

Iron in the Ocean: Laboratory experiments of iron geochemistry in the presence of marine particles

Thesis by
Anna Rose Beck

In Partial Fulfillment of the Requirements
for the Degree of
Doctor of Philosophy



California Institute of Technology
Pasadena, California

2012

(Defended August 31, 2011)

© 2012
Anna Rose Beck
All Rights Reserved

Acknowledgements

The end of a successful PhD does not come without its many supporters along the way.

I would like to thank my advisor Jess Adkins. He has a continued enthusiasm for science that rubs off on all of his graduate students, and he supports our interests outside of science. My thesis advisory committee members, Geoff Blake, Will Berelson, Paul Wennberg, and Jared Leadbetter, provided excellent guidance at crucial times in my PhD career. Geoff Blake and his wife Karen have been especially supportive ever since they became involved directly with Caltech student life as team MOSH (Master of Student Houses).

Numerous lab group members and other work colleagues, past and present, have always listened intently, made thoughtful comments on my research, and been an endless source of amusement and friendship. I thank Jeff Mendez, Seth John, and Alex Gagnon for their mentorship. Nithya sat with me in lab on a number of nights while I was cleaning syringe filters or doing sub-sampling, and I thank her heartily for this camaraderie. Nele Meckler graciously provided the foraminifera samples. John Crouse assisted with Matlab questions on occasion, as did Madeline Miller, and she helped me with the appropriate terminology when it comes to modeling. Deajung Kwon helped me learn how to run microcolumns for iron isotope measurements. Caterina Cherubini greatly improved my quality of life by assisting with syringe filter cleaning. I thank Andrew Homyk for his help with particle imaging.

I would like to thank a multitude of friends and colleagues across campus who provided unwavering support, especially Andy Downard, Vanessa Jönsson, Anne Dekas, Val Scott Kristof, Andrew Metcalf, and Claire Farnsworth. There were staff and stu-

dents from a number of offices or groups who always provided kind words and advice, from Residential Life and affiliated groups, Geological and Planetary Sciences, Environmental Science and Engineering, and the Dean's offices. The Caltech community has shown its willingness to provide help and support in a number of ways, and I am grateful to have worked with such a caring community.

My family and friends from back home and at college in Ohio, and those whom I have met along the way from there to here, all played an important role. I wouldn't be where I am today without their support, especially from my parents, Jim and Rae Lynn Beck, and my older brothers, Noah and Gabe.

Lastly, I owe huge thanks to my partner Michael Shearn for his willingness to bring me dinner in lab, help me endlessly with Matlab, be my dive buddy in the temperate coastal waters, embrace my love for cats, and discuss some of the finer points of research relating to iron in the ocean, all with a smile. His family also provided unconditional support and cheering.

Thank you to everyone for your support and kindness.

Thesis Abstract

Iron (Fe) is an important micronutrient for primary productivity in the ocean. The Fe cycle in the ocean is relatively unconstrained, especially when it comes to quantifying sources and sinks related to exchange with particulate matter. This thesis attempts to constrain some of the kinetic and equilibrium particle interactions with Fe bound to the siderophore desferrioxamine B (DFB). Out of five inorganic particle types investigated, ferrihydrite, goethite, opal, foraminifera, and montmorillonite, ferrihydrite has the largest, extended impact on dissolved FeDFB. From experimental and modeling results, ferrihydrite has two primary exchange pathways, absorption, with a rate of $4 \pm 2 \times 10^{-4} /(\text{mg/L})/\text{day}$, and dissolution, with a rate of $0.015 \pm 0.01 /\text{day}$. Uptake appears irreversible and follows a colloidal pumping model. Isotopic fractionation is also the greatest in the presence of ferrihydrite with signals up to $+1\%$ or higher with excess ligand. Dry montmorillonite has the biggest initial impact on FeDFB, resulting in a nearly instantaneous equilibrium and little isotopic fractionation. Goethite, opal, and foraminifera all have a minimal impact on FeDFB and show slight enriched isotopic fractionation, $+0.15\%$, in the presence of large particle concentrations. DFB seems to induce heavy Fe desorption or dissolution, while particle uptake seems to favor transfer of lighter Fe. These isotopic and kinetic parameters are important constraints on the ability of particles to control dissolved Fe, since they fall through the water column faster than equilibrium will be obtained.

Contents

List of Figures	ix
List of Tables	xi
1 Fe as a Micronutrient	1
1.1 Role of Ligands	3
1.2 Role of Particles and Size Fraction	4
1.3 Scope of Thesis	7
2 Methods	9
2.1 Materials	9
2.2 Characteristics of Particles	10
2.3 Experimental Setup	13
2.4 Sampling	15
2.4.1 Sample Analysis	16
2.5 Data Quality	16
2.5.1 Instrument Background	17
2.5.2 Chemical Blank and Detection Limits	17
2.5.3 Internal Error	18
2.5.4 External Error of Replicates	20
2.6 Spike Calibration and Mass Bias	25
2.6.1 Overall Error of [Fe]	27
2.7 Fe Isotope Experimental Setup	29

2.8	Sample Processing	31
2.8.1	Sample Analysis	32
2.9	Data Quality	32
2.9.1	Internal Error	32
2.9.2	Intermediate Error and External Error	34
2.9.3	Chemical Blanks	37
3	Kinetics of Ferrihydrite and FeDFB	38
3.1	Introduction	38
3.2	Experimental Setup	39
3.3	Results	39
3.3.1	Absorption	39
3.3.2	Desorption	40
3.4	Discussion	49
3.5	Modeling	57
3.6	Conclusions	71
4	Equilibration of FeDFB with Clay, Forams, Opal, Goethite, and Ferrihydrite	72
4.1	Introduction	72
4.2	Brief Experimental Setup	73
4.3	Results	74
4.4	Discussion	92
4.4.1	Absorption Experiments	92
4.4.2	Desorption	95
4.5	Conclusions	95
5	Fe Isotopic Fractionation in the Presence of Particles	98
5.1	Introduction	98
5.2	Brief Experimental Setup	99
5.3	Results	100

5.4 Discussion	103
5.5 Conclusions	105
6 Conclusions	110
A Natural Log Plots of Data from Chapter 4	113
Bibliography	115

List of Figures

1.1	Contours of atmospheric iron flux.	2
1.2	Open ocean Fe fertilization chlorophyll bloom.	3
2.1	Agilent Chemical Blank Levels.	19
2.2	Agilent internal error	21
2.3	Error Normalized Deviates	23
2.4	Kinetic Experiments, External Replicate Gaussian Fit.	24
2.5	Agilent Mass Bias	28
2.6	Neptune Internal Error	33
2.7	Fe Isotope error normalized deviates.	36
3.1	Control Fit Correction	42
3.2	Control experiments	42
3.3	Ferrihydrite Set 1 Experiments	43
3.4	Ferrihydrite Set 2 Experiments	45
3.5	Ferrihydrite, particles only, no DFB	47
3.6	Ferrihydrite Desorption Experiment.	48
3.7	Plotting the natural log of the relative Fe versus time	50
3.8	Ferrihydrite, $k_{sorb-part}$ slopes vs. particle concentration	52
3.9	Ferrihydrite TEM Images	56
3.10	Log C versus pH diagram of Fe(III) in the presence of ferrihydrite	61
3.11	Fit comparison of model to data, Set 1	62
3.12	Fit comparison of model to data, Set 2	63

3.13	Sensitivity test for k_{sorb} vs. k_{desorb} , Set 1.	64
3.14	Sensitivity test for k_{sorb} vs. k_{desorb} , Set 2.	65
3.15	Sensitivity test for k_{diss} vs. k_{precip} , Set 1.	66
3.16	Sensitivity test for k_{diss} vs. k_{precip} , Set 2.	67
3.17	Sensitivity test for k_{sorb} vs. k_{diss} , Set 1.	68
3.18	Sensitivity test for k_{sorb} vs. k_{diss} , Set 2.	69
4.1	Montmorillonite absorption experiment	76
4.2	Goethite absorption experiment	79
4.3	Opal absorption experiment	82
4.4	Foram absorption experiment	85
4.5	Largest particle concentration (6000 mg/L) absorption experiment.	88
4.6	Desorption experiments.	90
5.1	Fractionation of relative Fe dissolved in the presence of montmorillonite	106
5.2	Fractionation of relative Fe dissolved in the presence of ferrihydrite	107
5.3	Fractionation versus ferrihydrite concentration	108
5.4	Detail of fractionation regions close to 0‰ for ferrihydrite and montmorillonite.	109

List of Tables

2.1 Particle Characteristics.	11
2.2 SEM Images of Particle Types.	12
2.3 Kinetic Experiments, External Replicate Gaussian Fit Parameters. . .	24
2.4 Isotope Experiment Sample Matrix	30
4.1 Distribution coefficients for various particle types and concentrations.	96
5.1 Isotope data	102

Chapter 1

Fe as a Micronutrient

Iron (Fe) is an important micronutrient with implications for primary productivity in the ocean. Fe deficiency hinders primary productivity in waters that are rich in major nutrients such as nitrate, phosphate, and silicate [1]. Dissolved Fe concentrations are as low as 20 pM in remote surface waters of high-nitrate, low-chlorophyll (HNLC) regions and range up to approximately 1 nM in other areas [2, 3, 4]. Fe is needed for chlorophyll synthesis and even more so for nitrogen fixation [5, 6].

Since Fe is necessary for N-fixation, areas of nitrate depletion can indicate iron limitation, though phosphate limitation may play a role as well. Even though nutrients are remineralized, the nutrient cycling cannot reprocess organic nitrogen as readily as organic phosphate [7]. If the available nitrate is used up, this promotes nitrogen fixation, then the new nitrate and the more easily remineralized phosphate are used by photosynthetic organisms. Nitrogen fixation in the Atlantic is promoted by the atmospheric dust deposition from the Sahara Desert, though phosphate and iron can co-limit N-fixation [8]. In the Pacific, nitrogen depletion, relative to phosphate, should encourage N-fixers, however, due to a lack of iron, N-fixation is hindered. The Southern Ocean and parts of the Pacific are places that have unused nitrate and phosphate, though the southern Pacific is slightly nitrate and iron limited. These HNLC locations (Southern Ocean, Equatorial Pacific, and the southern Pacific Ocean) are potential spots where iron might be limiting primary productivity.

The major source of iron to the open ocean comes from dust and accounts for about three times as much dissolved iron deposition into the ocean as river input [9]. Duce and Tindale approximated atmospheric iron fluxes into the surface waters around the globe (Figure 1.1). The highest atmospheric fluxes are in the northern hemisphere

and closest to the eastern Atlantic and far western Pacific Oceans. The lowest fluxes occur in the central and southern South Pacific and in the Southern Ocean. A more recent study showed lower fluxes, by an order of magnitude, in the NW Pacific Ocean than those predicted by Duce and Tindale [10], which highlights the limiting nature of dust and iron input into the ocean.

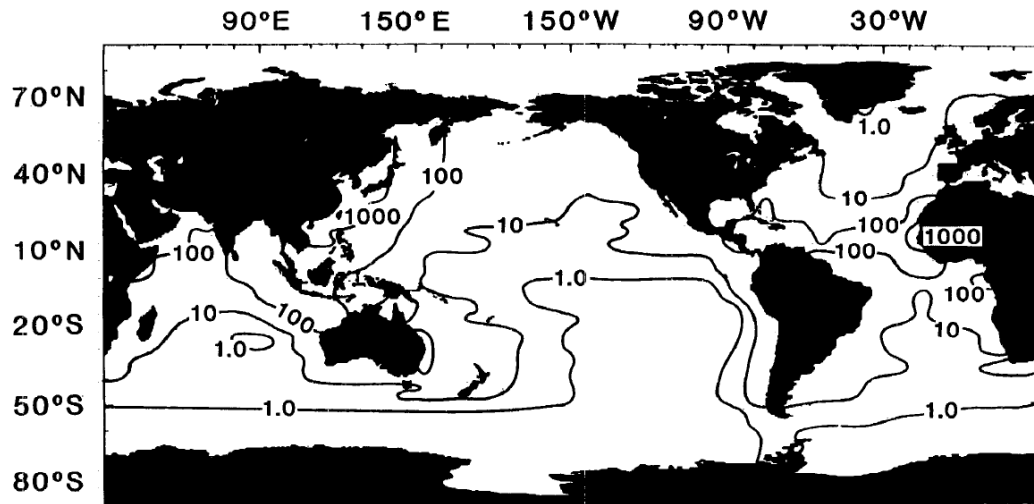


Figure 1.1. Contours of total atmospheric iron flux (particulate and dissolved) into the surface of the ocean ($\text{mg}/\text{m}^2/\text{yr}$). The areas of the ocean with little atmospheric dust input correspond to high nutrient, low chlorophyll regions (HNLC) where additional Fe sources would stimulate primary production. [9]

The iron hypothesis states that an increase in iron deposition to the open ocean during glacial times alleviated iron stress on the biological community, allowing more production [11]. This production increased the rate at which CO_2 was removed from the atmosphere and deposited into the deep ocean. Dust loads in the Vostok ice cores from glacial times are approximately 50 times higher than current interglacial levels, presenting a possible heightened source of iron. If there were abundant iron concentrations in the oceans, other nutrients would have been used to a fuller capacity and atmospheric CO_2 would have been drawn down.

Iron fertilization experiments have been conducted to measure the potential new productivity that could be achieved when sufficient amounts of iron are added to a

patch in an HNLC area. Large-scale chlorophyll blooms have been observed during such experiments in the Pacific, followed by increases in the grazer population [12, 13]. In one such experiment, the ratio of carbon to iron uptake found in the bloom was approximately C27,000:Fe1, highlighting Fe's small but important role. Fertilization studies have also been carried out in the Southern Ocean [14] and N Atlantic [8] with the occurrence of chlorophyll blooms (Figure 1.2). CO₂ fluxes into the ocean have been found to increase over the experimental patch [15]. More importantly, none of these enrichment experiments have seen sustained increases in primary productivity coupled by increased organic carbon export to the interior of the ocean [15]. This could be due the changes in the bioavailability of Fe during the experiments.

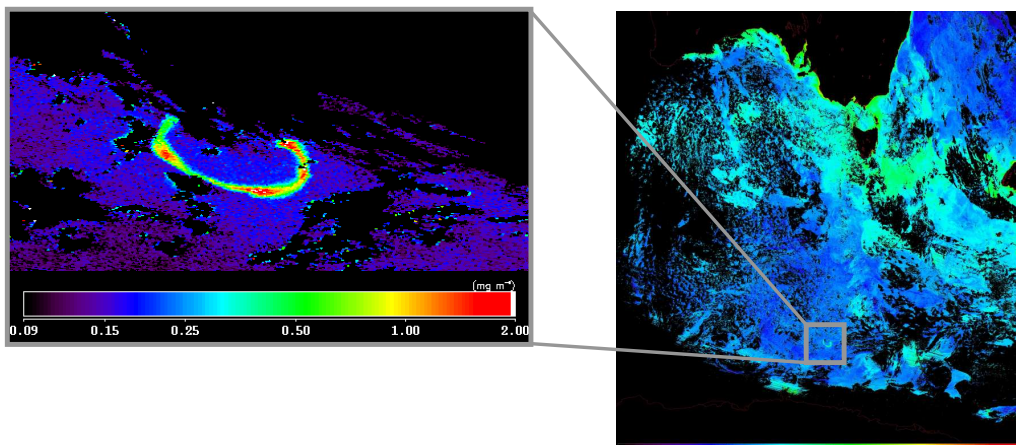


Figure 1.2. Satellite image of the Southern Ocean Fe fertilization experiment (SOIREE) cruise track that induced a chlorophyll bloom. Warmer colors indicate higher volumes of biomass (mg/m^3). [14]

1.1 Role of Ligands

Organic ligands complicate the bioavailability of Fe. Fe(II), the more soluble form, is rapidly oxidized to Fe(III) in oceanic surface waters with a half life of several minutes [16]. Voltammetry methods were developed to differentiate inorganic from organic Fe and discovered that over 99.9% of Fe is organically complexed [17, 18].

There are two classes of ligands based on conditional stability constants; K L1, Fe^{3+} is $\sim 10^{23}$ and K L2, Fe^{3+} is the weaker class, at $\sim 10^{22}$, though class L2 is typically higher in concentration [19]. During the Fe fertilization experiments in HNLC regions, the concentrations of these ligand classes switches to favor the stronger L1 class [14]. This happens because of a species-specific response to Fe bioavailability.

Some oceanic bacteria and phytoplankton produce siderophores in response to iron stress. These siderophores are strong iron binding ligands that generally fall into the L1 class. Autotrophic prokaryotes are able to access the stronger L1 class, and autotrophic eukaryotes can only utilize the weaker L2 class [20]. This utilization reflects the origin of siderophores as an evolutionary adaptation by prokaryotes to obtain Fe, whereas eukaryotes found a more generic pathway for Fe uptake via mediating Fe reduction, mostly from the weaker tetradentate porphyrin L2 class [20]. Indeed, a particularly strong terrestrial siderophore, desferrioxamine B (DFB) has been shown to limit productivity in coastal waters [20, 21] and in the Equatorial Pacific [22]. Additional experiments show that some types of marine siderophores do not have any effect on eukaryotic phytoplankton and yet still support, through modeling results, that they are primarily accessing the L2 class [23].

In addition to species-specific competition, other processes exist for Fe utilization from the organic ligand pool. Photolysis of these complexes leads to lower-affinity Fe(III) ligands and to the reduction of Fe(III) to Fe(II), a more soluble form of iron, or more reactive Fe(III), depending on the type of siderophore [24, 25]. The possible mechanisms for acquiring this complexed Fe(III) include cell-initiated release of extracellular reductases [26], or cell-bound surface reductases [27]. These processes can make iron more bioavailable for phytoplankton uptake.

1.2 Role of Particles and Size Fraction

In addition to organic complexation, there are chemical reactions with particles, particle concentrations and dynamics, and other physical properties of the ocean (temperature, salinity, pH) that are also controlling the dissolved Fe concentrations throughout

the water column [28, 29].

The ability to quantify mass flux and other particle dynamics progressed following Th isotope measurements in the dissolved and particulate phases by Bacon and Anderson in 1982 [30]. These Th isotopes are naturally occurring radioisotopes of the U-series decay, and its supply can be determined from its parent nuclides and distributions. Bacon and Anderson concluded that an equilibrium, including adsorption and desorption, exists between thorium and particle surfaces in the deep sea, an assumption asserted before but never verified. According to their model, the residence time of any metal in the ocean is controlled by the equilibrium partitioning between dissolved and particulate phases and the residence time of the particulate matter.

Other uses for uranium series metal tracers of particle dynamics include export production [31], mass flux quantification [32, 33], calibration of sediment traps [34, 35, 36], and water mass circulation [37, 38]. Particulate (dia. $> 0.45 \mu\text{m}$) metal concentrations and particle flux have been measured in the ocean with the help of sediment traps [28, 39, 40, 41, 42, 43, 44, 45, 46, 47, 48, 49, 50]. The quantification of water mass circulation and mass flux is vital to understanding the ventilation rate of the deep ocean and its possible effect on long-term climate variability.

The size of particles is also a factor in their sinking and adsorption/desorption abilities [51, 52], with special attention paid to the colloidal fraction. Colloids are defined as micro- and macroparticles that remain in the dissolved phase, meaning that they pass through a $0.45 \mu\text{m}$ filter. They are hypothesized to be responsible for slow sorption kinetics, wherein metal adsorbs irreversibly onto the colloids and then gradually coagulates into the particle phase [53, 54, 55]. Several field studies with radiotracers that have been carried out in river, estuary, and sea water confirm that colloidal trace metals decrease as particulate matter increases [56, 57]. Measurements of soluble ($< 0.02 \mu\text{m}$) and colloidal Fe, together comprising the “dissolved phase”, in the North Atlantic and North Pacific, showed that truly soluble Fe had a more characteristic nutrient-like profile (depleted at the surface and more enriched at depth) than the colloidal Fe (which had a maximum at the surface and minimum within the upper nutricline), suggesting that soluble Fe is more bioavailable than colloidal Fe [58].

A significant amount of colloidal Fe is thought to be organically complexed and subject to removal via coagulation, thus decreasing its bioavailability more than if it was sequestered by ligands in the soluble phase [59, 60]. Despite the focus on removal of organic Fe in these colloidal pumping studies, there is evidence that some siderophores, in this case DFB-bound Fe, exist predominantly in the soluble fraction when the ligand is in large excess (15:1) of dissolved Fe [61]. Even though soluble Fe has been characterized as the more bioavailable Fe size fraction [58], laboratory cultures have been growth limited by complexation of Fe to DFB [62, 20, 22]. Obviously, species-specific acquisition of Fe is a more accurate representation of bioavailability compared to an operationally defined size fraction. Both inorganic and organic forms of colloidal Fe are found to be bioavailable to diatoms [63, 64, 65]. The growth and grazing of diatoms release organic colloidal iron species, potentially relieving iron limitation [66]. Studies that have found biota utilizing both soluble and colloidal size fractions indicate the potential, and probably time-consuming, need to differentiate “bioavailable” Fe by classes of species and their respective available Fe, rather than by a generic, operationally defined size fraction.

While numerous studies have measured the distribution of metals in the particulate and dissolved phases, as an equilibrium partitioning coefficient K_D , in estuaries with high particulate loads [67, 49], and in other natural aquatic systems [68, 29] (and references within), particle equilibrium with the dissolved phase can only be assumed if the residence time of particles is long compared to the reactivity of dissolved trace metals. In turn, the reactivity of trace metals can vary widely among particle types and concentrations, thus creating the need to use a kinetic approach to describing metal-particle interactions [29, 69].

Studies have suggested complications with using Pa/Th as a water mass circulation tracer due to its absorption affinity for certain particle chemical compositions [70, 71, 72, 73, 74, 75]. In particular, there seems to be preference for adsorption of Pa onto opal and increased fractionation of Pa/Th during uptake by silicate and carbonate particles [76]. Additional paleoclimate proxies, such as Cd/Ca, have been investigated for their use as a tracer of past nutrient cycling and productiv-

ity [77, 78, 79, 80]. Elderfield and Rickaby incorporated preferential uptake of Cd versus phosphate due to fractionation during particle formation into Cd/Ca data sets [81]. This reconstruction of the Cd/Ca ratios in foraminifera matched proxy records showing nutrient under-utilization in the Southern Ocean during the Last Glacial Maximum, thus underlining the importance of metal-particle interactions in oceanic data interpretations.

In addition to the field studies, there have been laboratory experiments to determine metal-particle dependence and equilibriums. Geibert and Usbeck examined the preferential uptake of Pa and Th onto different particle types [82]. They found significantly different equilibrium distributions among the types of particles and filtered natural seawater used. The preferential uptake of Pa onto opal was observed, as seen in field studies, and distinct fractionations between clay and opal, while carbonate was highly variable. The variation across seawater types probably results from a variety of natural dissolved organic ligands that play a role in dissolved metal profiles.

Laboratory experiments have been used more frequently for the determination of sorption kinetics in estuaries because of the higher importance on particle scavenging due to the large suspended sediment loads, approximately 0.5 g/L in an estuary compared to 0.5 mg/L in the ocean. These studies have examined the qualitative kinetic dependence on pH, salinity, and particle concentration for adsorption and desorption of Cd, Cr, Co, Fe, Mn, and Zn [67] and includes some adsorption modeling that fits, within uncertainties, experimental results [83]. These studies do not calculate quantitative uptake rates for open ocean conditions, such as salinity and pH, and do not take into account any particle preference.

1.3 Scope of Thesis

This thesis addresses the need for controlled laboratory experiments with siderophore-bound Fe to determine: 1) forward and reverse rate constants with corresponding mechanisms, 2) preference for Fe uptake (and release) from different types of particles, abiotic and biologically produced, and 3) the particle isotopic fingerprint on the

dissolved Fe phase.

Chapter 2

Methods

2.1 Materials

All solutions and artificial seawater used in the experiments are made with 18.2 M Ω milliQ water. Acids and bases are trace-metal clean and come from SeaStar, unless noted as reagent grade (RG). Dilutions are given as % volume. All plastic bottles and columns were progressively leached with citranox (1%), RG HCl (10%), then RG HCl (1%) and stored (0.5% HNO₃ or 0.1% HCl).

The seawater was prepared from the seawater salts (SOW) method section of the AQUIL procedure [84]. Reagent salts were mixed in a carboy (10 L) and titrated to pH 8 (10 M RG NaOH, ca. 150 μ L). Chelex 100 (Bio-Rad Laboratories, Drymesh 100–200, Na form) was cleaned in batches (30–50 g) as described in the reference. The Chelex 100 resin was mixed with the SOW (300 mL) and titrated to pH 8 (1 M RG NaOH) and then poured into a column (LDPE, Bio-Rad, 10 mL). SOW was purified in 4 L batches at a time and stored in containers (polycarbonate, Nalgene) with the caps wrapped in parafilm to decrease vapor exchange. The resulting cleaned seawater is referred to as AQUIL or artificial seawater throughout the text.

For sampling and sample processing, all syringes (5 or 10 mL, LDPE, VWR) and centrifuge vials (1.5 mL, Global Scientific) were leached over heat (60 °C) in 10% RG HCl, 1% HCl, then 0.1% HCl. The syringes were rinsed and filled with water so that the pH of the samples would be minimally affected upon filtration. Luer-lock style syringe filters (0.2 μ m, 25 mm dia, polypropylene, Pall) were individually cleaned with 10% RG HCl (10 mL), 1% HCl (10 mL), and water (2 \times 10 mL).

All stock and working solutions were prepared in a flow bench using trace-metal-

clean techniques. An unacidified stock solution (3 mM) of the siderophore desferoxamine B, DFB, (desferoxamine mesylate, CALBIOCHEM) was prepared and kept refrigerated (2–8 °C). A ^{54}Fe stock solution (ca. 800 μM , 2% HNO_3) was prepared from enriched Fe_2O_3 solid (Oak Ridge Laboratories). A working ^{57}Fe standard (2.83 μM , 2% HNO_3) was carefully prepared for use as an internal reference spike in the sample analysis.

Five types of common marine particles were obtained. Commercially available goethite (stable iron oxide) and montmorillonite (clay) were purchased from Alfa Aesar. Opal, a SiO_2 mineral, was purchased as diatomaceous earth, a pulverized form of the dried shells from the diatom organisms. Carbonate shells from foraminifera (forams) were from a sample obtained aboard a research cruise in the Caribbean. Ferrihydrite, a fresh, labile iron oxide, was precipitated immediately prior to addition to experiment bottles. Solid $\text{FeCl}_3 \cdot 6\text{H}_2\text{O}$ was dissolved in water and, while stirring, carefully brought to pH 8 (NH_4OH). The dark reddish brown, voluminous precipitate was filtered (0.2 μm , polycarbonate) and scraped into a small volume of water (4–10 mL, pH 8). The ferrihydrite precipitate was aged 30 to 60 minutes from time of precipitation over the course of addition by pipette into the experiment seawater bottles. The other four particles were also mixed in water (pH 8) for quick addition to multiple experiment bottles by eliminating the need to weigh every particle addition.

2.2 Characteristics of Particles

The particles contain a variety of chemical components with surface areas spanning 3 orders of magnitude (Table 2.1). Surface area references for the same particle type differ by factors of 2 or 3. This is due to the difficulty of absorbates, such as nitrogen, evenly coating and reaching all the surfaces of the finer particulate matter or porous spaces when measuring surface area. The particles were imaged using a Zeiss 1550VP Field Emission Scanning Electron Microscope (SEM) (Table 2.2).

Known amounts of the particles were dissolved or leached in acid over 1 week to determine Fe abundance. Chemical composition dictates huge amounts of Fe within

Particle Type	Chemical Formula	Iron Density		Surface area
		$[\frac{\text{nmol Fe}}{\text{mg}}]$	(1σ)	$[\text{m}^2/\text{g}]$
Ferrihydrite	$\text{Fe}(\text{OH})_3$	3,180		650
Goethite	$\text{Fe}(\text{O})\text{OH}$	11,255		250
Montmorillonite	$\text{R}_{0.33}^+\text{Al}_2\text{SiO}_4\text{O}_{10}(\text{OH})_2 \cdot x\text{H}_2\text{O}$	1.1	(0.1)	23-600
Opal	SiO_2	0.83	(0.04)	4-30
Foraminifera	CaCO_3	0.72	(0.01)	4

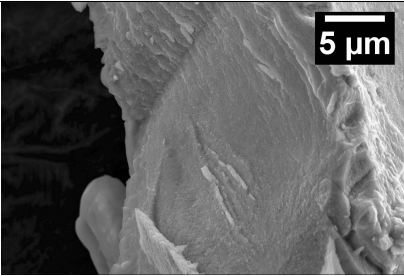
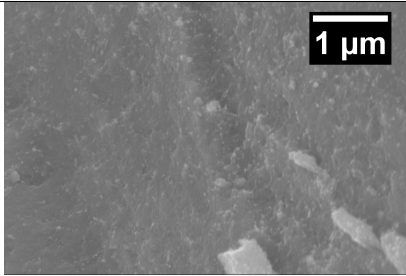
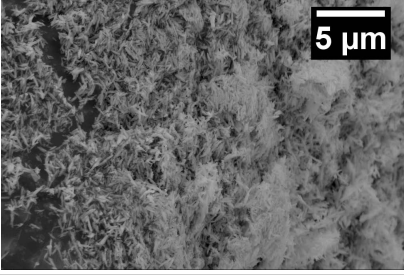
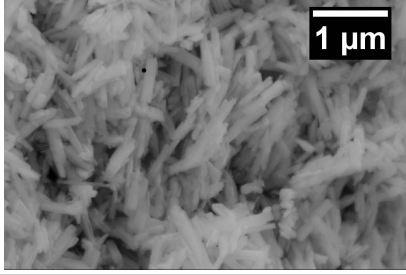
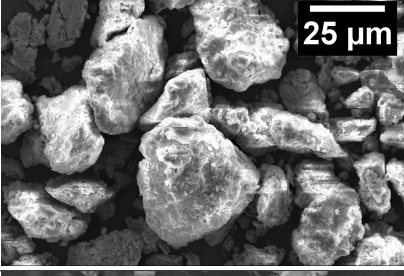
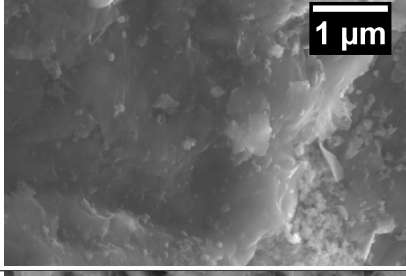
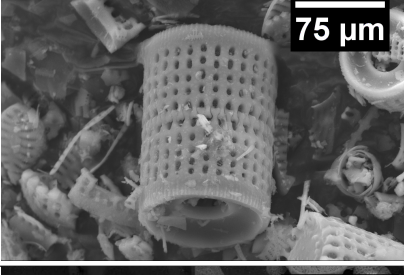
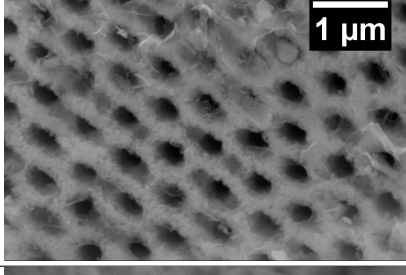
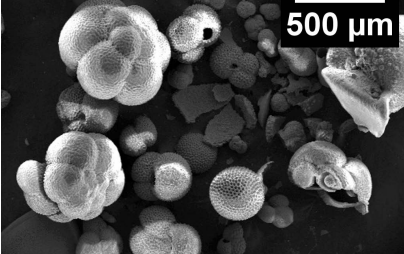
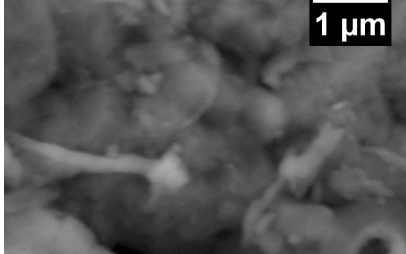
Table 2.1. Types of particles used in experiments and their respective chemical formulas. The amount of Fe per particle (nmol Fe/mg) was calculated from the chemical formula for the iron oxides or measured, as described in the text, for the other types with 1 standard deviation (1σ) in parentheses. Surface area measurements using BET are included for montmorillonite, opal, and forams, and literature values are included for ferrihydrite and goethite [85], montmorillonite [86], and opal [87].

the iron oxides ferrihydrite and goethite, ranging from 3180 to 11,255 nmol Fe/mg. These particulate concentrations are based on the assumed chemical stoichiometry. The interiors of ferrihydrite aggregates have chemical compositions very similar to $\text{Fe}(\text{O})\text{OH}$ [88], suggesting that there is an increasing amount of Fe stored in the subsurface of ferrihydrite as it aggregates and ages.

Ferrihydrite has the highest surface area and the most potential to undergo morphological change due to its fresh, labile state. Ferrihydrite can further crystallize into goethite, hematite, lepidocrite, magnetite, or maghemite under the appropriate conditions [85]. With aging, the dissolution of ferrihydrite can be reduced by 2 orders of magnitude within 1 week of formation [89]. Ferrihydrite contains 2-5 nm nanoparticles with a surface area notoriously difficult to estimate due to marked aggregation as seen in Table 2.2.

Goethite is a more refractory iron oxide, leading to the assumption that it is less bioavailable. Studies suggest that in the presence of multiple ligands or one siderophore and increased temperatures, goethite dissolution could be induced, lead-

Table 2.2. Zeiss 1550VP field emission SEM images. There is a range of surface features across all particle types. Ferrihydrite and montmorillonite particles appear as highly aggregated though are comprised of nanoparticles.

Particle type Surface area [m ² /g]	SEM images	
	Low magnification (120-9k X)	High magnification (50k X)
Ferrihydrite 650		
Goethite 250		
Montmorillonite 23-600		
Opal 4-30		
Foraminifera 4		

ing to possible biological acquisition [90, 91]. Another study suggests that common surfactants in the ocean could promote goethite dissolution [92]. Goethite is composed of 200 nm rod-shaped crystals with an approximate surface area of 250 m²/g.

The montmorillonite is a type of swelling clay, with an octahedral layer between 2 tetrahedral layers that can expand with water intake. The surface area of this clay can vary between 200 to 600 m²/g depending on cation substitutions [86], though our BET measurements indicated a surface area of only 23 m²/g. This low surface area could be due to difficulties of evenly coating all tiny, clay particles with N₂. Particle size ranges from less than 1 μm to 30 μm.

Various diatoms species have been well documented for acquiring Fe opportunistically, often dominating phytoplankton blooms in open ocean Fe fertilization experiments (Chapter 1). Opal is the generic term for biogenic produced SiO₂. Opal contains numerous pore spaces, leading to a higher surface area than one might guess for a particle this size. The sample contains both crushed and intact diatom SiO₂ hard parts, leading to an overall measured surface area of 30 m²/g. Crushed diatom cultures have had as low as 4 m²/g measured surface areas [87].

The forams range from 0.5 μm to 4 or 5 μm in diameter with only mild porosity, thus having the lowest surface area of all the particles. Forams are common marine organisms that are collected from sediments and used as temperature proxies for past ocean conditions.

2.3 Experimental Setup

Natural abundance Fe contains four stable isotopes: 91.754% ⁵⁶Fe, 5.845% ⁵⁴Fe, 2.119% ⁵⁷Fe, and 0.282% ⁵⁸Fe. In order to track two separate pools of Fe, the dissolved and particulate phases, we use a less abundant isotope as a tracer, ⁵⁴Fe. Since the iron oxide particles used in these experiments, and any Fe contamination already present on the other particle types, are natural abundance Fe, we can track the particulate phase as ⁵⁶Fe and the dissolved phase as ⁵⁴Fe.

We set up two types of experiments based on where the ⁵⁴Fe tracer began. The first

was primarily an “adsorption” experiment, where we added the ^{54}Fe to the dissolved phase of AQUIL, and then added particles. The second was primarily a “desorption” experiment, where we equilibrated the ^{54}Fe with high concentrations of the various particles, and then added the filtered particles to clean AQUIL.

For both sets of experiments, the ^{54}Fe was equilibrated with DFB at a $\sim 1:1$ ratio for at least 2 days (pH 3, in the dark). Experiment bottles (250 mL, HDPE) were filled with the artificial seawater (250 mL). The bottles varied with the ambient room temperature from 19 to 23 °C. The reaction bottles were placed in an opaque action packer on top of an orbital shaker table (VWR, 3.6 RPM).

For adsorption experiments, small amounts of $^{54}\text{FeDFB}$ (< 1 mL) were added to the experiment bottles to minimize pH change of the AQUIL and to create a dissolved Fe concentration between 400 and 600 nM. All other Fe species contribution is estimated to be less than 0.1 nM based on thermodynamic constants [93]. The bottles were placed in the dark on the shaker table for at least 2 days to allow the $^{54}\text{FeDFB}$ to equilibrate with the walls.

There were three sets of adsorption experiments to test varying particle concentrations. There was only one particle type per bottle. For the first adsorption experiment, goethite, clay, opal, and ferrihydrite particles were pipetted from their respective solutions to result in experiment bottles with approximately 200, 20, 2, 0.2, and 0.02 mg/L. The forams were pipetted to obtain 141 and 14 mg/L. The remaining three bottle concentrations of forams were determined by initial mass of the forams, yielding 208, 51, and 31 mg/L. A replicate bottle of 20 mg/L ferrihydrite was made to test the reproducibility of the experiment. A control was made that had the $^{54}\text{FeDFB}$ tracer and no particles. A particle only bottle was made for each particle type with 20 mg/L (or 14 mg/L for forams) and no $^{54}\text{FeDFB}$. The pH varied between 8.19 and 8.24 for the bottles with particle additions and the control, respectively. This set of adsorption experiments is collectively referred to as Set 1 for ferrihydrite, for differentiating between the two sets of ferrihydrite adsorption experiments.

The second adsorption experiment tested a higher particle concentration for goethite (6080 mg/L), clay (6040 mg/L), opal (6120 mg/L), and forams (6240 mg/L). Dry par-

ticles were weighed before direct addition to the bottle containing $^{54}\text{FeDFB}$ in AQUIL. The pH was 8.20.

The third adsorption experiment, referred to as Set 2 for ferrihydrite, tested four additional ferrihydrite concentrations of 570, 349, 172, and 33 mg/L. The pH of the bottles was 8.0 (± 0.05).

Drying down and weighing the pipetted quantities separately confirmed particle amounts. Pipetted particle concentrations are consistent to 10%, except 0.02 mg/L, which was 30%. The bottles remained on the shaker table in the dark, so that the AQUIL was moved around in the bottle, except during sampling, however not all of the particles remained in constant suspension.

For the desorption experiment, approximately 250 mg of each particle type sat in a 1 mL solution of $^{54}\text{FeDFB}$ (pH 8) for 1.5 days, which created an effective particle concentration of 2.5×10^5 mg/L. Particles were filtered (polycarbonate, 0.2 μm , 25 mm) and scraped from the filter paper into the bottle of artificial seawater (250 mL). Replicate filter scrapings were dried down and weighed to estimate the amount of particles that was added to each bottle. Replicates agreed within 10%. The estimated experimental particle concentrations are 247 mg/L—forams, 232 mg/L—opal, 210 mg/L—goethite, 208 mg/L—clay, and 166 mg/L—ferrihydrite. There was too little solution remaining to collect the filtrate via syringe filtration, described in Section 2.4, so there is no estimate of the remaining ^{54}Fe that did not absorb onto particles.

2.4 Sampling

All sampling was done in a flow bench using trace-metal-clean techniques. Sub-samples (50 μL) were taken before particle addition to obtain the initial Fe concentration and taken periodically throughout the experiments, with more intense sampling within the first week after particle addition. For each sub-sample, a few milliliters were poured from a well-shaken bottle into the bottle's wide mouth cap, without the sample touching the threads. 2 or 3 mL were drawn into a syringe, and then pushed through a syringe filter (0.2 μm) that was previously cleaned. Our experiments do

not differentiate between soluble and colloidal Fe.

The first 1 mL of filtrate was discarded and the rest went into a centrifuge tube. Two replicates were created for each sub-sample filtrate. 50 μL was pipetted into a second centrifuge vial, referred to as the B replicate in following sections. Then, 50 μL were taken from the first vial, the remainder of the filtered sample discarded, and the 50 μL placed back into the empty vial, referred to as the A replicate. Each sub-sample was spiked with a calibrated ^{57}Fe standard (10 μL) and diluted (0.5% HNO_3 , x6) to reduce the AQUIL matrix interferences during sample analysis.

Chemical blanks (50 μL) of clean AQUIL from the same batch as the experiments were spiked and diluted identically to the samples.

2.4.1 Sample Analysis

All samples and chemical blanks were run on an Agilent 7500 Inductively Coupled Plasma Mass Spectrometer (ICP-MS). Fe standards (5 ppb–20 ppb, 0.5% HNO_3) of natural abundance were run during each sequence to determine the mass bias correction factor of the instrument. A maximum of 48 samples, including blanks, were run during each sequence.

Total counts from each mass measured on the ICP-MS were used to compute Fe concentrations, including background subtractions. ^{54}Fe and ^{56}Fe were calculated for each blank and sample. The ^{54}Fe and ^{56}Fe concentrations were determined by reference to the internal ^{57}Fe spike and the mass bias correction factor, then the blank averages for ^{54}Fe and ^{56}Fe from each sequence run were subtracted from their respective samples, as described further in the next section.

2.5 Data Quality

This section contains subsections relating to instrument background, chemical blanks and detection limits, internal error, external error of replicates, and spike calibration and mass bias.

Samples, blanks, and standards were scanned at masses 54, 56, and 57 a total of

25 times during 1 acquisition, amounting to $n = 25$ or less for measured ratios $R_1 = {}^{54}\text{Fe}/{}^{57}\text{Fe}$ and $R_2 = {}^{56}\text{Fe}/{}^{57}\text{Fe}$. A 3σ outlier test was performed on data ratios and total counts from each acquisition, resulting in $n = 20$ minimum for some samples due to outliers. Each sample only had 1 acquisition from which average ratios and standard errors were calculated. A small subset of samples ($n = 24$) were re-run during a different Agilent sequence session, and the difference between sample [${}^{54}\text{Fe}$] and [${}^{56}\text{Fe}$] was entirely within the internal error of the samples, indicating that the instrument analysis method for determining [Fe] is robust from one analytical session to the next.

2.5.1 Instrument Background

Since all samples were diluted in 0.5% HNO_3 , an instrument blank of the same make-up was run at multiple points throughout the sequence. The instrument background was subtracted from the total counts of each acquisition scan of the chemical blanks, standards, and samples. The instrument background amounted to less than 0.1% of all ${}^{57}\text{Fe}$ counts for spiked blanks and standards. Total ${}^{54}\text{Fe}$ and ${}^{56}\text{Fe}$ counts for the instrument background were comparable to un-spiked AQUIL, indicating that the AQUIL was close to its minimum values for these Fe isotopes.

2.5.2 Chemical Blank and Detection Limits

[${}^{54}\text{Fe}$] and [${}^{56}\text{Fe}$] chemical blanks throughout all the Agilent sequences are shown in Figure 2.1 ($n = 150$). ${}^{54}\text{Fe}$ blanks deviate around 0 nM, with 2σ of 3.8 nM for the entire population, indicating that the ${}^{54}\text{Fe}$ in the chemical blanks was minimal. ${}^{56}\text{Fe}$ blanks averaged 35 nM, with 2σ of 4.5 nM. By comparing multiple unspiked AQUIL counts to spiked AQUIL chemical blank counts, this increase in ${}^{56}\text{Fe}$ relative to ${}^{54}\text{Fe}$ in the blanks is almost entirely due to the amount of ${}^{56}\text{Fe}$ in the ${}^{57}\text{Fe}$ spike. In the spike, ${}^{56}\text{Fe}$ is around 6.3% abundant and ${}^{54}\text{Fe}$ is less than 0.1% abundant. Since all sub-samples were the same volume and were spiked with the same volume, a fairly consistent amount of ${}^{56}\text{Fe}$ is present in all analyses. The larger blank con-

tamination problems would also manifest themselves as ^{56}Fe since dust and sample handling would mostly introduce natural abundance Fe, where ^{56}Fe is 91.754% abundant. However, the relative error in the ^{56}Fe blank is only 6.5%, which indicates little contamination and good reproducibility for the method.

Detection limit is 3σ of the blank, so our detection limits for these experiments are 6 nM and 7 nM for ^{54}Fe and ^{56}Fe , respectively.

2.5.3 Internal Error

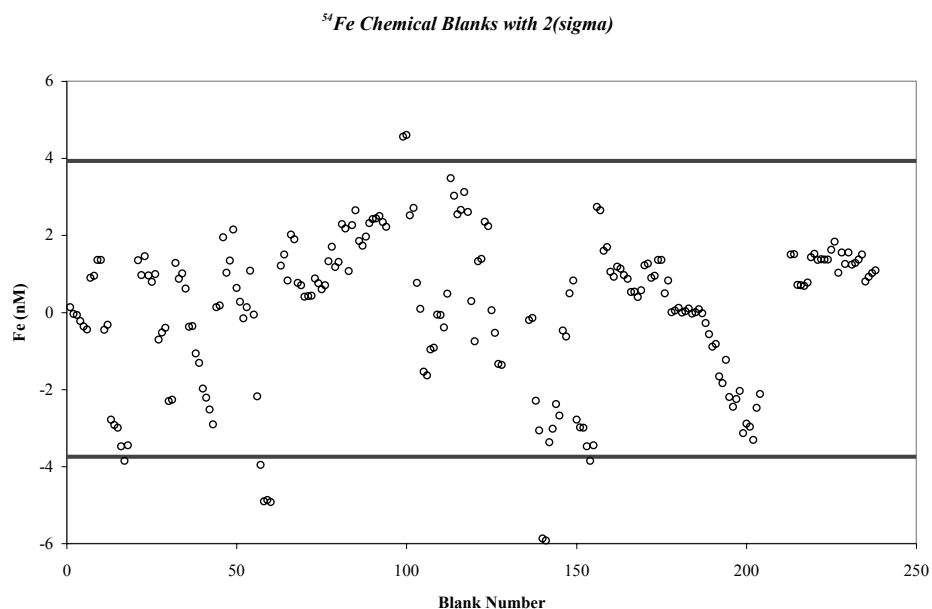
Internal error is the amount of uncertainty in measuring R_1 and R_2 values for each Agilent acquisition and is limited by counting statistics if our data are evenly distributed over time. We can compare the error of our ratios that were measured 20 to 25 times to the error predicted from the total number of counts, N .

For our acquisition method, the Agilent reports the counts per second for each mass number, so calculating the total amount of time spent measuring counts is necessary for determining N . Each mass is measured during 0.3 seconds for 100 times per scan, and the total number of scans varies from 20 to 25. For our statistical test, the total number of counts measured for each mass is determined by multiplying the averaged reported counts per second by 30 and by its respective number of scans kept after the 3σ outlier test. In counting statistics, the error for measuring N counts for a given mass is $\sigma = \sqrt{N}$. Following the propagation of error of a ratio, we compute the theoretical internal error due to counting statistics:

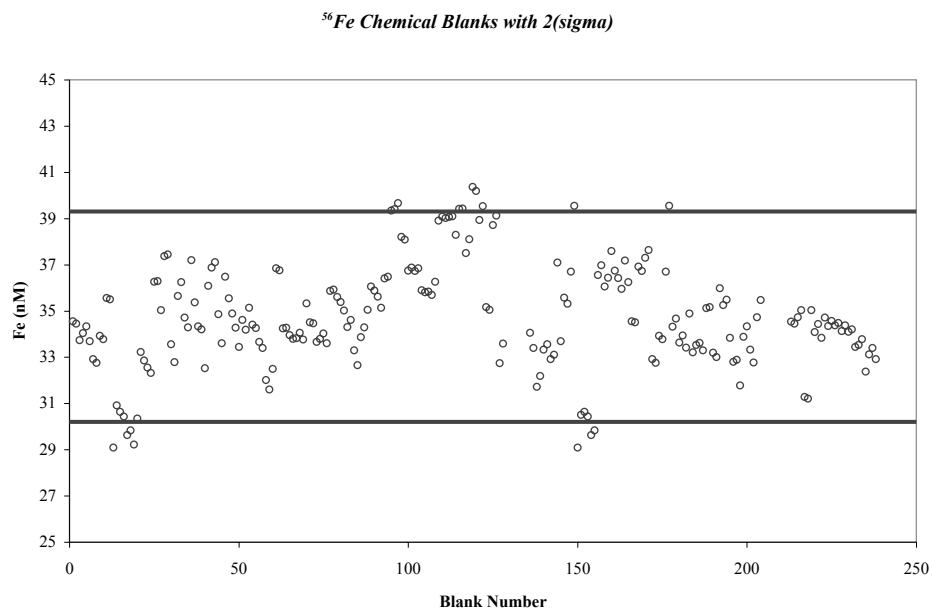
$$\sigma_{\text{counting statistics}} = \sqrt{\frac{N_1 + N_2}{N_1 \cdot N_2}}, \quad (2.1)$$

where N_1 and N_2 are the total counts for the masses of that respective ratio. The standard deviation of the mean decreases as \sqrt{N} , so we must compare the error to the effective intensity of each isotopic ratio measured, N_{eff} , where

$$N_{\text{eff}} = \frac{N_1 \cdot N_2}{N_1 + N_2}. \quad (2.2)$$



(a) Few interferences or blank contamination.



(b) Consistently around 35 nM due to presence of ⁵⁶Fe in the ⁵⁷Fe spike.

Figure 2.1. Agilent chemical blank concentrations (nM). A chemical blank consists of the same proportions of clean AQUIL and clean, dilute nitric acid (0.5%) as the samples.

Therefore, by combining equations, the relative error predicted for measuring a given ratio becomes

$$\sigma_{\text{counting statistics}} = \frac{1}{\sqrt{N_{\text{eff}}}}. \quad (2.3)$$

The internal error of measuring ratios on the Agilent relative to counting statistics, a log-log plot of relative standard error (RSE) versus N_{eff} , is given in Figure 2.2 for the Fe standard solutions run throughout the all of the sequences.

$$\text{RSE}_{\text{standard}} = \frac{\sigma/n}{R_{\text{ave}}} \quad (2.4)$$

where R_{ave} is the average ratio over the number of scans kept, n is the number of scans kept, and σ is the standard deviation of the measured ratios.

From the plot, we can see that our internal error does trend with counting statistics, however it exceeds that predicted by counting statistics on average by 0.5 log units, or a factor of 3. This offset happens for two reasons. The first is our inability to obtain instantaneous ratios. The Agilent sweeps through the mass range and measures each mass individually, so there will be some inherent drift in the masses between mass measurements. This also means that as we measure masses that are further apart in mass units, the less we are able to precisely measure ratios. Secondly, there is an additional source of error beyond counting statistics at lower signal intensities due to Johnson noise. The variation in instrument background counts becomes more important at lower counts and could account for the offset from counting statistics, especially below $\log N_{\text{eff}}$ of about 6.

2.5.4 External Error of Replicates

Each sub-sample for experiments run on the Agilent was spiked and diluted separately before analysis. Comparison of these sub-samples to each other gives an estimate of the reproducibility of the sampling method throughout the experiments. Overall, there were 1331 pairs of replicates. Most, if not all, replicate pairs were analyzed during the same sequence. Therefore, these samples cannot be used as an indication

Fe Standard Solution Ratios on Agilent 7500 ICP-MS

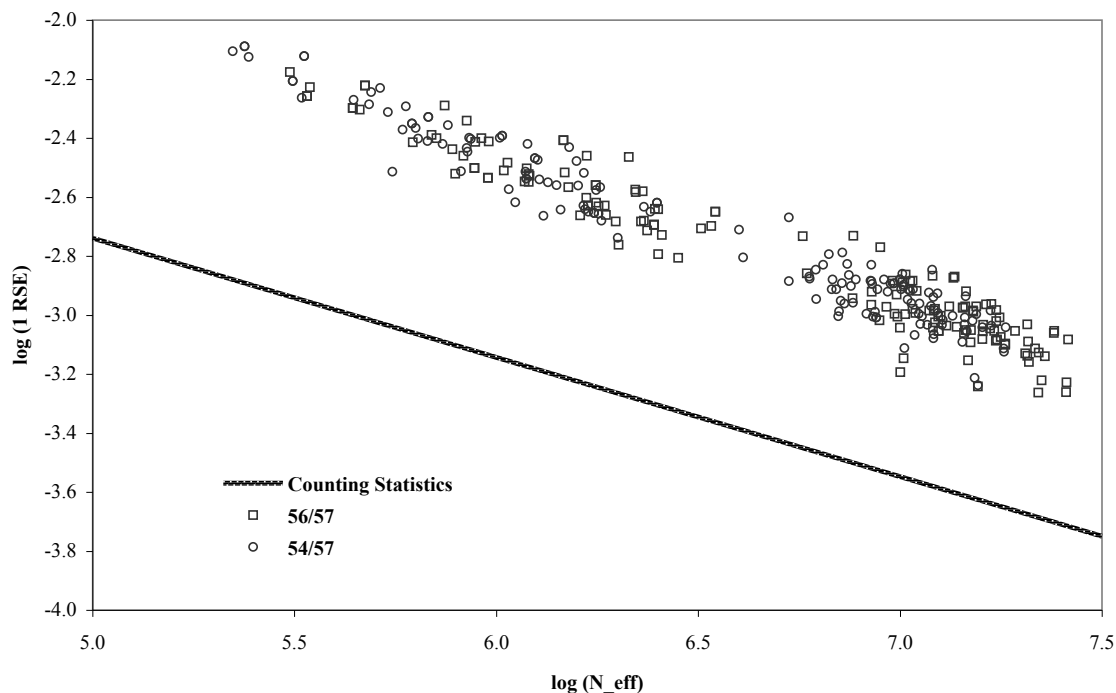


Figure 2.2. The errors (1σ RSE) in $^{56}\text{Fe}/^{57}\text{Fe}$ and $^{54}\text{Fe}/^{57}\text{Fe}$ are calculated from the variability of the standard ratios over approximately 40 seconds of acquisition per standard run. 2 standards are run during each sample processing sequence throughout all the experimental sampling, which consisted of more than 2000 samples. Signal intensity is given as the effective number of counts, N_{eff} , eq 2.2. The error due to counting statistics is based on theoretical calculations, eq 2.3. There is some drift in the signal between each mass measurement, leading to the deviation of the actual internal error (squares and circles) from counting statistics (line).

of error resulting from different analytical sessions. For each of these pairs, the error normalized deviates (END) can be calculated as

$$\text{END} = \frac{[Fe]_A - [Fe]_B}{\sqrt{\sigma_A^2 + \sigma_B^2}} \quad (2.5)$$

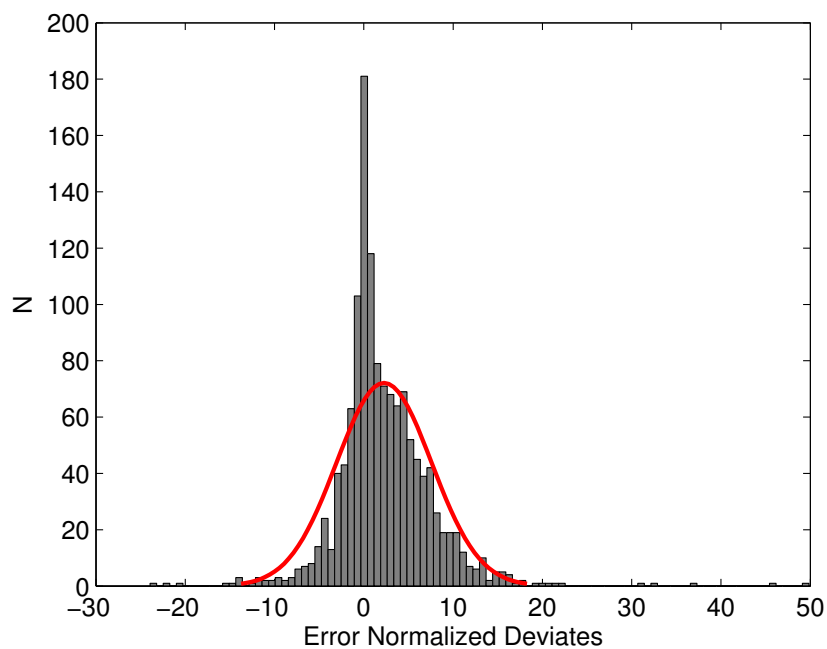
where A and B represent the replicates, as described in Section 2.4, and σ is the standard error from the ratios measured for A and B, propagated through to variations in [Fe]. The histograms for ^{54}Fe and ^{56}Fe are plotted in Figure 2.3.

Upon initial glance, the deviations appear to have a Gaussian distribution, however upon closer examination, there is a more beefy shoulder to the right of 0 for both ^{54}Fe and ^{56}Fe . This could indicate that, on average, $[\text{Fe}]_A$ is more concentrated than $[\text{Fe}]_B$. The mean of each distribution is 2.26 and 0.63 for ^{54}Fe and ^{56}Fe , respectively. By fitting the histogram data to a two Gaussian distribution (Figure 2.4) of the form

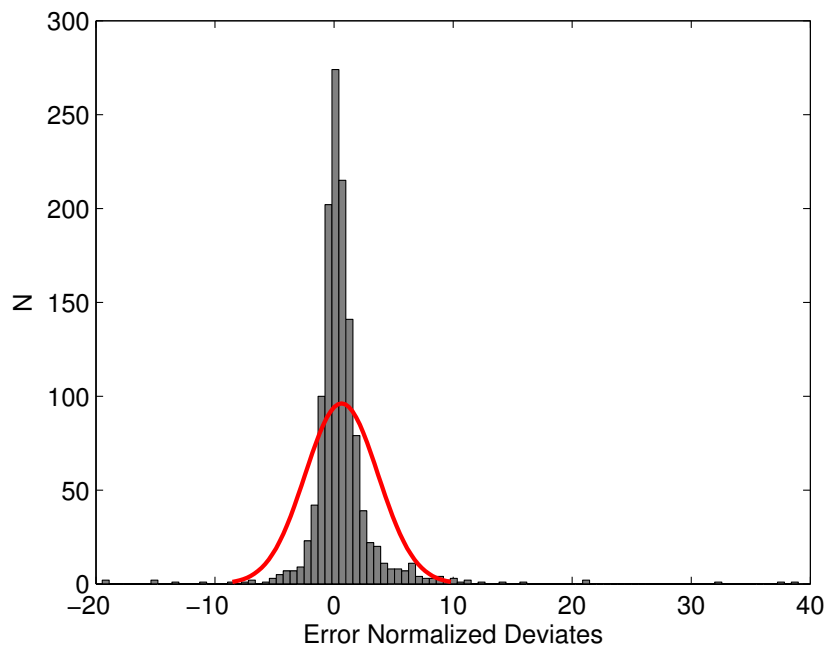
$$f(x) = a_1 \cdot \exp \left[- \left(\frac{x - b_1}{c_1} \right)^2 \right] + a_2 \cdot \exp \left[- \left(\frac{x - b_2}{c_2} \right)^2 \right] \quad (2.6)$$

we can clearly see that the shoulder is more pronounced in the ^{54}Fe data, corresponding to a higher mean, b_2 , for ^{54}Fe than ^{56}Fe in the second of the two distributions. The fit parameters are given in Table 2.3.

There is clearly a disparity between the replicates, which could stem from the method design. Each A replicate had a few hundred microliters of unacidified AQUIL in its centrifuge vial, from which 50 μL was pipetted out and placed in the B centrifuge vial. Then, 50 μL were taken out for A, the rest of the AQUIL quickly discarded, and the 50 μL placed back into A. Since vial A contained unacidified AQUIL, a varying amount of Fe atoms could have stuck to the vial walls in replicate A in addition to the 50 μL . Even though this unacidified AQUIL only remained in vial A for, at most, 10 seconds, there is evidence that this was enough time for additional atoms of Fe to adhere to the walls. Of course, the B replicate could be under-representing the true [Fe] if some atoms were lost to replicate A, meaning an average between the two values could be more accurate than A or B alone. However, the variance of



(a) ^{54}Fe END has a mean of 2.26.



(b) ^{56}Fe END has a mean of 0.63.

Figure 2.3. Histograms of external error normalized deviates (END) for 1331 pairs of kinetic experiment replicates compared to a Gaussian distribution. Both have positive means which indicate that replicate B is more concentrated on average than replicate A.

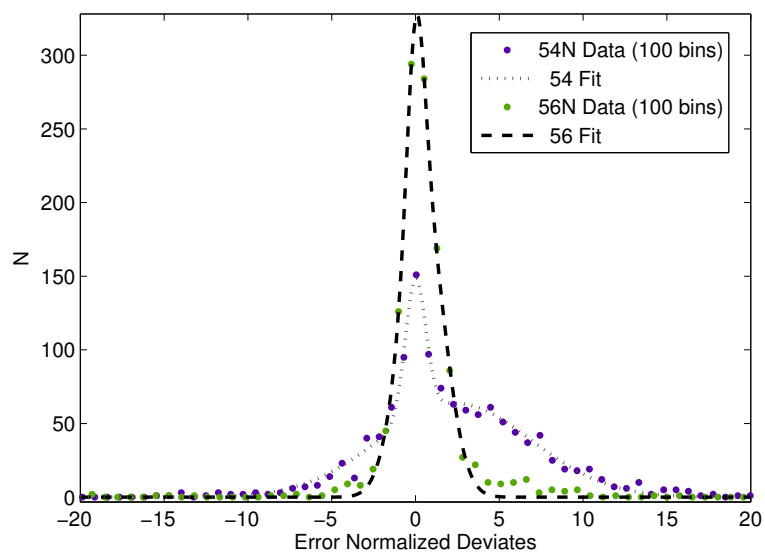


Figure 2.4. Fit of error normalized deviate histograms from ^{54}Fe and ^{56}Fe external replicates to two Gaussian distribution with bin size 100.

Parameter	Coefficients (95% confidence bounds)					
	^{54}Fe			^{56}Fe		
a_1	92.38	(83.96,	100.8)	134.8	(115.5,	154)
b_1	0.001684	(-0.06209,	0.06546)	0.02098	(-0.01919,	0.06116)
c_1	0.866	(0.7739,	0.958)	0.7338	(0.61,	0.8575)
a_2	63.58	(59.88,	67.27)	199.9	(178.3,	221.5)
b_2	2.364	(2.087,	2.642)	0.405	(0.3399,	0.47)
c_2	6.45	(6.09,	6.809)	1.807	(1.73,	1.885)
Goodness of Fit						
SSE:	780.4			871.7		
R^2 :	0.9852			0.9958		
Adjusted R^2 :	0.9837			0.9958		
RMSE:	3.991			3.045		

Table 2.3. Two Gaussian fit parameters of external replicates for kinetic experiments (based on Equation 2.6).

the RSE for all the ^{54}Fe and ^{56}Fe data for replicate A is 1.70 and 0.34, respectively, and for the B replicate is 0.22 and 0.21. The higher variance in the A replicate RSE indicates some difficulty in precisely measuring replicate A, even with the error being intensity normalized. This could be indicative of a varying number of Fe atoms eventually finding their way into solution during the course of analysis. Additionally, this wall contamination issue manifests itself more in the ^{54}Fe data than the ^{56}Fe data, indicating that ^{54}Fe was preferentially lost to the vial walls versus ^{56}Fe .

In light of this difference between replicates and because there are many sub-samples per experiment to constrain data trends, we have eliminated the A replicates from the results and discussions so as not to confuse observations.

2.6 Spike Calibration and Mass Bias

The accuracy and precision of our [Fe] measurements strongly depend on our confidence in the calibration of the ^{57}Fe spike and the mass bias correction, since they are used directly for concentration calculations. [Fe] were determined by

$$[\text{Fe}] = R_{sa} \cdot M \cdot [^{57}\text{Fe}]_{sp+sa}, \quad (2.7)$$

where R_{sa} is the measured ratio of 54/57 or 56/57, M is the respective mass bias correction factor, and $[^{57}\text{Fe}]_{(sp+sa)}$ is the concentration of ^{57}Fe in the spike and sample together, which is assumed to be entirely from the ^{57}Fe spike. This assumption leads to an error of 2% at the highest experimental $[^{56}\text{Fe}]$, since natural Fe contains approximately 2% ^{57}Fe . This secondary ^{57}Fe spike was made from a lab supply of primary ^{57}Fe spike that contained a dissolved ^{57}Fe -enriched abundance iron oxide from Oak Ridge National Laboratories. $[\text{Fe}]_{\text{tot}}$ was determined to be $101 \pm 0.5 \mu\text{M}$ in a previous calibration [94]. By mass on a 5 decimal balance (g), the new [Fe] concentration of the secondary ^{57}Fe spike (2% HNO3) was determined to be 2999 nM. Since the isotopic analysis of the spike determined the ^{57}Fe to be 93.56% abundant, then the $[^{57}\text{Fe}]$ is $2805 \pm 1 \text{ nM}$.

The primary ^{57}Fe spike had been stored for several years in a humid jar within plastic bags; a calibration check of the secondary ^{57}Fe spike was performed. The calibration consisted of spiking 4 known concentrations of Fe standard, based on careful pipette addition, in triplicate. The Fe standard concentrations were 12.3, 92.6, 308.7, and 463.1 nM. Using the isotope dilution equation (Equation 2.8), in reverse, the total Fe, $[\text{Fe}]_{\text{tot}}$, of the spike was determined.

$$C_{sa} = \frac{(R_{sp} - R_m) V_{sp} \text{}^{57}\%_{sp}}{(R_m - R_{sa}) V_{sa} \text{}^{57}\%_{sa}} C_{sp} \quad (2.8)$$

In the isotope dilution equation (Equation 2.8), C_{sp} and C_{sa} are the total Fe concentrations of the spike and sample, respectively. R_{sp} is the known 56/57 ratio of the spike, R_{sa} is the known natural ratio of 56/57, and R_m is the measured 56/57 ratio (on the Agilent ICP-MS). V is the volume of the respective solutions (10 μL and 290 μL , V_{sp} and V_{sa}) and $\text{}^{57}\%$ is the respective abundance. The mass bias correction factor was also determined in the calibration sequence and multiplied by the R_m . The blank was around 1 nM and its variation was negligible compared to the variance of C_{sp} . $[\text{Fe}]_{\text{tot}}$ for the ^{57}Fe spike was calculated to be 3240 ± 10 nM ($n = 12$), therefore its $[\text{}^{57}\text{Fe}]$ based on abundance is 3031 ± 9 nM.

This calibration of the secondary ^{57}Fe spike yields a difference of 7–8% compared to the carefully weighed dilution calculation. Since Fe contamination is a problem in all trace metal handling, there could be a natural abundance Fe contamination in the ^{57}Fe spike, meaning that the R_{sp} could be higher than previously thought and $\text{}^{57}\%_{sp}$ slightly lower. However, raising the R_{sp} value and lowering the $\text{}^{57}\%_{sp}$ in a systematic way actually leads the calibration calculation in the wrong direction, further away from the dilution calculation of the previously determined spike concentration. There could also be some systematic error in the pipette additions in creating the calibration standards.

Pending the calibration of the ^{57}Fe spike abundances and ratios to a well-known standard of similar isotopic ratios, or another calibration involving the carefully weighed volume of each Fe standard solution and spike addition instead of relying

on pipette volumes, the concentration of ^{57}Fe has been reported here as 2805 ± 1 nM. This may give slightly inaccurate $[\text{Fe}]$, however the data trends remain unaltered. This spike concentration leads to the variable $^{57}\text{Fe}_{(\text{sp+sa})}$ being 467.5 ± 0.2 nM. The sample contribution to ^{57}Fe , as previously noted, gives at most 2% error in the accuracy of the sample $[\text{Fe}]$.

The mass bias correction solutions were natural abundance Fe standards that ranged from 5 to 25 ppb, though generally the same concentration standard was run within each sequence. The known natural abundance ratio, R_{sa} , was divided by the average of its respective R_m , 54/57 or 56/57, which was measured at the beginning and end of each sequence to give

$$M = \frac{R_{sa}}{R_m}. \quad (2.9)$$

M had an average value of 1.259 ($1\sigma = 0.004$) and 1.090 ($1\sigma = 0.001$) for 54/57 and 56/57, respectively ($n = 150$). The higher mass bias correction between 54 and 57 is expected because of the longer time interval between 54 and 57 mass acquisitions compared to that between 56 and 57. The mass bias factors for each ratio are plotted together in Figure 2.5. For higher values of 54/57, the error increased because these standards were run at lower concentrations, leading to an offset from the 1/3 mass fractionation line at lower values of M .

2.6.1 Overall Error of $[\text{Fe}]$

The overall variance of our $[\text{Fe}]$ data can be estimated from each variable,

$$\sigma_{[\text{Fe}]}^2 = \sigma_{R_m}^2 \left(\frac{\partial[\text{Fe}]}{\partial R_m} \right)^2 + \sigma_M^2 \left(\frac{\partial[\text{Fe}]}{\partial M} \right)^2 + \sigma_{^{57}\text{Fe}}^2 \left(\frac{\partial[\text{Fe}]}{\partial [^{57}\text{Fe}]} \right)^2, \quad (2.10)$$

where σ is the absolute standard deviation of the respective variables. The variance of the data is dominated by the mass bias correction factor, owing to the lower intensities at which the standards were run for multiple sessions. On average the relative error is 4% or 5%, though at low concentrations near the limit of detection it

Fudge Factor for Mass Bias on Agilent 7500 ICP-MS

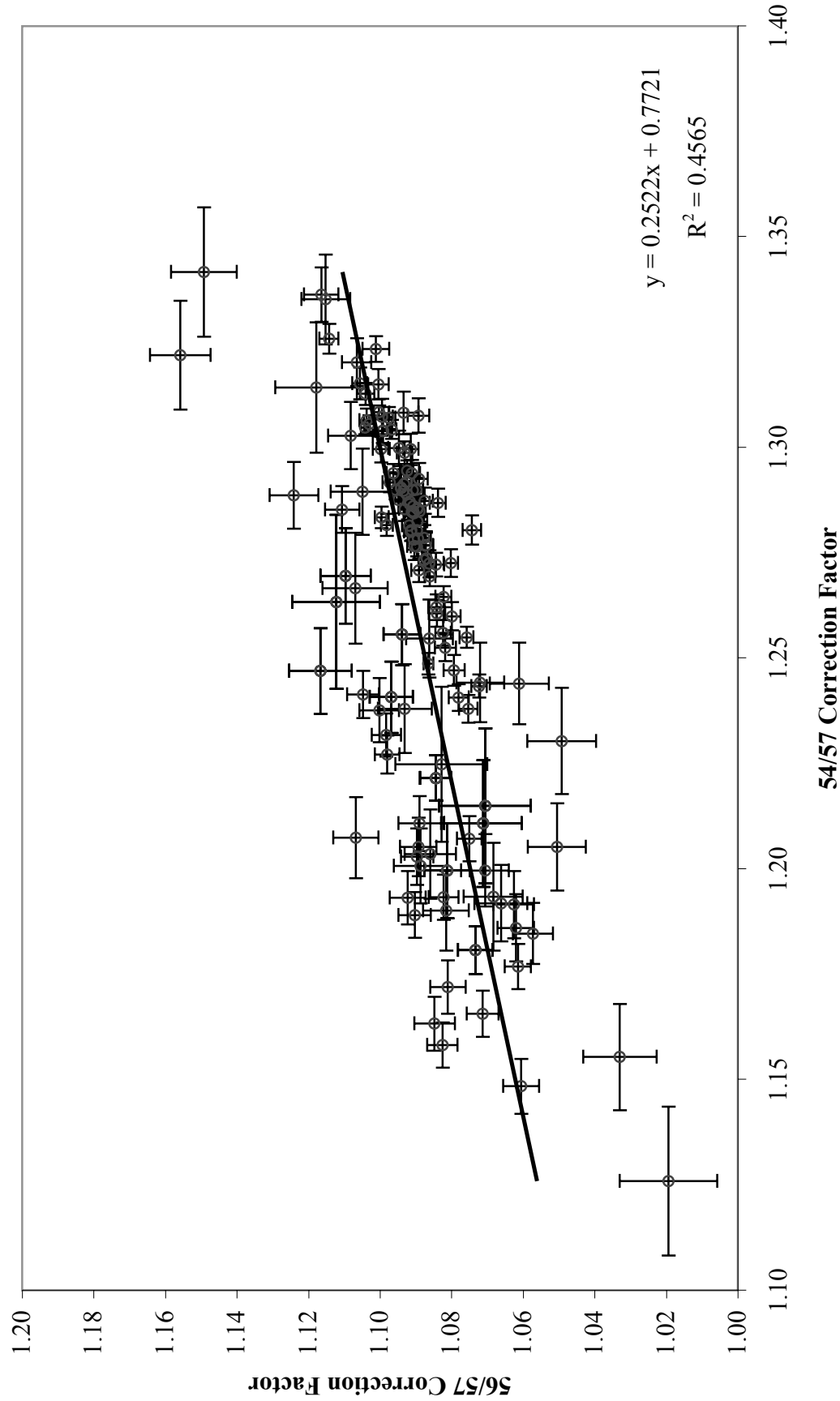


Figure 2.5. Mass biases are calculated using eq 2.9. Mass bias should follow a 1/3 line given the measured ratios. Low signal intensity of the standards cause the error to increase and mean mass bias to deviate from the 1/3 line.

gets as high as 20%. However, since we are determining the mean [Fe] over a course of ratio measurements, the estimated error in the mean is reduced as the square root of the number of measurements increases. The overall standard error of the mean is typically less than 1%, though it gets as high as 2% or 3% around the limit of detection. Including the error of the sample contribution to mass 57, the overall error of [Fe] is about 3–5% across the range of experimental concentrations.

2.7 Fe Isotope Experimental Setup

Artificial seawater from 3 batches (4L each) was mixed together to create an identical medium for all experimental bottles. Natural Fe (418 μL , 1000 ppm, 2% HNO_3 , High Purity Standards) and fresh DFB powder (5.33 mg) were combined (1:1 ratio) in a 100 mL solution at pH 3 and left in the dark for 2 days to equilibrate. After rinsing once with AQUIL, 80 bottles (125 mL, Nalgene, LDPE) were filled with 100 mL of AQUIL. The FeDFB was added to make 30 bottles with 1000 nM FeDFB and 48 with 400 nM FeDFB. 21 of the 48 FeDFB 400 nM AQUIL bottles had an additional spike of DFB (20 μL , 3 mM) added to bring the Fe:DFB ratio to 1:2.5 or 400 nM Fe to 1000 nM DFB. Ferrihydrite and clay particles were added via pipette addition, and the mass of each addition was determined from identical pipette volumes that were dried down. Bottles made up in triplicate are indicated with a “T.” Ferrihydrite was freshly precipitated from $\text{FeCl}_3 \cdot 6\text{H}_2\text{O}$ (8.92 g) around pH 8 and added to 400 nM and 1000 nM Fe concentration bottles to create the following particle concentrations (mg/L): 3164 (T), 910, 320 (T), 3.1, and the smallest two concentrations, which were not accurately weighable and estimated to be 0.3 (T) and 0.03. Clay was added to obtain the following concentrations (mg/L): 2468 (T), 640, 116 (T), 2, 0.2 (T), and 0.02. The 400 nM Fe, 1000 nM DFB AQUIL bottles had ferrihydrite and clay added to them to make 9 bottles with the same particle concentrations and replicates as those done in triplicate.

Goethite, forams, and opal were weighed and added to 1000 nM FeDFB bottles to create one bottle each of 2435, 2491, and 2454 mg/L particles, respectively.

Controls (no particles) were also present in triplicate for 400 nM FeDFB, 1000 nM FeDFB, and 400 nM Fe-1000 nM DFB.

All bottles were placed on a shaker table in the dark at ambient temperature (19–20 °C) for 3 months.

[Fe]nM 1000		
[Particle] mg/L	DFB-1000nM	
2500	x	shaded in triplicate
625	x	
125	x	
2.5	x	
0.25	x	
0.025	x	
Control	x	

[Fe]nM 400		
[Particle] mg/L	DFB-400nM	DFB-1000nM
2500	x	x
625	x	
125	x	x
2.5	x	
0.25	x	x
0.025	x	
control	x	

Table 2.4. Isotope experiment sample matrix. All bottles were 125 mL, cleaned HDPE, and shaded experiments had 3 separate bottles. Two sets of 1:1 ratios of FeDFB were made at 1000 nM (top) and 400 nM (bottom) and an additional set of bottles with 400:1000 nM FeDFB. Particle concentrations are within an order of magnitude of listed values, see text for exact concentrations for each particle type. Controls have no particles.

2.8 Sample Processing

Samples were purified and concentrated using a two-step column procedure, adapted from two methods [95, 96]. Anion exchange resin (AG-MP-1, BioRad Laboratories) for the column purification was leached progressively in 10% RG HCl (1 week) then 1% HCl (few days), rinsing several times with milliQ in between, and stored in 0.5% HNO₃. Teflon vials (15 mL, 22 mL) were similarly leached over low heat and stored (0.5% HNO₃).

Filtered experiment samples (0.2 μm , 10 mL) were acidified (500 μL , conc. HNO₃), from which a sub-sample (50 μL) was taken for [Fe] analysis on the agilent ICP-MS, as described in the Section 2.7. The sample was dried down and reconstituted (1 mL, 7 N HCl, 0.001% H₂O₂). The first column consisted of anion exchange resin (1.8 mL, pre-cleaned) that was additionally cleaned after suspension and settling within the column (3 \times (7 mL 0.5% HNO₃, 2 mL water)). The column was pre-conditioned (6 mL, 7 N HCl, 0.001% H₂O₂). Each sample was added to a fresh column; resin was not re-cleaned nor re-suspended for future sample use. The next fraction was eluted and discarded (30 mL 7 N HCl, 0.001%). Within the rinsed sample vial (0.5% HNO₃), the Fe elution was collected (10 mL, 2 N HCl, 0.001% H₂O₂). The final elution was dried down and reconstituted in 1 mL (500ppb Ni, 0.5% HNO₃). A sub-sample (25 μL) of this final 1 mL was taken for [Fe] analysis on the Agilent ICP-MS. Total column recoveries were estimated to be $97 \pm 5\%$.

Column blanks (1 mL, 7 N HCl, 0.001% H₂O₂) were processed alongside samples and were approximately 23 ± 9 ng Fe ($1\sigma, n = 5$), which was 1% to 10% of the total amount of dissolved Fe in the samples.

The two highest clay and ferrihydrite particle concentrations (~ 600 to 3000 mg/L) contained too little Fe in the 10 mL filtered volume for the column purification method and had 20% to 50% Fe contamination. These higher particle concentration samples would need to have a larger filtrate volume for analysis, or a smaller resin volume in the column, both of which should be tested in further method development for matrix purification and complete Fe recovery. These high particle concentration data

are omitted.

2.8.1 Sample Analysis

Samples were analyzed for their isotopic composition using the instrumental method described in John and Adkins [96]. Samples were concentration matched to an Fe standard and run in a bracketed sequence, standard-sample-standard, on a Neptune multi-collector ICP-MS. Instrument background levels were measured previous to each bracket and subtracted from the measured voltages at each mass. The isotopic composition is defined relative to the standard,

$$\delta^{56}\text{Fe} = \left(\frac{\left(\frac{56}{54}\right)_{\text{sample}}}{\frac{1}{2} \left(\left(\frac{56}{54}\right)_{\text{IRMM before}} + \left(\frac{56}{54}\right)_{\text{IRMM after}} \right)} - 1 \right) \cdot 1000. \quad (2.11)$$

The isotopic standard reference material was IRMM-14.

2.9 Data Quality

This section contains subsections relating to internal error, intermediate and external error of replicates, and chemical blanks.

2.9.1 Internal Error

Analogous to the previous set of samples run on the Agilent ICP-MS, our ability to measure ratios on the Neptune ICP-MS can be compared to the error predicted by counting statistics. Comparing the relative standard error of the measured 56/54 ratios and their predicted estimated error versus N_{eff} gives Figure 2.6. From this figure, we can see that the internal error follows counting statistics, however our error is higher on average by 0.2 log units, or a factor of 1.6, due to internal variability during the 4-minute sample acquisition. The ability to measure ratios with this level of precision becomes worse for lower values of N_{eff} , where the background variance becomes more important. Our total internal error for a bracketed sample must include

Fe Standard and Sample Ratios on Neptune ICP-MS

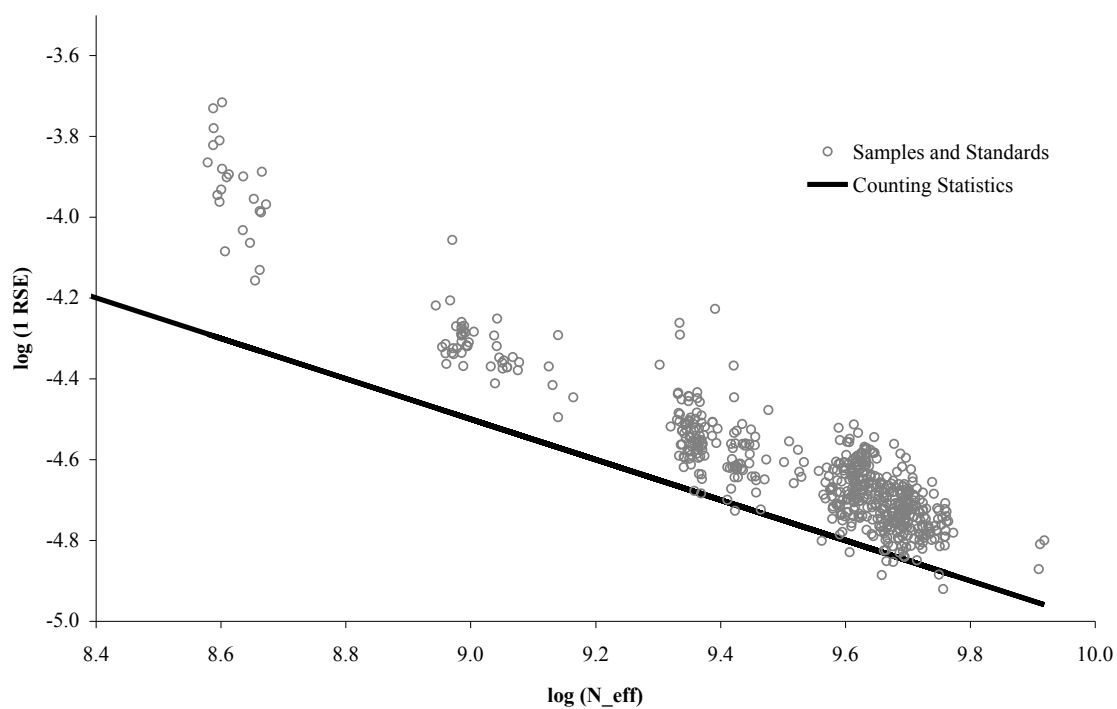


Figure 2.6. Relative standard error (RSE) of sample and standard data (grey circles) are calculated from the variability of the $^{56}\text{Fe}/^{54}\text{Fe}$ ratios over 54 consecutive 4.2 second cycles of data. Counting statistics error (solid line) calculated from theory, eq 2.3.

the variance from the averaged standards run before and after the sample. The total internal error of a standard-bracketed sample, following propagation of error of Equation 2.11, is

$$\sigma_{internal}^2 = \sigma_{sample}^2 + 2\left(\frac{1}{4} \cdot \sigma_{standard}^2\right). \quad (2.12)$$

Since the samples are concentration matched to the standards and thus have similar intensities, we can assume the internal error will be the same for each, and thus $\sigma_{internal}$ reduces to

$$\sigma_{internal} = \sqrt{\frac{3}{2}} \cdot \sigma_{sample}. \quad (2.13)$$

2.9.2 Intermediate Error and External Error

This sample analysis contained intermediate replicates of purified samples run during two or more analytical sessions and external replicate bottles with separate purification and analysis. By comparing pairs of intermediate (69 pairs) and pairs of external replicates (60 pairs), we can estimate the amount of error added from one sample analysis to the next and from sample processing, respectively. For example, the total intermediate error should sum in quadrature as

$$\sigma_{intermediate-total} = \sqrt{\sigma_{internal}^2 + \sigma_{intermediate}^2}, \quad (2.14)$$

so then we can estimate $\sigma_{intermediate}$ based on $\sigma_{internal}$ by calculating the error normalized deviates (END) of the replicate pairs

$$\text{END} = \frac{R_1 - R_2}{\sqrt{\sigma_1^2 + \sigma_2^2}}, \quad (2.15)$$

where R is the 56/54 standard corrected ratio and σ is $\sigma_{internal}$ as calculated in Equation 2.15. If R is normally distributed with variance σ^2 , then the END will be normally distributed with a standard deviation of 1 for $\sigma_{internal}$, by definition.

The distribution of END for the intermediate pairs (IEND) is shown in Figure 2.7a and appears as a Gaussian distribution. The standard deviation of our IEND is 1.37,

which follows from Equation 2.14 that

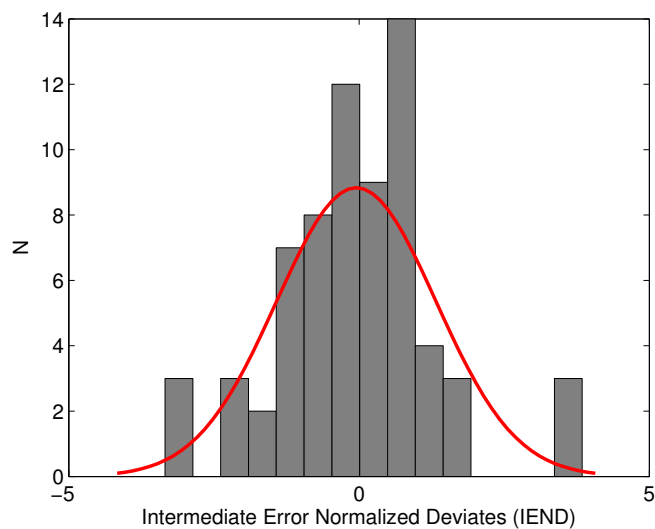
$$\sigma_{intermediate} = \sqrt{1.37^2 - 1} = 0.94. \quad (2.16)$$

This means that, between acquisitions of the same sample or between multiple analytical sessions, there is an additional source of error that is equal to 94% of internal error, nearly doubling our error.

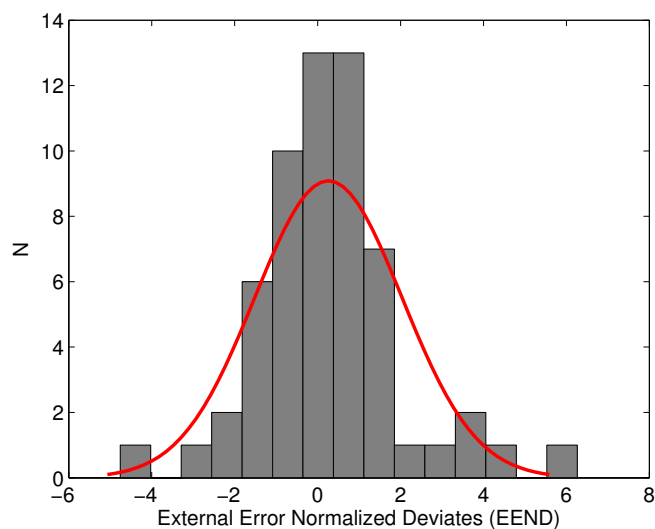
Similarly to the intermediate error, the distribution of END for the external pairs (EEND) is shown in Figure 2.7b, and its error includes internal, intermediate, and external sources, representing, respectively, reproducibility within 1 acquisition, reproducibility between analytical sessions (including some sample handling via pipette dilution), and reproducibility between sample processing, including filtering and purification steps.

$$\sigma_{external-total} = \sqrt{\sigma_{internal}^2 + \sigma_{intermediate}^2 + \sigma_{external}^2} \quad (2.17)$$

The standard deviation of this EEND is 1.78, meaning that the total amount of error from sample processing, $\sigma_{external}$, is a factor of $1.13 \times \sigma_{internal}$. The largest single source of error in the entire sample processing and analysis is the reproducibility of sample handling (40%), and to a slightly lesser extent reproducibility of analysis (28%) and internal reproducibility within an acquisition (32%).



(a)



(b)

Figure 2.7. Error normalized deviates (END) histograms for 69 pairs of intermediate replicates (a) and 60 pairs of external replicates (b) with a Gaussian fit overlay. IEND standard deviation is 1.37, which means from further calculations that our intermediate error, between multiple analytical sessions, nearly doubles our error. EEND standard deviation is 1.78, and from these calculations, the single largest source of error is sample handling, followed by similar reproducibility of analysis and within an acquisition.

2.9.3 Chemical Blanks

The effect on the $\delta^{56}\text{Fe}$ values from Fe contamination can be estimated by taking into account the $\delta^{56}\text{Fe}$ of the blank

$$\delta^{56}\text{Fe}_{total} = \delta^{56}\text{Fe}_{sample} \cdot f_{sample} + \delta^{56}\text{Fe}_{contaminant} \cdot f_{contaminant} \quad (2.18)$$

where the overall measured value is $\delta^{56}\text{Fe}_{total}$. The contributing factors, f , sum to 1 and represent the relative contribution of the actual $\delta^{56}\text{Fe}$ of the sample itself and the contaminant. $\delta^{56}\text{Fe}_{contaminant}$ is around 0‰ since its largest contributors are probably dust from the air or dirt from the column resin. $f_{contaminant}$ is known, approximately, for each sample, since the dissolved [Fe] was measured before and after column purification (the single largest sample-handling step). Assuming the column recovery was 97%, the samples have been corrected for $f_{contaminant}$, which amounted to 1% to 10% of Fe in the samples.

Chapter 3

Kinetics of Ferrihydrite and FeDFB

3.1 Introduction

Particle residence times in the ocean vary and can be short enough for the kinetics of dissolved Fe exchange with particles to matter [69]. Models of variations in particle residence time and trace metal compositions have shown that dissolved concentrations depend strongly on particle flux [28].

Precipitation and dissolution rates of the particulate matter are two factors affecting dissolved [Fe]. There are few studies of Fe^{3+} dissolution and precipitation reactions and rates for various iron oxides in natural seawater conditions, high salinity and pH 8. Two examples include precipitation and dissolution of Fe^{3+} from ferrihydrite or dust in the presence of ligands or siderophores [97, 89]. There have been kinetic and equilibrium studies of Fe^{3+} in the presence of various particle types [68, 69], however, there is no existing literature on the absorption and desorption rates of ligand-bound Fe(III) to and from various particles. The strong affinity of siderophores for Fe will also affect the ability of particles to scavenge Fe as they fall through the water column.

These experiments, coupled with modeling, quantify the important parameters for exchange between DFB bound Fe(III) with amorphous, freshly precipitated ferrihydrite, namely: adsorption, desorption, dissolution, and precipitation. The tracer in the dissolved phase allows us to monitor two pools of Fe by measuring the removal of ^{54}Fe from the dissolved phase and the appearance of ^{56}Fe from the particulate phase. The experiments were run in parallel with other marine particle types, including goethite, montmorillonite, foraminifera (forams), and pulverized fossilized diatoms. Those experiments are discussed in more detail in Chapter 4.

3.2 Experimental Setup

Chapter 2 describes the detailed setup for these experiments. Our dissolved phase ^{54}Fe tracer was equilibrated with DFB, a naturally occurring siderophore, before addition to AQUIL. After 2 more days of equilibration, freshly precipitated ferrihydrite, of natural isotopic abundance, was added in various quantities. Sub-samples (50 μL) were drawn off and filtered (0.2 μm , polypropylene). A total of 222 sub-sample pairs over 104 days were analyzed for dissolved ^{54}Fe and ^{56}Fe at 5 ferrihydrite concentrations, 0.02 to 200 mg/L, including one replicate bottle at 20 mg/L, referred to as Set 1. A total of 148 sub-sample pairs over 38 days were analyzed for dissolved ^{54}Fe and ^{56}Fe at 4 ferrihydrite concentrations in a higher range, 33 to 570 mg/L, referred to as Set 2. A control experiment with no particles was sub-sampled 36 times over 104 days. An experiment with only ferrihydrite and no FeDFB was sub-sampled 37 times over 104 days. A desorption experiment, where a few milliliters of FeDFB were equilibrated with ferrihydrite for 2 days then placed into AQUIL, was sub-sampled 22 times over 58 days.

3.3 Results

3.3.1 Absorption

Plots of ^{54}Fe and ^{56}Fe in the presence of ferrihydrite have been adjusted so that their scale bars highlight the full range of change in $[\text{Fe}]$ for all particle concentrations. For ^{54}Fe , the y-axis has been set to 450 nM for Set 1 experiments with the lower range of ferrihydrite concentrations, and to 600 nM for Set 2 because Set 2 began at higher initial values of tracer. To normalize for these differences in starting concentration between Set 1 and Set 2, there are additional figures where the starting concentration is normalized to 1. ^{56}Fe plots have a maximum of 350 nM, the upper limit of the observed ^{56}Fe across all particle concentrations. Plots of $[\text{Fe}]_{\text{total}}$ include both ^{54}Fe and ^{56}Fe , so the net $[\text{Fe}]$ in the presence of ferrihydrite can be visualized.

Measurements of ^{54}Fe and ^{56}Fe in the dissolved phase have been corrected for

the loss of ^{54}Fe and ^{56}Fe in the control. The control (Figure 3.2) fit yields a linear slope of approximately 0.4 nM Fe lost per day. A linear relationship indicates a zeroth-order reaction, independent of $[\text{Fe}]$ or site concentration on the bottle walls. The addition of Fe back into the experiments to account for wall loss was split proportionally according to the amount of ^{54}Fe and ^{56}Fe present in the dissolved phase on any given day, assuming any fractionation between the isotopes is negligible.

Experiment Set 1 with the lower ferrihydrite range, including one replicate particle concentration, is shown in Figure 3.3. Experiment Set 2, four ferrihydrite concentrations over a higher range, is shown in Figure 3.4.

Overall, both sets of adsorption experiments show a decrease in total Fe, especially at higher particle concentrations, suggesting that DFB is lost from solution or that DFB is not able to compete for its full capacity of dissolved Fe in the presence of a fresh, labile iron hydroxide. The removal of ^{54}Fe from the dissolved phase scales with particle concentration and has an exponential decay trend, indicating possible first-order rate dependence. ^{54}Fe has a nearly linear increase, followed by a gradual plateau, indicating a possible zeroth-order reaction mechanism until saturation of the dissolved phase is reached. The rate of decrease in Set 2 is faster than in Set 1, suggesting that there is a difference between the two sets of precipitates or the experimental conditions. The lower particle concentrations in Set 1, 0.02 and 0.2 mg/L of ferrihydrite, are barely able to compete with the FeDFB given their relatively small effect on ^{54}Fe dissolved.

3.3.2 Desorption

In the experimental bottle with no tracer and no DFB, there is an insignificant amount of Fe released from the particulate phase in the absence of the ligand (Figure 3.5), underscoring the importance of ligands for moving Fe to the dissolved phase.

The desorption experiment is shown in Figure 3.6, with a particle concentration of approximately 660 mg/L. There is an increasing amount of ^{56}Fe released from the particle phase, but no enhanced appearance of ^{54}Fe , suggesting that the uptake of ^{54}Fe is irreversible. Irreversible absorption is consistent with the continuous exponen-

tial decay observed with the ^{54}Fe tracer. The ^{56}Fe appearing in the dissolved phase in this desorption experiment is ligand-promoted dissolution of ferrihydrite, since in the absence of ligand (Figure 3.5) there was no significant dissolution.

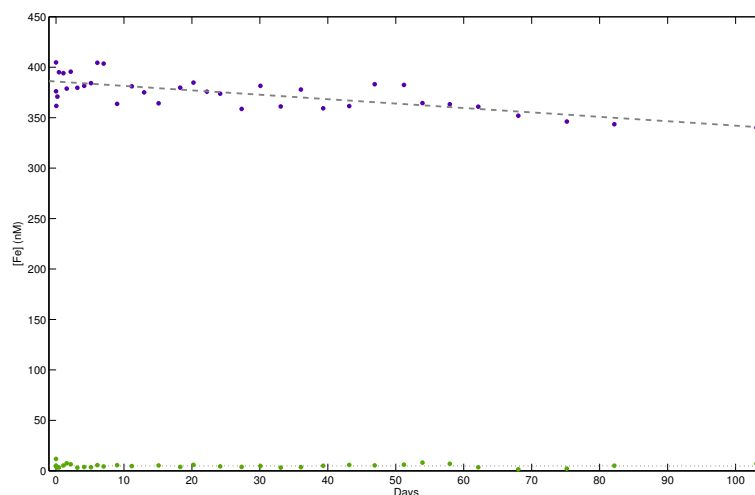


Figure 3.1. Control (no particles) experiment sub-sampled over 100 days. Linear regression yields a slope of approximately -0.4 nM Fe/day. This loss of Fe was added back into the particle experiments in proportion to the amount of ^{54}Fe and ^{56}Fe measured in the dissolved phase. This correction accounts for wall loss throughout the experimental run.

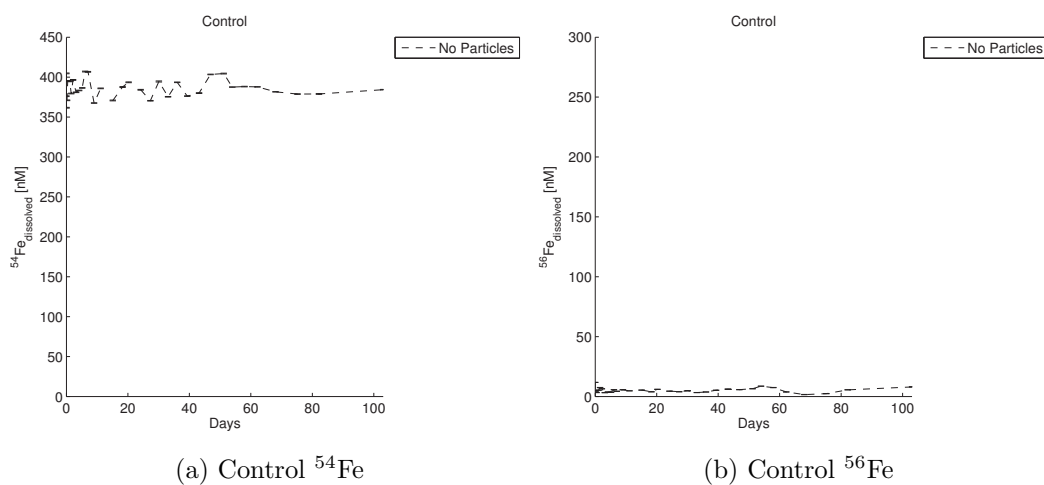
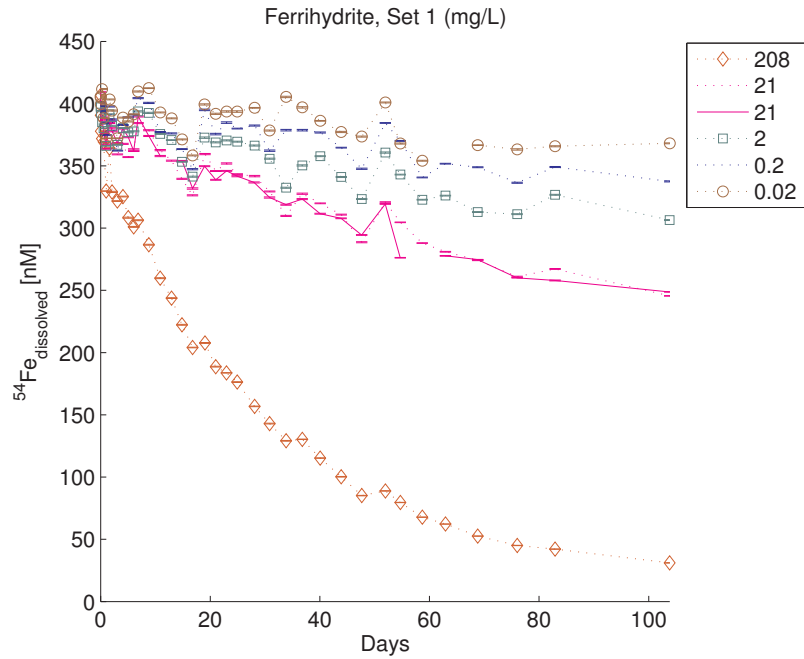
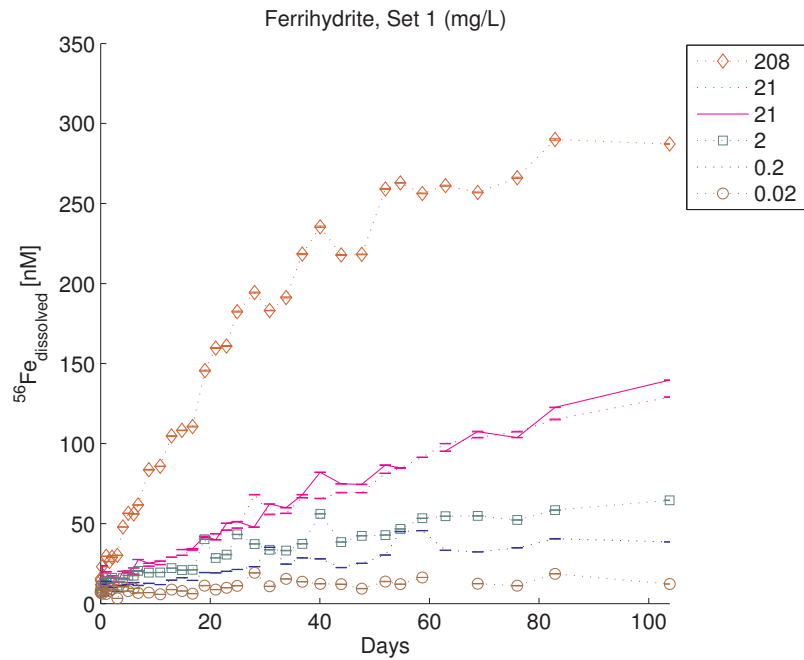


Figure 3.2. Control experiments, corrected from their own slope shown in Figure 3.1. (a) Fluctuations in $[\text{Fe}]$ most likely result from ambient temperature variations, otherwise the tracer remains fairly constant. (b) Very little natural abundance Fe appears in the control, indicating that the experimental bottles are free from contamination.

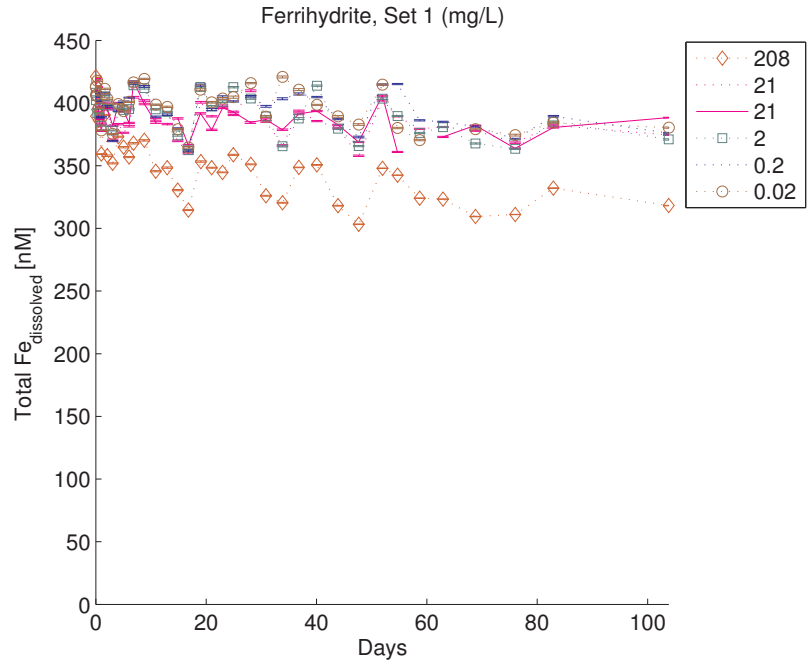


(a) The tracer, ^{54}Fe , decreases over time and scales with particle concentration.

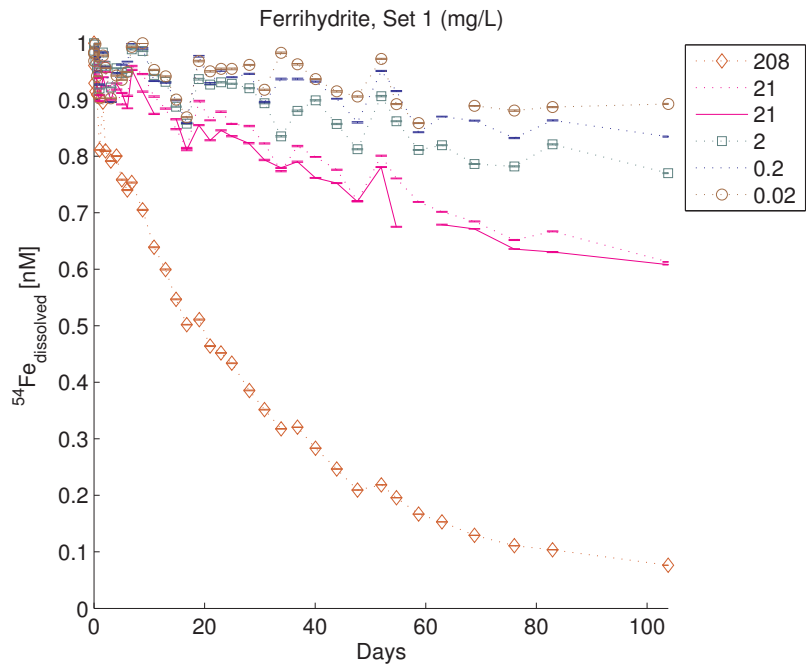


(b) The appearance of ^{56}Fe from ferrihydrite increases over time and scales with particle concentration.

Figure 3.3. Ferrihydrite Set 1 experiments of $[\text{Fe}]$ versus time. Legend is particle concentration, mg/L.

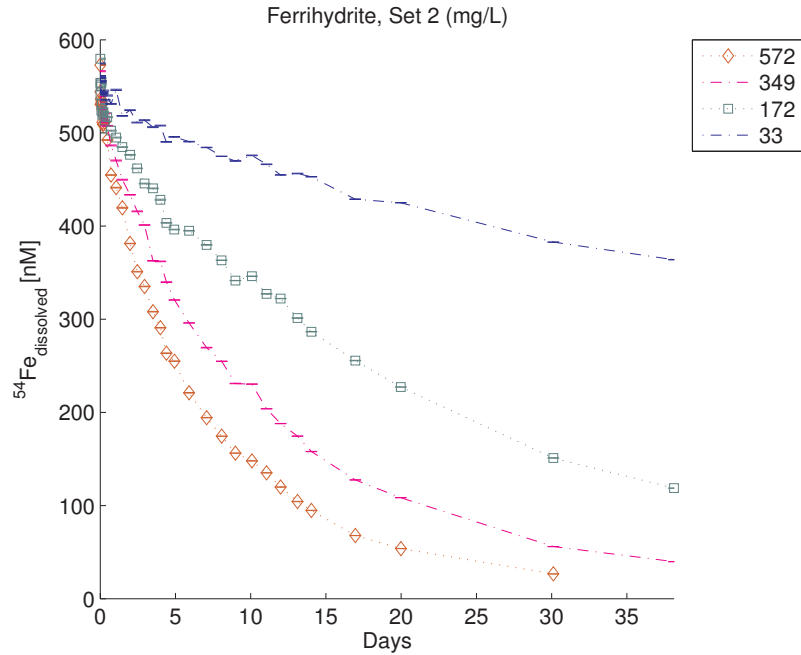


(c) The overall change in $[\text{Fe}]_{\text{total}}$ (^{54}Fe + ^{56}Fe), is plotted over time.

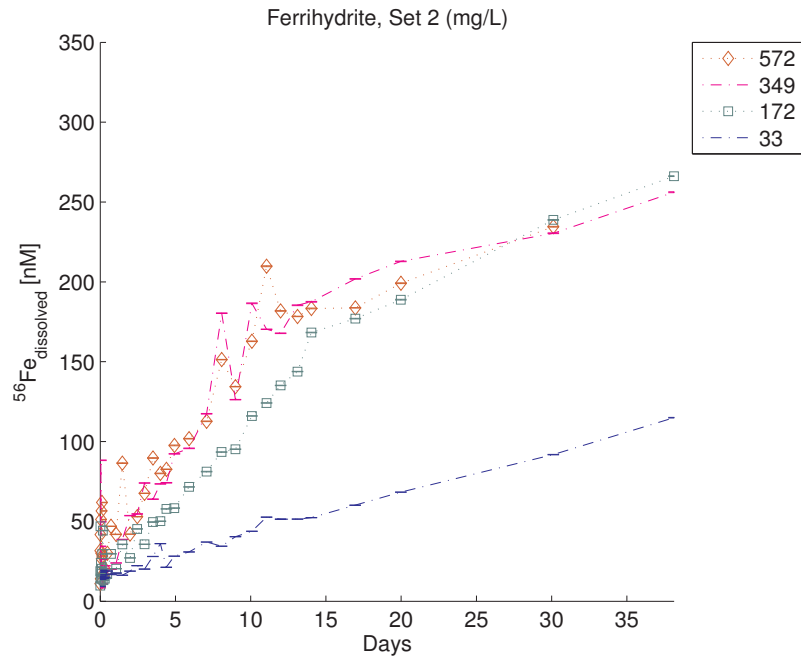


(d) The normalization is performed for easy comparison to Ferrihydrate Set 2 experiments that began at a higher ^{54}Fe .

Figure 3.3. Ferrihydrate Set 1 experiments of $[\text{Fe}]$ versus time. Legend is particle concentration, mg/L.

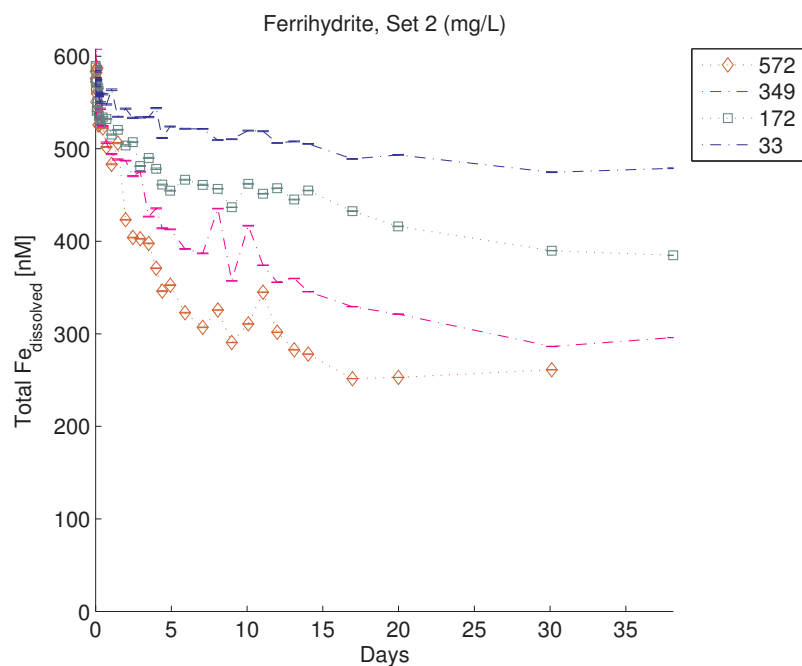


(a) ^{54}Fe decrease scales with particle concentration and appears to decrease at a faster rate than Set 1.

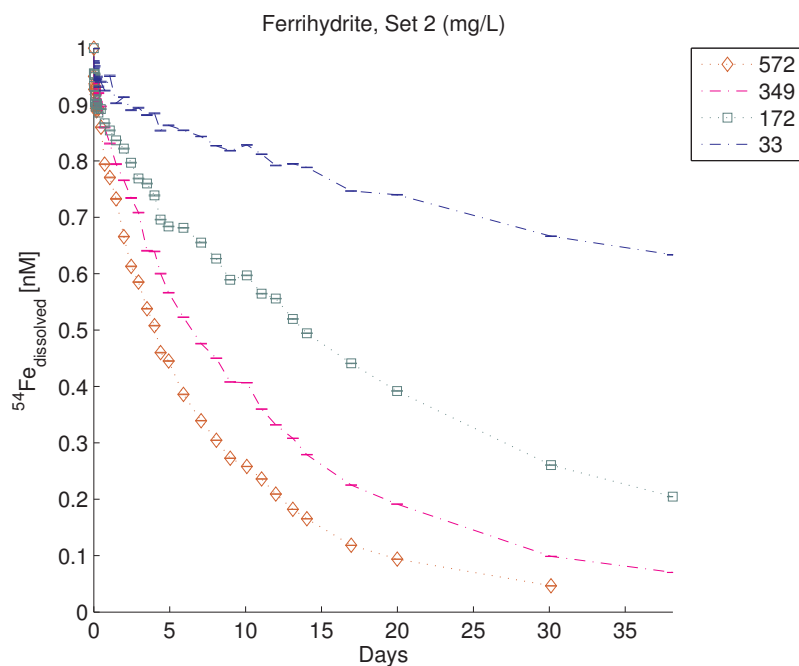


(b) There is not as much of an increase in ^{56}Fe as compared to Figure 3.3b. The three highest particle concentrations reach a similar plateau, suggesting that saturation has been reached.

Figure 3.4. Ferrihydrite Set 2 experiment of $[\text{Fe}]$ versus time. Legend is particle concentration, mg/L.



(c) $[\text{Fe}]_{\text{total}}$



(d) From the normalization, we can see a faster, higher magnitude decrease in ^{54}Fe over time compared to Figure 3.3d.

Figure 3.4. Ferrihydrate Set 2 experiment figures of $[\text{Fe}]$ versus time. Legend is particle concentration, mg/L.

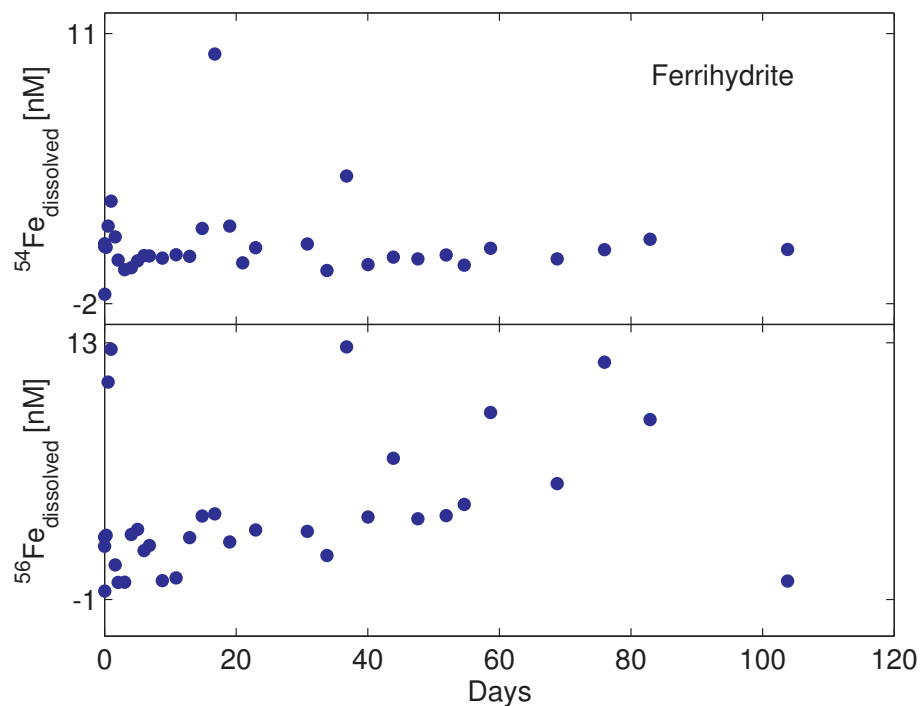
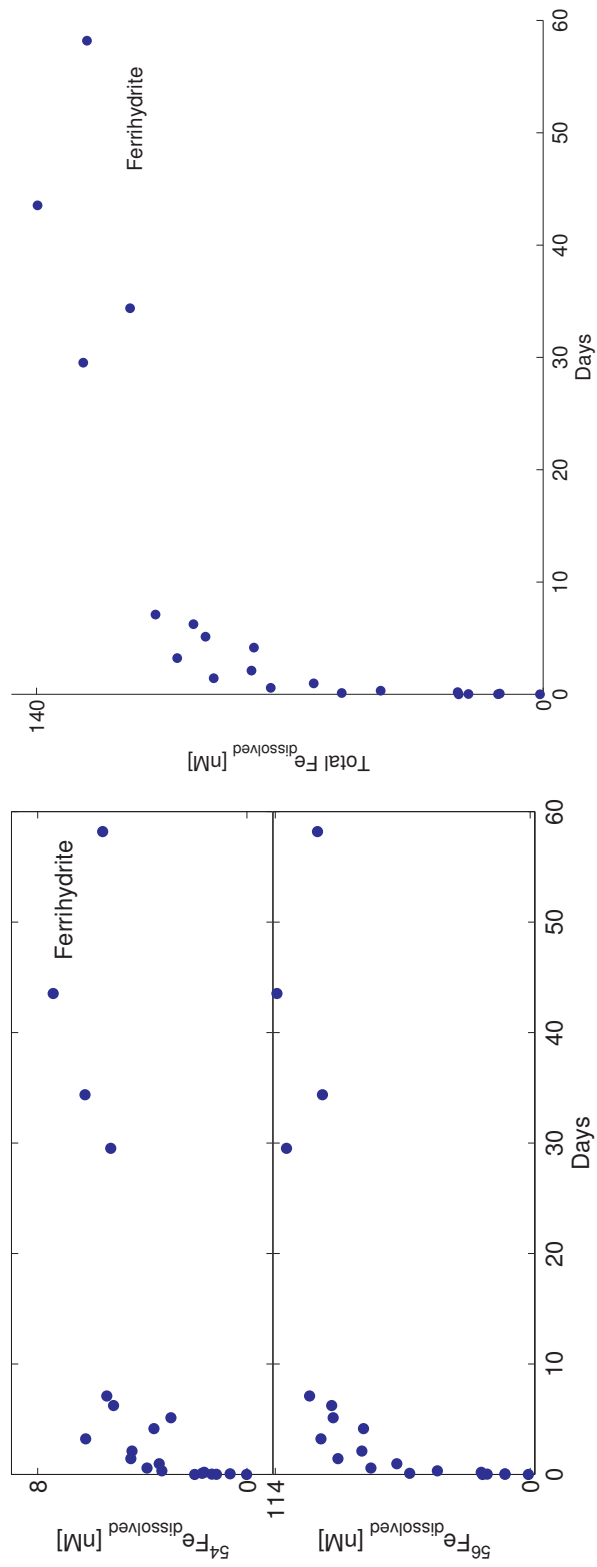


Figure 3.5. This experiment contains only ferrihydrite, 20 mg/L, in AQUIL and no added tracer or DFB. Very little Fe remains in the dissolved phase without DFB present. The max and min y-axis values have been adjusted to maximize the [Fe] range for each isotope, and the scale is the same. For our experiments with DFB, the approximation is valid that all dissolved Fe is FeDFB. ^{54}Fe is consistently around 0 nM with a couple outlier spikes in concentration. ^{56}Fe has some contamination or discrete dissolution spikes. Overall, the slight increasing trend in ^{56}Fe of several nM may not be significant as these [Fe] are around our limit of detection.



(a) ^{54}Fe (top) and ^{56}Fe (bottom).

(b) Total Fe, sum of ^{54}Fe and ^{56}Fe .

Figure 3.6. This experiment shows the increase of ^{56}Fe in the dissolved phase, from natural abundance Fe in the ferrihydrate. Y-axis scale bars have been adjusted to the maximum concentration reached by ^{54}Fe and ^{56}Fe , respectively. The amount of ^{54}Fe in the dissolved phase relative to ^{56}Fe is consistent with a natural abundance Fe increase, indicating dissolution of the ferrihydrate. Since there is no enhanced appearance of ^{54}Fe , the tracer seems to have irreversibly absorbed onto the particulate matter during the initial equilibration time before addition to AQUIL.

3.4 Discussion

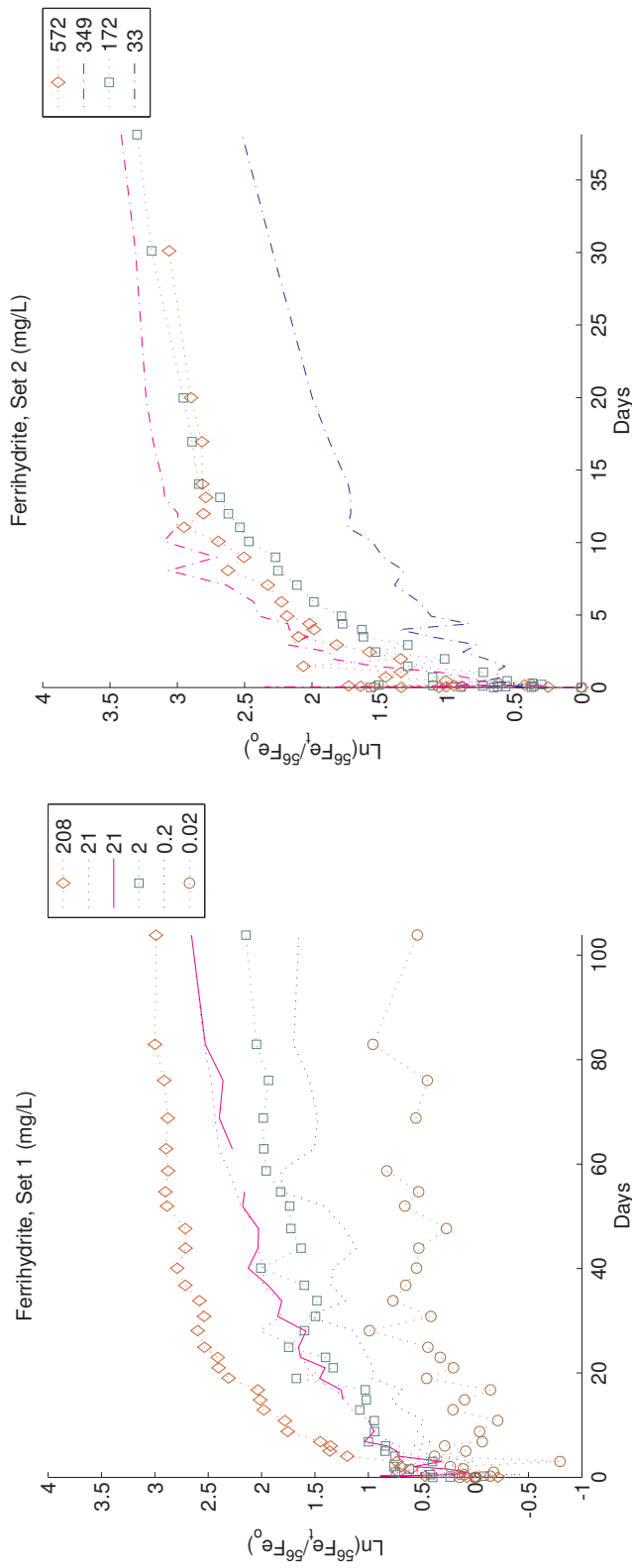
Understanding the mechanisms is key to explaining the differences among adsorption rates and dissolution rates. The experimental conditions can also assist in clarifying or eliminating possible mechanisms. By fitting the ^{54}Fe and ^{56}Fe data from (a) and (b) in Figures 3.3 and 3.4 to the following equation,

$$\frac{\text{Fe}_t}{\text{Fe}_o} = e^{-kt}$$
$$\ln\left(\frac{\text{Fe}_t}{\text{Fe}_o}\right) = -kt \quad (3.1)$$

we can determine if there is a linear relationship between $\ln(\text{Fe}_t/\text{Fe}_o)$ and time, where the slope is a rate constant ($k_{\text{sorb-part}}$) for each particle concentration experiment. Figure 3.7 shows the results of fitting both ^{54}Fe and ^{56}Fe to Equation 3.1 for each set of adsorption experiments.

A first-order mechanism is likely the cause of the linear relationship among the ^{54}Fe data from day 2 after particle addition through day 104. In stark contrast, there is no linear relationship for the ^{56}Fe data, possibly indicating higher-order kinetics or a zeroth-order mechanism followed by a saturation plateau. The ^{56}Fe data do not support a simple forward and reverse rate constant pair; the underlying mechanisms are different. The ^{54}Fe data first-order rate dependence on particle concentration is confirmed by plotting $k_{\text{sorb-part}}$ versus particle concentration for each set of experiments (Figure 3.8). The smallest concentrations (< 2 mg/L) are omitted because their slopes with error are indistinguishable from the control. The two experiment sets each have their own robust linear agreement, with slopes of k_{sorb} ($k_{\text{sorb-part}}/[\text{particle}]$) of $2.3 \times 10^{-4} \text{ (mg/L)}^{-1} \text{ day}^{-1}$ and $1.2 \times 10^{-4} \text{ (mg/L)}^{-1} \text{ day}^{-1}$.

There is also a notable difference in the rate of ^{56}Fe appearance for the two sets of ferrihydrite experiments. The higher range of particle concentration experiments with the faster k_{sorb} appears to have a slower and overall lower increase of ^{56}Fe compared to the slower k_{sorb} experiment set. This seems counterintuitive since one might expect that higher particle concentrations would lead to faster adsorption and



(a) $\ln {}^{56}\text{Fe}$, Set 1

(b) $\ln {}^{56}\text{Fe}$, Set 2

Figure 3.7. Plotting the natural log of the relative Fe (Fe_t/Fe_i) versus time yields a straight line for the ${}^{54}\text{Fe}$ data, indicating a first-order reaction with slope kt where k is a rate constant for that given particle concentration. The ${}^{56}\text{Fe}$ data do not have a linear relationship, meaning they do not follow a first-order rate.

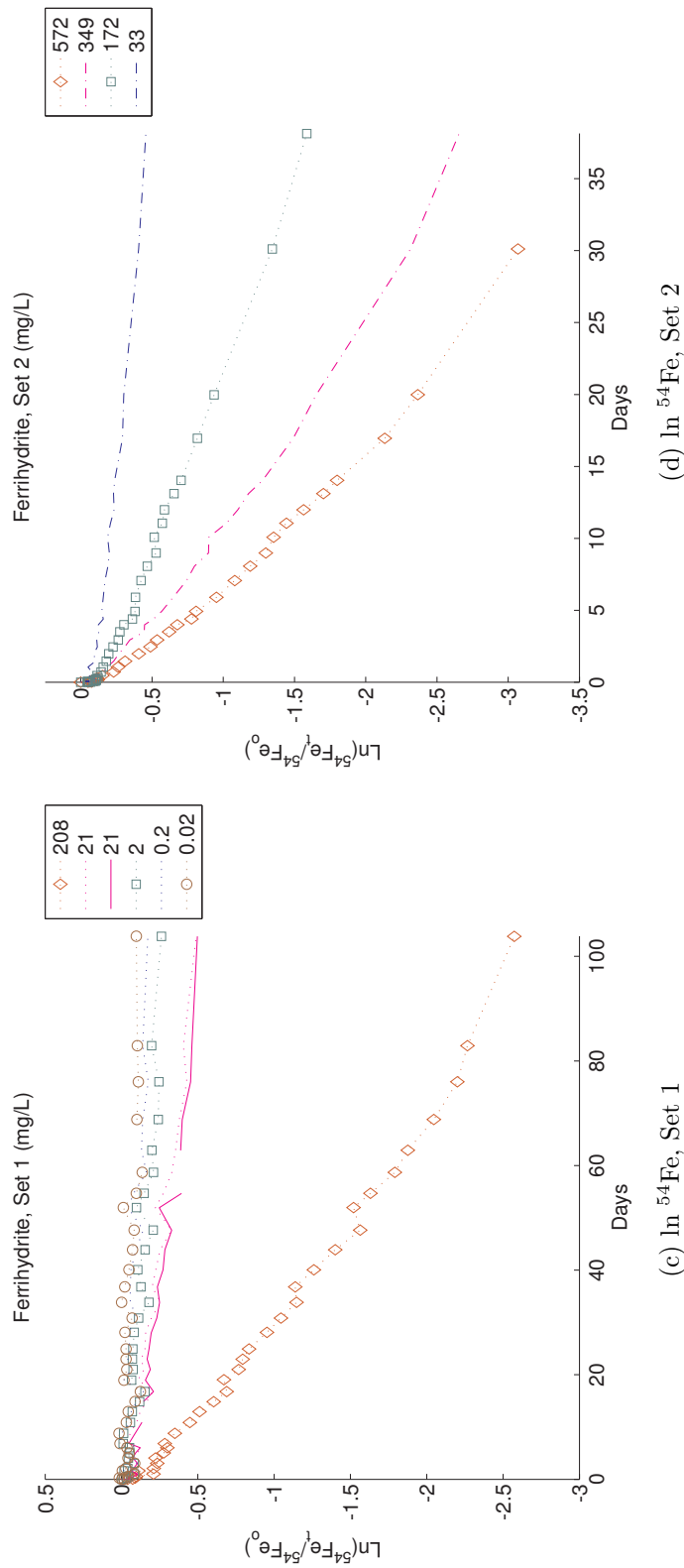


Figure 3.7. Plotting the natural log of the relative Fe (Fe_t/Fe_i) versus time yields a straight line for the ${}^{54}\text{Fe}$ data, indicating a first-order reaction with slope kt where k is a rate constant for that given particle concentration. The ${}^{56}\text{Fe}$ data do not have a linear relationship, meaning they do not follow a first-order rate.

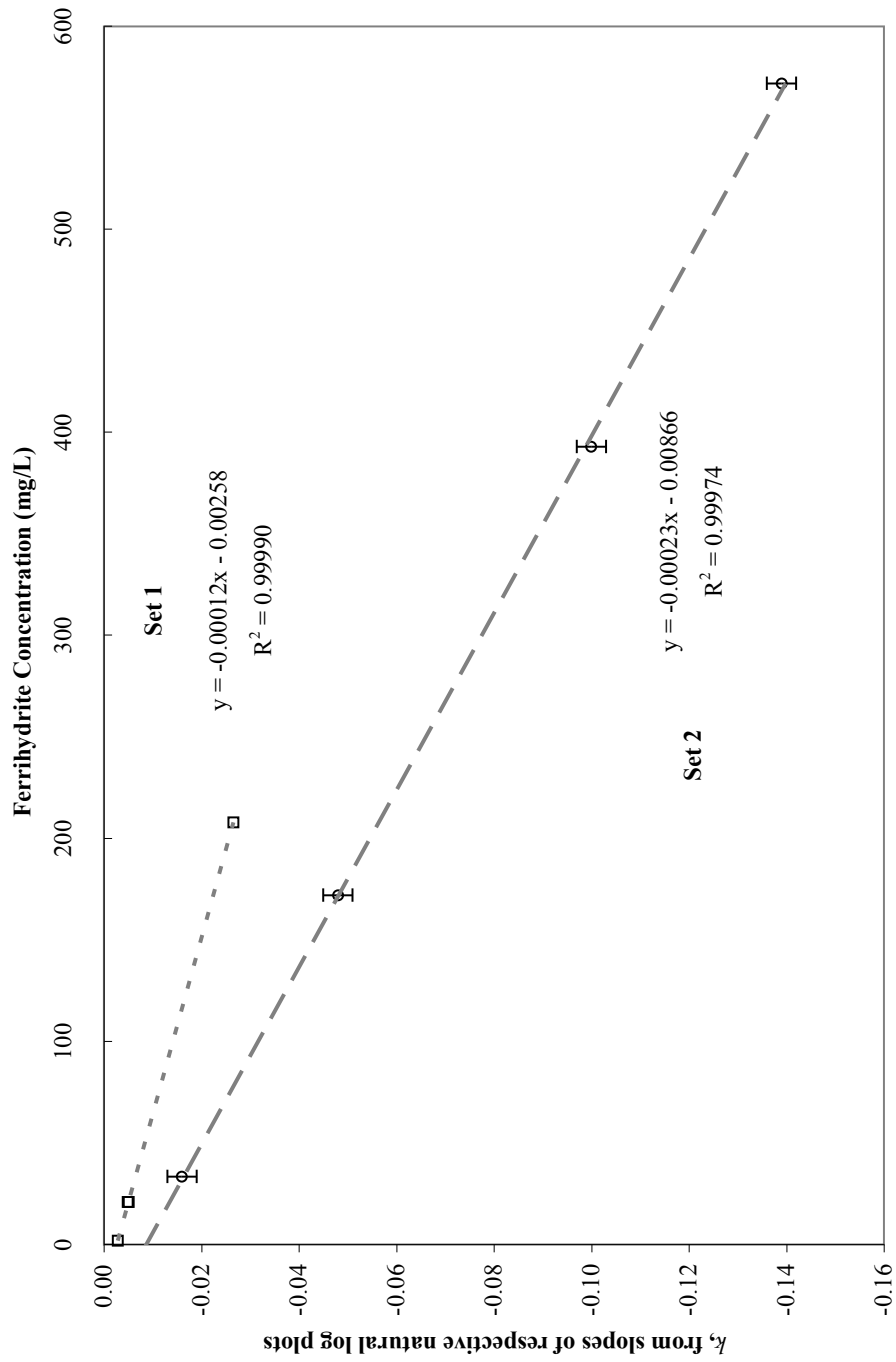


Figure 3.8. The respective slopes of the natural log plots, $k_{sorb-part}$, versus concentration of ferrihydrate (mg/L). Error bars for Set 1 are within the marker size. Set 1, squares, has a slower overall k_{sorb} compared to Set 2, circles, by a factor of 2.

more dissolution, however we observe faster adsorption and *less* dissolution.

The experimental conditions could help explain the mechanism for the change in k_{sorb} and the rate of input of $[^{56}\text{Fe}]$. Differences between the experiments include ambient temperature variations, two separate pH's (8.0 and 8.2), age of precipitate upon beginning the experiment, and Fe concentration before precipitation.

Ambient temperature varied from 19 °C to 22 °C. The widest temperature differences occurred on a diurnal time scale and probably resulted in the 10 to 15 nM dissolved [Fe] fluctuations observed on a day-to-day basis across all experiments. However, the median temperature was similar between the two experiments, so this is probably not the cause of the difference in k_{sorb} .

Changes in pH should certainly have an effect on the reaction mechanism since pH dictates the degree of protonation of surface sites. The reaction associated with FeDFB adsorption probably proceeds via metal attachment to the deprotonated hydroxide groups on the hydrolyzed surface of ferrihydrite.



Since the protonation of hydroxide groups is pH dependent, k_{sorb} will also be pH dependent. However, as pH decreases more sites will become protonated, leaving fewer reactive sites to which Fe can attach, so the k_{sorb} should slow down with lower pH. The experiment set with the lower pH 8 actually has the faster k_{sorb} $2.3 \times 10^{-4} \text{ (mg/L)}^{-1} \text{ day}^{-1}$, so, if anything, the pH difference might actually be hindering this k_{sorb} relative to the experiment set at pH 8.2 with the k_{sorb} of $1.2 \times 10^{-4} \text{ (mg/L)}^{-1} \text{ day}^{-1}$.

Aging the precipitate will lead to singly coordinated sites (FeOH) being converted to more ordered surface sites with doubly (Fe₂OH) and triply (Fe₃OH) coordinated O atoms [88]. The doubly coordinated sites are probably not proton reactive in our experimental pH range, as shown in various experiments of freshly cleaved hematite where no surface charge developed over a large pH range, therefore FeDFB will have less affinity for doubly charged groups. Triply coordinated O atoms differ in their

proton affinity because in their structuring one O atom accepts a proton (OH) and the other does not (O). This is most readily evident in the natural chemical stoichiometry of goethite, Fe(O)OH, where all the O atoms are triply coordinated. Therefore, the triply coordinated O sites are effectively half as reactive, or have half the site density as a surface with all singly coordinated sites. The surface charging of ferrihydrite has a similar proton affinity to FeOH, indicating that ferrihydrite has mostly singly coordinated reaction sites on its surfaces.

The aging differences between the two sets of experiments before the ferrihydrite precipitate was added to the AQUIL bottles were a matter of 30 to 60 minutes. While there are no estimates of how quickly singly coordinated sites convert to other types of sites for ferrihydrite, there are estimates of dissolution rates. Aging the precipitate has been shown to decrease the dissolution of ferrihydrite [89], which probably corresponds to a decrease in overall surface reactivity as well. The dissolution rate at 1 minute decreases from 2.3×10^{-4} to $6.1 \times 10^{-5} \text{ s}^{-1}$ over a period of 6 hours. If one assumes a linear relationship during that time period, then the difference in dissolution rate at 30 minutes and 60 minutes is less than 7%. If this is analogous to reaction site decrease, it probably cannot account for the factor of 2 difference we see in k_{orb} over the long course of the experiments.

The concentrations of dissolved Fe from which the ferrihydrite precipitates were formed were different between the two experimental sets. The lower range, Set 1, was precipitated from [Fe] that was a factor of 7 or 8 lower than the higher range experiment, Set 2. If the higher [Fe] precipitates had more surface sites initially, then this could explain the increase in k_{orb} for its corresponding experiment set. However, there is evidence that aging, as well as ferrihydrite preparation at relatively high initial Fe concentrations, may result in smaller surface area [98]. In fact, ferrihydrite that was produced at a higher [Fe] relative to other ferrihydrite precipitation methods resulted in a lower effective surface area [99].

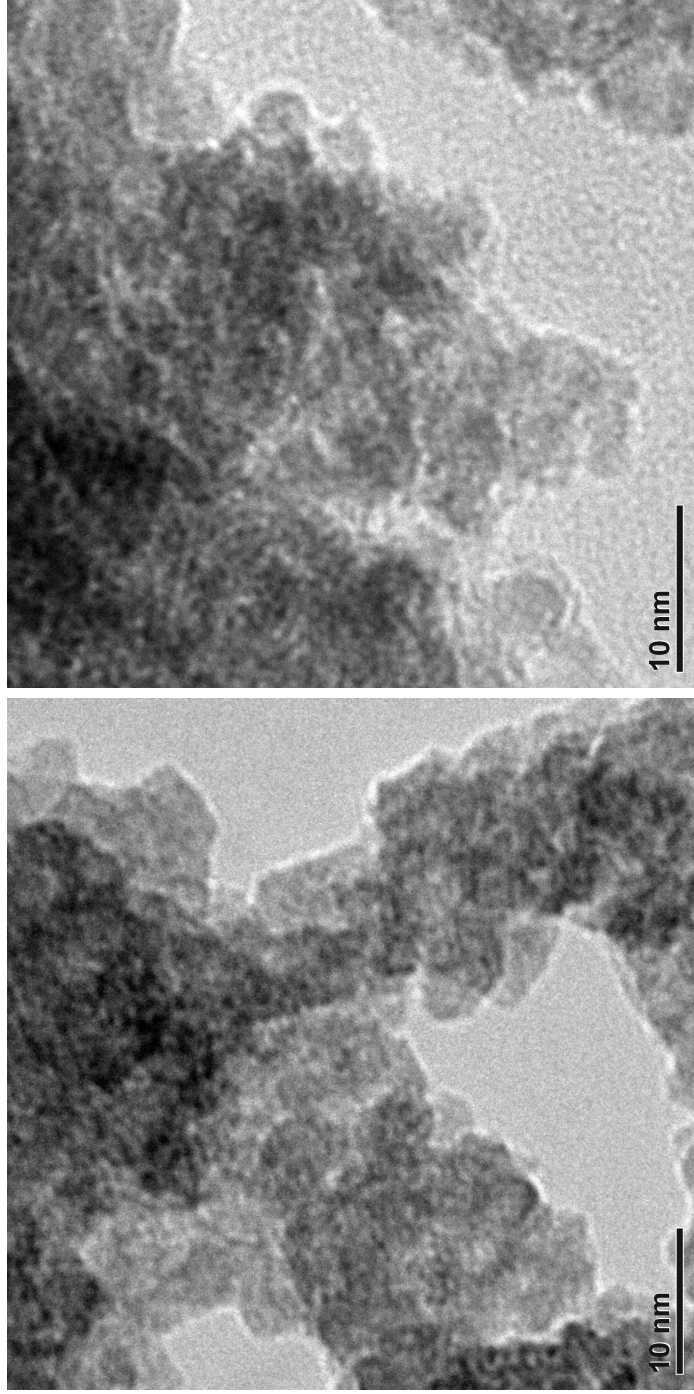
Since our precipitates were formed from dissolved [Fe] within an order of magnitude of each other, we imaged the two types of precipitate with transmission electron microscopy (TEM) to obtain an average particle diameter. TEM is especially difficult

for an amorphous, surface-charged product like ferrihydrite because the iron particles move in the electron beam due to their magnetism and have no clear diffraction pattern (since the particles are oriented in different directions). TEM studies have shown ferrihydrite to have extremely small diameters, on average 1 to 6 nm [100], which results in their huge effective surface area estimates of 450 to 650 m²/g [85].

Our fresh precipitates (10 μ L) were dispersed in isopropyl alcohol and the faintly colored solutions were air dried on holey carbon TEM grids. From our TEM images in Figure 3.9, one can see the rough outline of individual nanoparticles at the edges of the ferrihydrite aggregates. While a robust imaging program is needed to discern average particle size, there does not appear to be a qualitative particle size difference between the two precipitate batches. The images also cannot give an idea of actual particle size distribution or particle density since aggregation is so marked upon drying.

One hypothesis to explain the differences in k_{sorb} and apparent dissolution relies on particle size distribution and density. If the more concentrated Fe solution ended up with a higher particle density of similarly sized nanoparticles, these precipitates would have a higher effective surface area and an increased rate of coagulation. The higher surface area and particle density could lead to increased adsorption and removal rates via coagulation, where the nanoparticles are removed from the dissolved phase as in the colloidal pumping model [54, 55]. The precipitate formed from the lower [Fe] could have a lower overall particle density, and therefore a slower rate of removal from the dissolved phase. Similarly for the rate of [⁵⁶Fe] appearance, the higher density of precipitates have their colloidal size fraction removed more quickly from the dissolved phase, due to the higher number of particle-particle interactions. Therefore, their colloidal fractions, which have the highest site density, will not have as much opportunity to dissolve as their lower-particle-density precipitate counterparts. The desorption experiment, which is more appropriately called a dissolution experiment, has no enhanced appearance of ⁵⁴Fe, even though ⁵⁴Fe was absorbed at the beginning of the experiment, and is consistent with an irreversible colloidal pumping mechanism.

While the first-order, irreversible absorption of Fe onto ferrihydrite is concluded from the ⁵⁴Fe data, the ⁵⁶Fe data appear to be independent of dissolved [Fe]—though



(a) Lower [Fe] initial, Set 1

(b) Higher [Fe] initial, Set 2

Figure 3.9. TEM images of ferrihydrite precipitated from two different amounts of initial [Fe]. Aggregation of the precipitates was notable throughout both samples. Outlines of individual ferrihydrite particles can be seen at the edges. Qualitatively, particle diameter does not vary much between the two precipitates and averages around 3 to 5 nm.

there is a dependence on particle concentration as the dissolution increases with increasing ferrihydrite concentration, consistent with the Rose and Waite study [89]. The mechanism of the ^{56}Fe dissolution might be adjunctive, where the DFB attaches to the precipitate surface and detaches with an Fe atom, or disjunctive, where the Fe dissolves and then DFB binds to it before re-precipitation or adsorption. The dissolution capacity of dust in seawater has been shown to be dependent on the surrounding ligand concentration [97]. Rose and Waite showed that altering the DFB concentration by an order of magnitude did not cause any change in the dissolution rate from a fresh iron oxide precipitate [89], which indicates that dissolution is probably a disjunctive mechanism. In our desorption study, the precipitates were equilibrated with a small volume of highly concentrated tracer and then were filtered, suggesting that any DFB on the precipitate had adsorbed onto the particle surface before it was placed in AQUIL. While this extremely high particle concentration during the adsorption period might be an inaccurate representation of a natural system, the DFB does have the ability to seemingly attach to ferrihydrite and then desorb and take Fe with it, or desorb by itself and then attach to Fe within the dissolved phase. Repeating the desorption experiment with a higher ligand concentration could further elucidate the mechanism.

3.5 Modeling

Adsorption, desorption, dissolution, and precipitation are all mechanisms affecting the dissolved [Fe]. Assuming other mechanisms have a minor effect, the rate of change of ^{54}Fe and ^{56}Fe can be described with the following two sets of coupled differential equations which account for exchange of ^{54}Fe and ^{56}Fe between the dissolved and particulate phase. Using forward modeling and parameter estimation in MATLAB, we find the physical rate constants that provide the best fit between this model and our measured data and take into account oceanic salinity, pH, and organic speciation

of Fe.

$$\begin{aligned} \frac{d[{}^{54}\text{Fe}]_D}{dt} &= -k_{sorb}[\text{part}][{}^{54}\text{Fe}]_D + k_{desorb}([{}^{54}\text{Fe}]_D|_{t=0} - [{}^{54}\text{Fe}]_D) \\ &\quad + k_{diss}[{}^{54}\text{Fe}]_P - k_{precip}(f_{54} \cdot [\text{Fe}_{ID}])[{}^{54}\text{Fe}]_P \end{aligned} \quad (3.3)$$

$$\begin{aligned} \frac{d[{}^{54}\text{Fe}]_P}{dt} &= +k_{sorb}[\text{part}][{}^{54}\text{Fe}]_D - k_{desorb}([{}^{54}\text{Fe}]_D|_{t=0} - [{}^{54}\text{Fe}]_D) \\ &\quad - k_{diss}[{}^{54}\text{Fe}]_P + k_{precip}(f_{54} \cdot [\text{Fe}_{ID}])[{}^{54}\text{Fe}]_P \end{aligned} \quad (3.4)$$

$$\begin{aligned} \frac{d[{}^{56}\text{Fe}]_D}{dt} &= -k_{sorb}[\text{part}][{}^{56}\text{Fe}]_D + k_{desorb}([{}^{56}\text{Fe}]_D|_{t=0} - [{}^{56}\text{Fe}]_D) \\ &\quad + k_{diss}[{}^{56}\text{Fe}]_P - k_{precip}(f_{56} \cdot [\text{Fe}_{ID}])[{}^{56}\text{Fe}]_P \end{aligned} \quad (3.5)$$

$$\begin{aligned} \frac{d[{}^{56}\text{Fe}]_P}{dt} &= +k_{sorb}[\text{part}][{}^{56}\text{Fe}]_D - k_{desorb}([{}^{56}\text{Fe}]_D|_{t=0} - [{}^{56}\text{Fe}]_D) \\ &\quad - k_{diss}[{}^{56}\text{Fe}]_P + k_{precip}(f_{56} \cdot [\text{Fe}_{ID}])[{}^{56}\text{Fe}]_P \end{aligned} \quad (3.6)$$

This model consists of four differential equations that represent the change in concentrations of four variables, ${}^{54}\text{Fe}$ dissolved and particulate, $[{}^{54}\text{Fe}]_D$ and $[{}^{54}\text{Fe}]_P$, and ${}^{56}\text{Fe}$ dissolved and particulate, $[{}^{56}\text{Fe}]_D$ and $[{}^{56}\text{Fe}]_P$, respectively. Each addition term to the dissolved phase is a corresponding loss term for its respective particle phase, and vice versa. The parameters we solve for are rate constants for adsorption (k_{sorb}), desorption (k_{desorb}), dissolution (k_{diss}), and precipitation (k_{precip}). Adsorption depends on particle concentration ($[\text{part}]$), $[{}^{54}\text{Fe}]_D$, and k_{sorb} , which has already been estimated by a first-order model to be $1.2 - 2.3 \times 10^{-4} \text{ (mg/L)}^{-1} \text{ day}^{-1}$, as described in Section 3.4. Desorption depends on k_{desorb} and the amount of Fe adsorbed onto the surface, which begins at zero because no FeDFB has adsorbed onto the surface at $t = 0$, and then it grows as ${}^{54}\text{Fe}$ is removed from the dissolved phase and deposited on the surface.

Dissolution and precipitation terms are based on the rates determined by Rose and Waite [89]. Dissolution depends on k_{diss} and the respective concentration of Fe in

the particulate phase. Precipitation depends on k_{precip} , a second-order rate constant, and the concentration of inorganic Fe dissolved, Fe_{ID} , and Fe particulate. The more concentrated these species are, the more collisions there will be to speed up precipitation [89]. $[Fe_{ID}]$ is the total amount of inorganic dissolved Fe, mostly hydrolyzed Fe at pH 8, and can be visualized from a log C versus pH diagram for amorphous $Fe(OH)_3(s)$ in equilibrium with FeDFB (Figure 3.10). Seawater pairing constants were used for major ions, which were not significant contributors to dissolved inorganic Fe [93]. Fe hydrolysis constants were calculated using ionic strength, $I = 0.5$, and the Davies equation [93]. By definition of the solid being present, the dissolved Fe^{3+} is set by K_{sp} and pH, and calculation of $[Fe_{ID}]$ is straightforward. The total amount of Fe_{ID} at pH 8.1 is a sum of the Fe species, mainly $Fe(OH)_2^+$ and $Fe(OH)_4^-$, and is calculated to be $\log([Fe_{ID}]) = -9.95$. The relative fractions of ^{54}Fe and ^{56}Fe are based on normal isotopic abundance with values of $f_{54} = 0.058$ and $f_{56} = 0.917$, respectively.

Initial conditions are defined for each variable in the model, and then the model is allowed to run for the duration of the experiment length without further inputs. We set up initial conditions based on the measured dissolved ^{54}Fe and ^{56}Fe before particle addition, and we used particle concentration to calculate the initial values of particulate ^{54}Fe and ^{56}Fe .

The model also requires an initial parameter guess and allows fixing or varying of each parameter. The respective k_{sorb} values were used for each model run of the individual experiments. k_{diss} and k_{precip} values were based on the study of dissolution and precipitation of ferrihydrite in the presence of DFB [89]. k_{diss} decreased by 2 orders of magnitude over the 1 week experiment from $2.3 \times 10^{-4} \text{ s}^{-1}$ to $4.8 \times 10^{-6} \text{ s}^{-1}$. We based our k_{precip} term on the second-order rate from this study, which had a value of $(4.1 \pm 1.1) \times 10^7 \text{ M}^{-1} \text{ s}^{-1}$. The initial estimate for k_{desorb} was based on the guess that $[^{56}Fe]$ did not desorb from ferrihydrite as quickly as it absorbed and was therefore slightly lower in magnitude than k_{sorb} . The model had a fixed k_{sorb} and the other 3 parameters were permitted to vary for the parameter estimation. The parameters were all constrained to be positive values.

The model is used to solve the set of differential equations and compare the resulting $[^{54}\text{Fe}]_{model}$ and $[^{56}\text{Fe}]_{model}$ to the experimental data, while adjusting the parameters in an iterative fashion to minimize the difference between the model concentration data, $[\text{Fe}]_{model}$, and the experimental concentration data, $[\text{Fe}]_{data}$. The numerical calculations were performed using the MATLAB grey-box modeling toolbox. “ode45” was used as the ordinary differential equation solver. The parameter estimation was performed using the PEM function. The parameter estimation minimums were robust to several orders of magnitude change in the initial parameter guesses, meaning no other minimums were observed.

The model output, $[\text{Fe}]_{model}$, generated from the best parameter minimization, is plotted together with the experimental $[\text{Fe}]$ to visually compare the model fit to the experimental data (Figure 3.11 for ferrihydrite Set 1 and Figure 3.12 for ferrihydrite Set 2). The comparison is quantified by computing a fit % based on the difference between the model and the measured $[\text{Fe}]$, defined as

$$\text{fit} = 100 * \left[1 - \frac{\text{norm}([\text{Fe}]_{model} - [\text{Fe}]_{data})}{\text{norm}([\text{Fe}]_{data} - \text{mean}[\text{Fe}]_{data})} \right], \quad (3.7)$$

where the function “norm” computes the maximum of the sums of the absolute differences between model and experiment data. Essentially, this fit takes the magnitude of the difference between the model and measured $[\text{Fe}]$ and normalizes it to the noise in the data around that point, e.g., the difference between the $[\text{Fe}]$ at that point in time to the mean of the points 1 time-step away. As the difference between $[\text{Fe}]_{model}$ and $[\text{Fe}]_{data}$ approaches zero, then the fit would approach 100%.

For our model-to-experimental-data comparison, the model fits are generally over 70%, with lower fits corresponding to more noisy data. The worst fit is for the lowest particle concentration, 2 mg/L. For this particle concentration, the model seems to have overestimated the ^{54}Fe absorption and underestimated the ^{56}Fe dissolution. This could be due to an artifact of the control corrections for wall loss, since the 2 mg/L data set has much lower relative change in $[\text{Fe}]$ compared to the control.

A test of the sensitivity of the parameters and a visualization of the cost function

FeDFB and Fe Inorganic Dissolved Species in Presence of Ferrihydrite

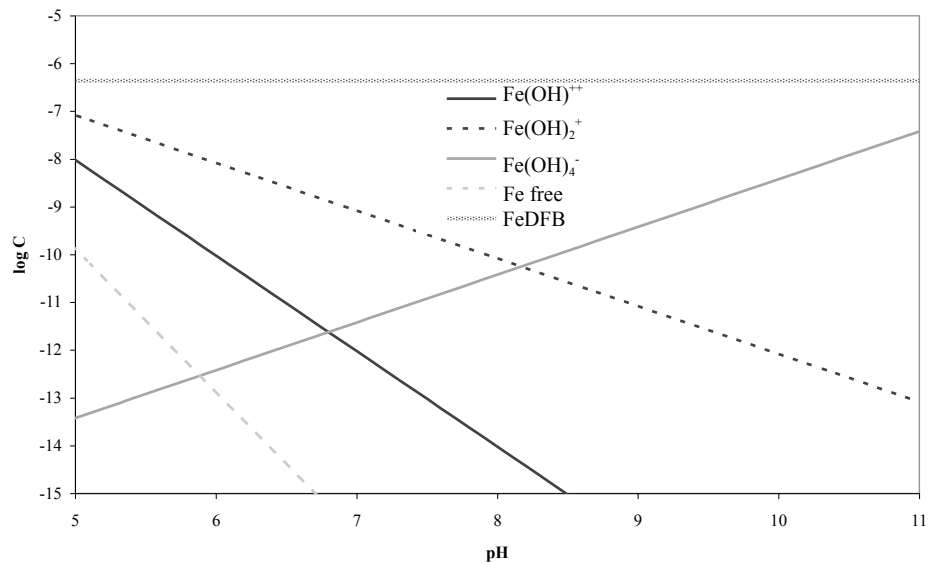


Figure 3.10. $\log C$ v pH diagram of Fe(III) in the presence of ferrihydrite, $\text{Fe}(\text{OH})_3$. Complexation constants have been corrected for appropriate ionic strength. FeDFB remains constant across a range of pH values due to the strong binding constant of DFB to Fe^{3+} . Fe^{3+} is set by presence of the solid since $[\text{Fe}]_{\text{solid}} > [\text{DFB}]_{\text{total}}$. At pH 8, the inorganic Fe species are dominated by $\text{Fe}(\text{OH})_2^+$ and to a lesser extent by $\text{Fe}(\text{OH})_4^-$.

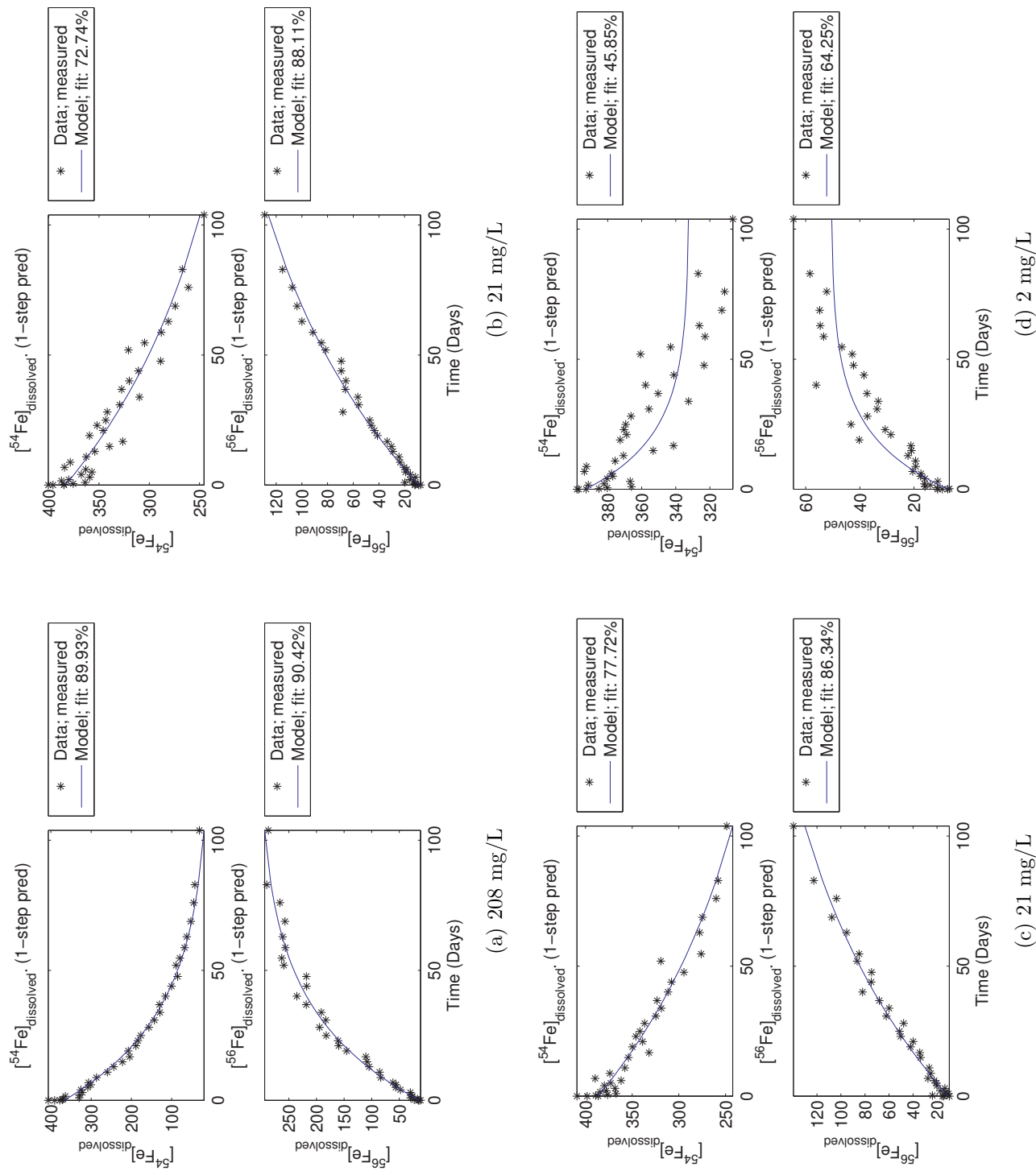


Figure 3.1.1. Fits of $[Fe]_{model}$ and experimental $[Fe]_{data}$ for Set 1 ferrihydrite experiments.

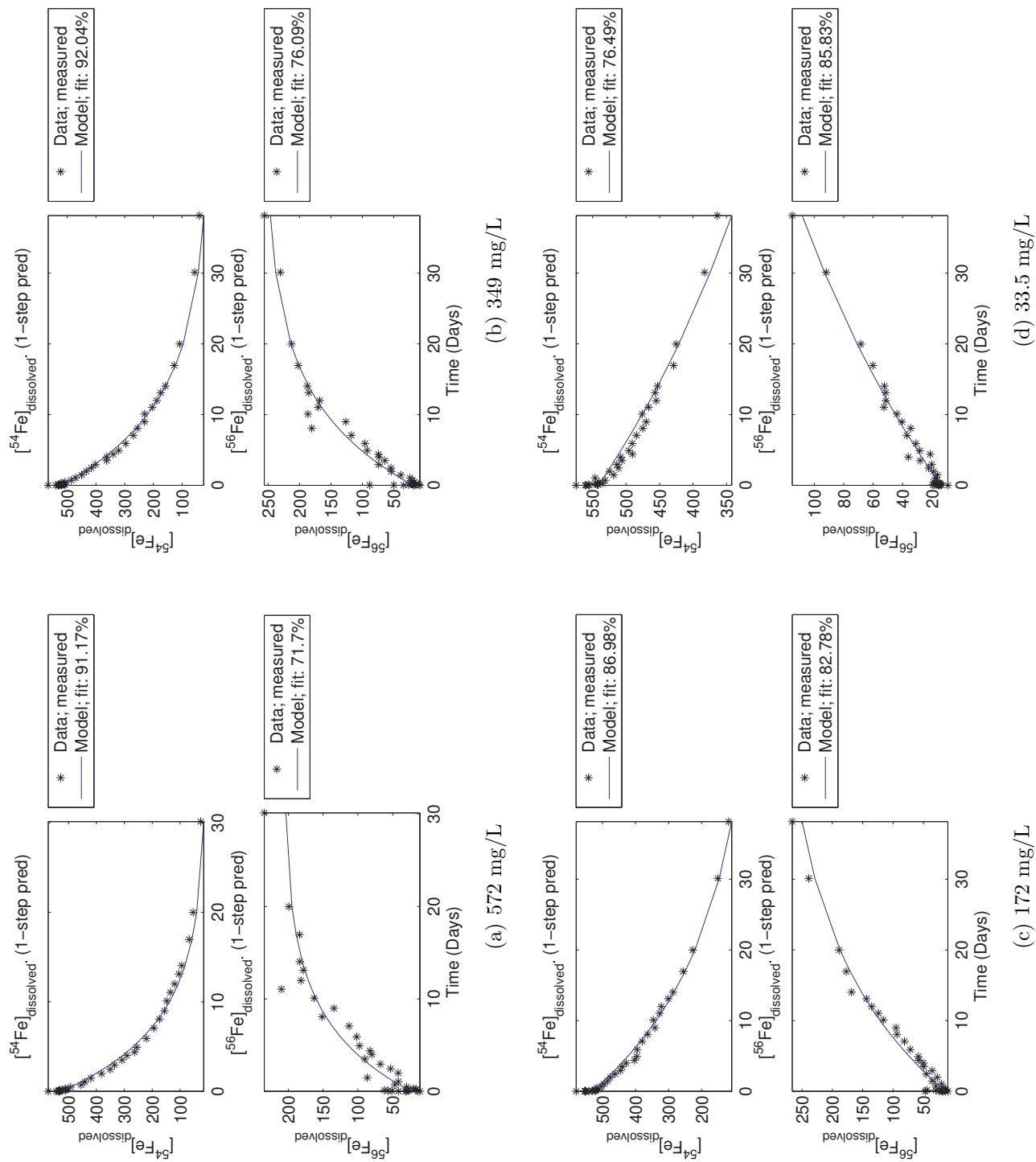
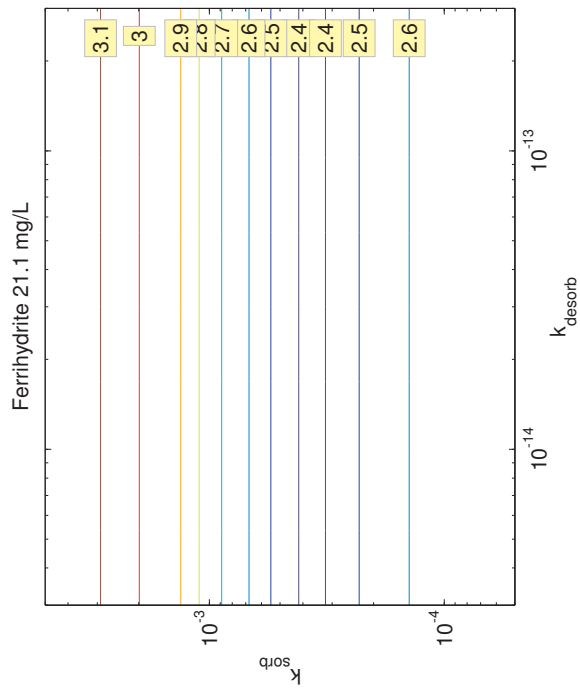
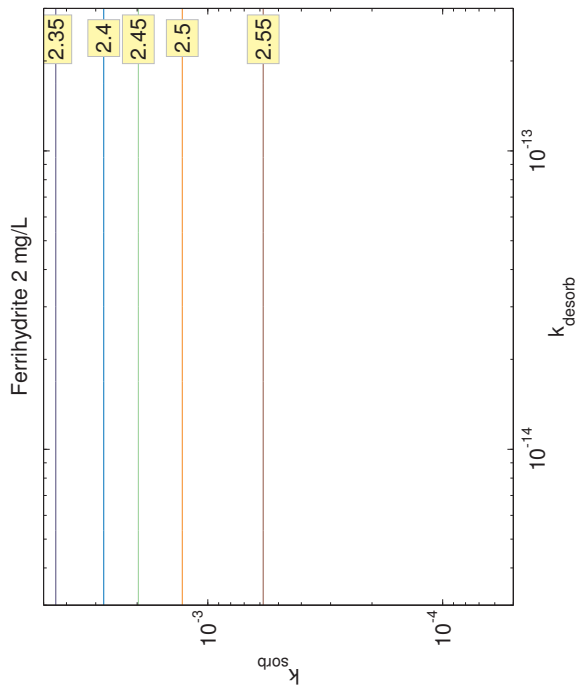


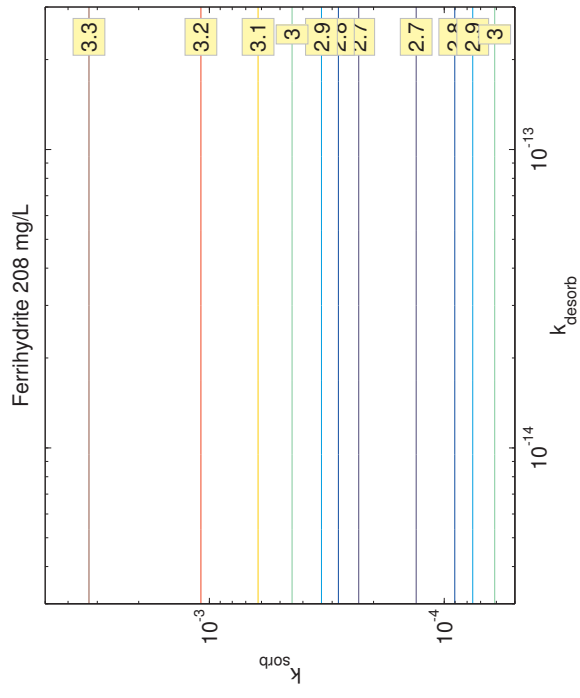
Figure 3.12. Fits of $[\text{Fe}]_{\text{model}}$ and experimental $[\text{Fe}]_{\text{data}}$ for Set 2 ferrihydrite experiments.



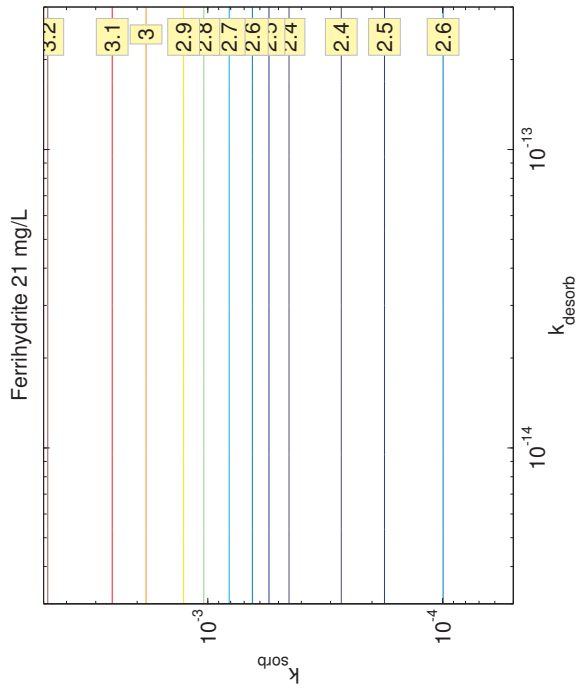
(b) 21 mg/L



(d) 2 mg/L



(a) 208 mg/L



(c) 21 mg/L

Figure 3.13. Sensitivity tests for k_{sorb} vs. k_{desorb} for Set 1 experiments. Contours are logarithms of the sum of the deviates. Our model is more dependent on k_{sorb} than k_{desorb} .

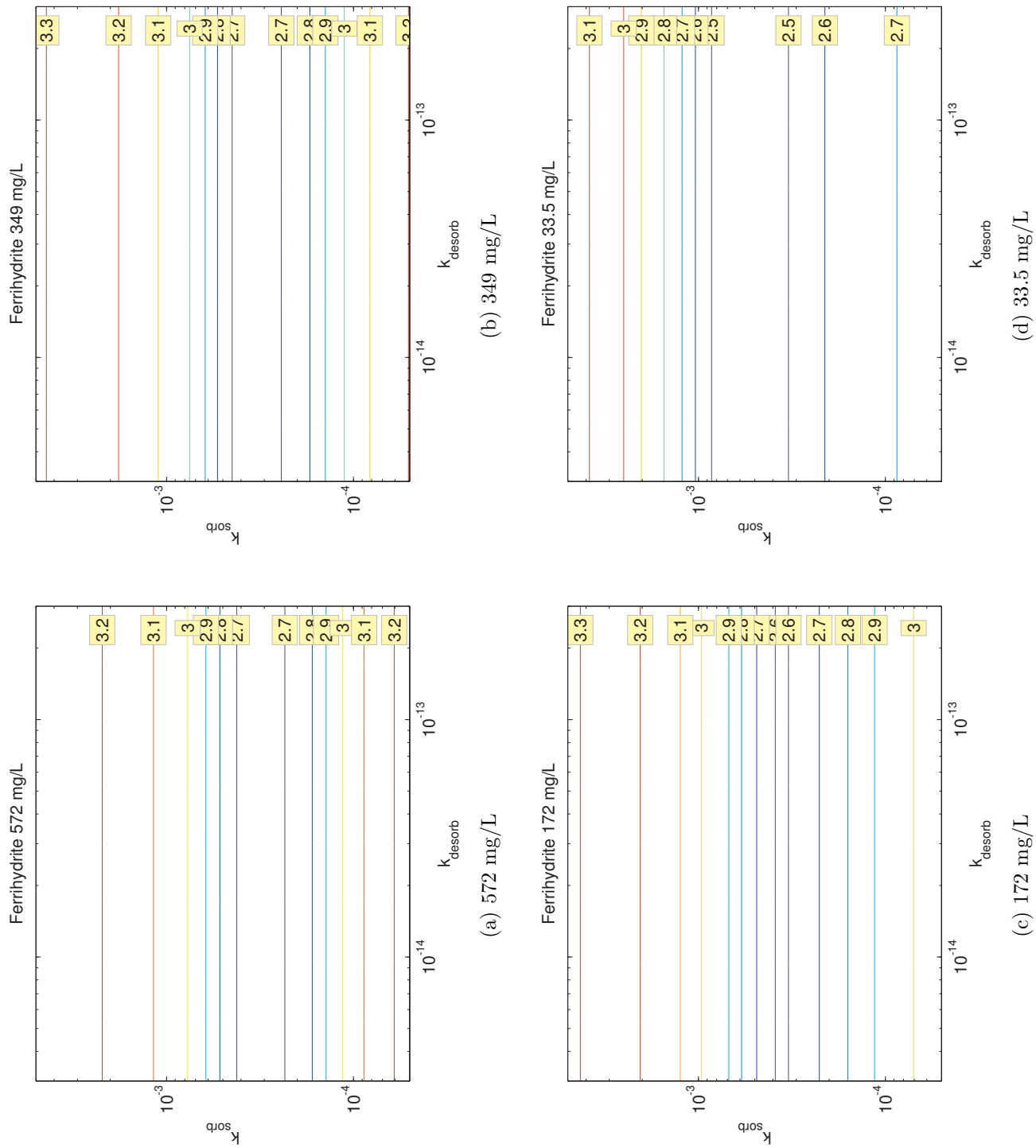


Figure 3.14. Sensitivity tests for k_{sorb} vs. k_{desorb} for Set 2 experiments. Contours are logarithms of the sum of the deviates. Our model is more dependent on k_{sorb} than k_{desorb} .

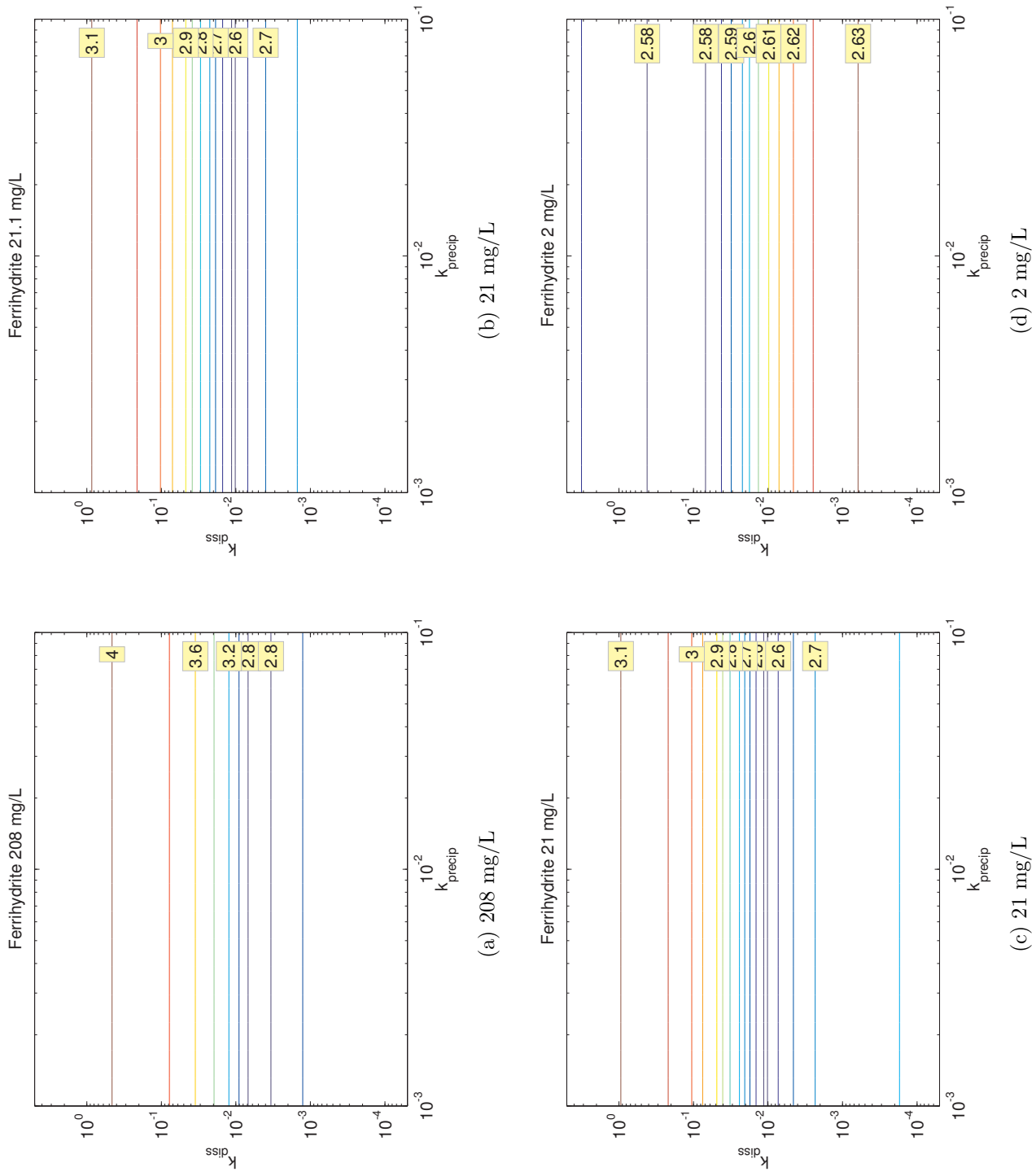


Figure 3.15. Sensitivity tests for k_{diss} vs. k_{precip} for Set 1 experiments. Contours are logarithms of the sum of the deviates. Our model is more dependent on k_{diss} than k_{precip} .

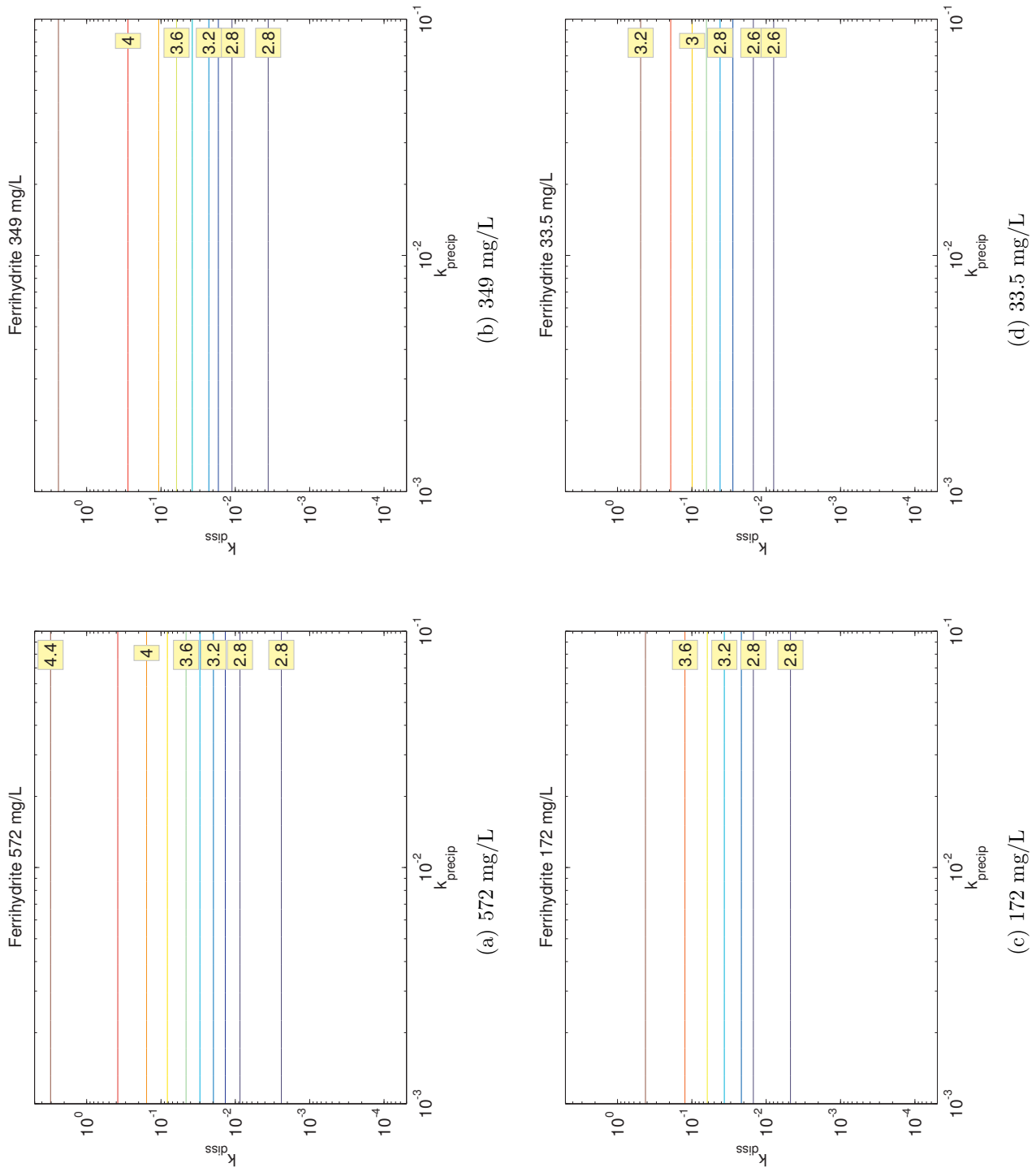


Figure 3.16. Sensitivity tests for k_{diss} vs. k_{precip} for Set 2 experiments. Contours are logarithms of the sum of the deviates. Our model is more dependent on k_{diss} than k_{precip} .

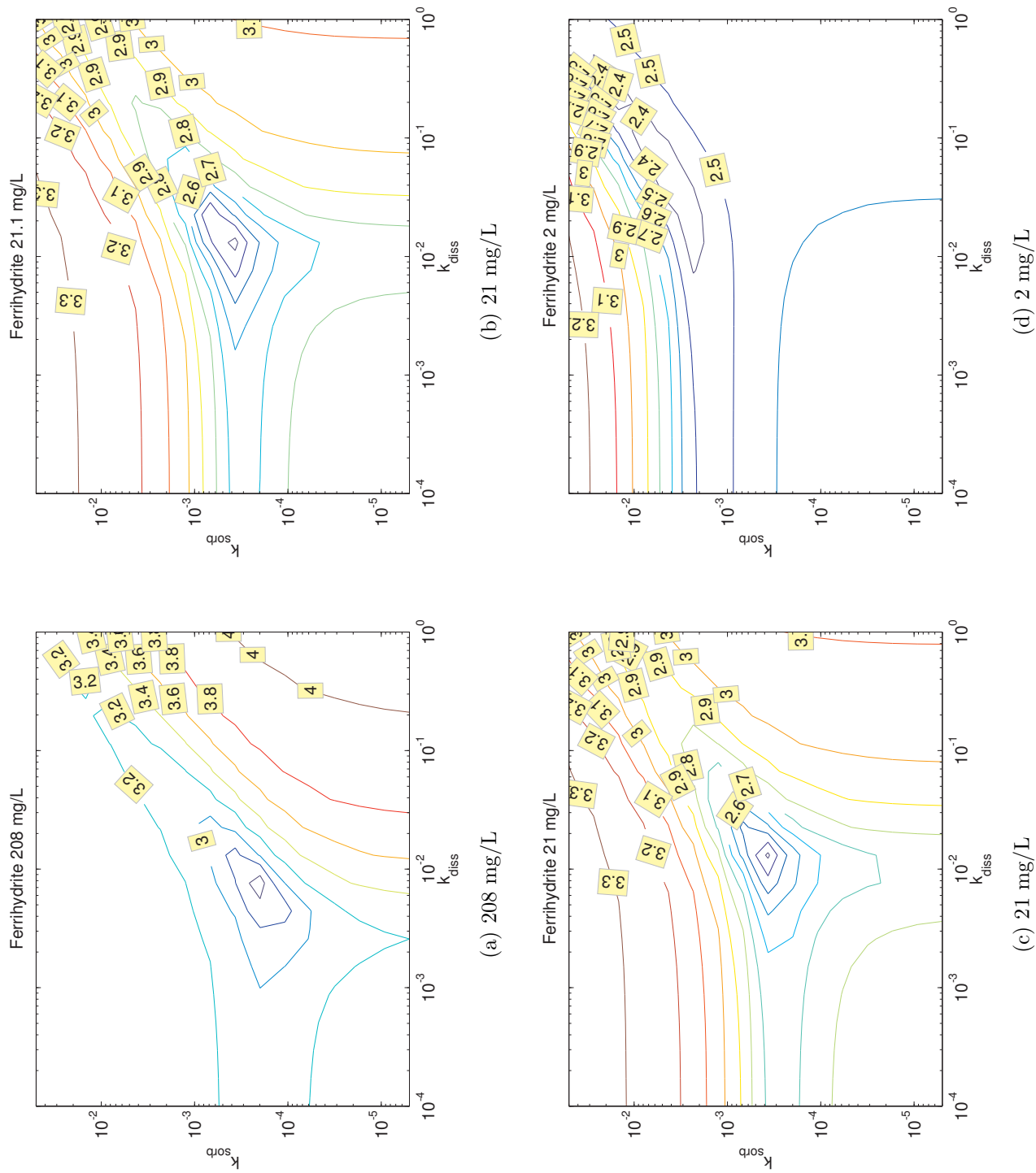


Figure 3.17. Sensitivity tests for k_{sorb} vs. k_{diss} for Set 1 experiments. Contours are logarithms of the sum of the deviates. A minimum is found around $4-6 \times 10^{-4}$ L/mg/day for k_{sorb} and 0.02 /day for k_{diss} , with the exception of 2 mg/L.

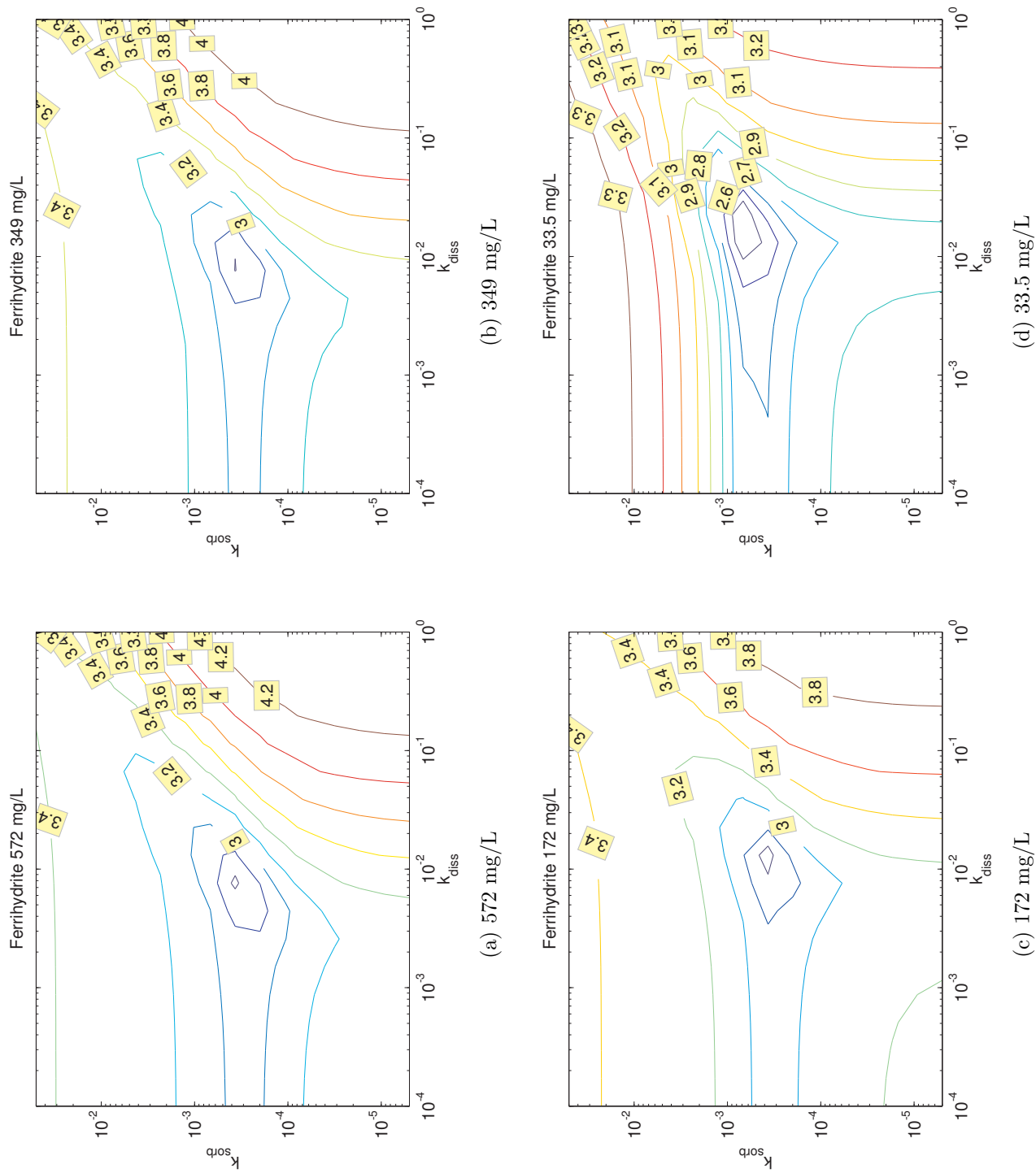


Figure 3.18. Sensitivity tests for k_{sorb} vs. k_{diss} for Set 2 of experiments. Contours are logarithms of the sum of the deviates. A minimum is found around $4-6 \times 10^{-4}$ L/mg/day for k_{sorb} and 0.02 /day for k_{diss} .

minimization is done by varying all of the k parameter estimates over several orders of magnitude, solving with the model numerically, and then plotting the sum of the squares of the differences between model and measured [Fe] for forward and reverse rate constants. These sensitivity tests were first done for pairs k_{sorb} versus k_{desorb} and k_{diss} versus k_{precip} . Each of these plots for the 8 experiments (4 experiments from Set 1 and all 4 experiments from Set 2) are shown in Figures 3.13, 3.14 and 3.15, 3.16. The contours are the logarithm of the sum of the squares of the deviations, so their magnitudes are important for showing that the model is more closely matching the data for lower overall numbers. From the rows of horizontal lines in both types of plots, clearly there is little dependence on k_{desorb} and k_{precip} (both on x-axes), and strong of dependence on k_{sorb} and k_{diss} . From these same model outputs, k_{sorb} versus k_{diss} are plotted together, from which actual minimums are observed within the contours (Figure 3.17, 3.18).

Minimums are found between values $4 - 6 \times 10^{-4}$ /(mg/L)/day for k_{sorb} and between $0.01 - 0.02$ /day for k_{diss} . The optimal minimum values of appear to be robust across all experiments of varying particle concentrations, except at the lowest particle concentration of 2 mg/L . This range of k_{diss} is slower than the 1 week k_{diss} rate, measured by Rose and Waite [89], by an order of magnitude. This difference could be that after one or two weeks, the dissolution of ferrihydrite becomes more or less constant, as suggested by the the slight stabilization of k_{diss} towards the end of their experiments. There could also be some disparity between our operationally defined dissolved phase and their optical method of determining FeDFB concentration. The model values of k_{sorb} are faster than our first-order rates, $1.2 - 2.3 \times 10^{-4}$ (mg/L) $^{-1}$ day $^{-1}$, by a factor of 2 to 4, meaning that the model predicts Fe to be lost faster from the dissolved phase than the simple first-order particle adsorption model does. This enhanced loss of Fe could be due to the colloidal pumping that is removing Fe by coagulating colloids together into the particulate phase, in addition to Fe adsorbing onto particulate matter ($> 0.2 \mu\text{m}$), or from not accounting for wall loss as a term in the model.

3.6 Conclusions

As determined from multiple laboratory experiments with FeDFB in the presence of ferrihydrite, there are large effects on the dissolved [Fe] that stem namely from adsorption of FeDFB onto the particles and dissolution of ferrihydrite itself. Even though DFB is among one of the strongest naturally occurring siderophores, it is not a match for fresh, labile iron oxides with highly accessible surface area and reactive sites. FeDFB total decreases over time, though a remarkable amount of ligand-mediated dissolution also takes place. The estimated parameter ranges for adsorption and dissolution are $(4 \pm 2) \times 10^{-4} \text{ (mg/L)}^{-1} \text{ day}^{-1}$ and $0.015 \pm 0.01 \text{ day}^{-1}$. This exchange capacity is important for fresh precipitates formed in the ocean. Even though Fe will precipitate when the dissolved phase becomes over-saturated, there is still an exchange that transfers Fe from both phases to continue to alter the dissolve phase [Fe].

Chapter 4

Equilibration of FeDFB with Clay, Forams, Opal, Goethite, and Ferrihydrite

4.1 Introduction

In addition to the fresh, labile iron oxide precipitate ferrihydrite that was discussed in the previous chapter, our experiments focus on four naturally occurring pure mineral phases. If a preferential uptake exists among varying particle types, then particle composition should factor into Fe dissolved-particulate phase modeling in addition to particle concentration.

While many studies have been conducted to test particle preference for particle flux and circulation tracers, there have been few studies investigating the preference of ligand-bound, dissolved Fe among varying particle types. A way of comparing the amount of metal, M , in the particulate versus dissolved phase is through a universal partitioning coefficient, or distribution coefficient,

$$K_D = \frac{(M)_{\text{particulate}}}{(M)_{\text{dissolved}}}. \quad (4.1)$$

One study tested the absorption of an added Fe radiotracer, as species Fe^{3+} , in natural seawater in the presence of 3 different mineral phases [68]. The distribution coefficients for $^{59}\text{Fe}^{3+}$ after 3 weeks of equilibration with goethite and manganese oxide were an order of magnitude larger than with montmorillonite. They hypothesized that colloidal aggregation was responsible for the removal of the Fe.

Another study focusing on radiotracer equilibration with different sediment types

noted a large increase in ^{59}Fe K_D for sediments that contained more Mn than the other two sediment types [69], suggesting that the composition of sediments and suspended particulate matter plays an important role in removal of Fe. A more recent paper by Santschi and his co-workers determined that the coagulation of the organic colloid fraction of ^{59}Fe into the particulate phase was the rate-limiting removal process in estuary and river mixing with estuary waters, occurring on the order of 10 days, whereas absorption of $^{59}\text{Fe}^{3+}$ onto the colloid size fraction was relatively fast, \sim hours [60].

Aeolian input is arguably the largest source of Fe to the open ocean [9, 101]. A set of radiotracer experiments focused on the absorption of ^{59}Fe onto aerosol particles of three types: remotely collect marine aerosols, illite (a type of non expanding clay) and Chinese loess (mainly silt with varying amounts of sand or clay) [102]. They argue that pure inorganic phases are not representative of the aeolian suspended particulate matter, which contain large fractions of weathered minerals and organic material, and its absorptive capabilities and the amount of soluble Fe. An in-depth study of the affect of aerosol aging and weathering on the solubility of Fe lead to the conclusion that chemical speciation greatly affects Fe solubility once the aerosols reach the ocean [103].

The results of our own FeDFB absorption experiments are discussed in this chapter, along with the implications of mineral composition affecting Fe residence time in the ocean. While mineral standards are not the most accurate representation of naturally occurring, weathered particulate matter, they will give an initial indication of organically complexed Fe preferences among bulk phase minerals (montmorillonite, goethite, ferrihydrite) and biologically produced particles (opal, forams).

4.2 Brief Experimental Setup

Further details are described in Chapter 2. Our tracer, ^{54}Fe , was equilibrated with DFB (1DFB:1Fe) before addition to AQUIL. After 2 days of equilibration of $^{54}\text{FeDFB}$ with the bottle walls, varying amounts of goethite, montmorillonite, opal, forams, and

ferrihydrite (as discussed in Chapter 3) were added to individual bottles. A control bottle with $^{54}\text{FeDFB}$ and no particles was prepared in parallel. Another set of experiments was done for these 4 particle types at a higher particle concentration, approximately 6000 mg/L. The desorption experiments were done together for all particle types (including ferrihydrite) at approximately 1000 mg/L for goethite, forams, opal, and montmorillonite. Sub-samples were taken at discrete time intervals and filtered (0.2 μm polypropylene), prior to spiking, dilution, and analysis on an Agilent 7500 ICP-MS.

4.3 Results

Plots of ^{54}Fe and ^{56}Fe in the presence of particles have been adjusted so that their scale bars match those in Chapter 3 for ease of comparison. For ^{54}Fe , the y-axis has been set to 450 nM. ^{56}Fe plots have a maximum of 350 nM, the upper limit of the observed ^{56}Fe across all particle concentrations and types. Plots of $[\text{Fe}]_{\text{total}}$ include both ^{54}Fe and ^{56}Fe , so the net $[\text{Fe}]$ in the presence of ferrihydrite can be visualized.

Measurements of ^{54}Fe and ^{56}Fe in the dissolved phase have been corrected for the loss of ^{54}Fe and ^{56}Fe in the control. The control fit (Chapter 3, Figure 3.2) yields a linear slope of approximately 0.4 nM Fe lost per day. A linear relationship indicates a zeroth-order reaction, independent of $[\text{Fe}]$ or site concentration on the bottle walls. The addition of Fe back into the experiments to account for wall loss was split proportionally according to the amount of ^{54}Fe and ^{56}Fe present in the dissolved phase on any given day, assuming any fractionation between the isotopes is negligible.

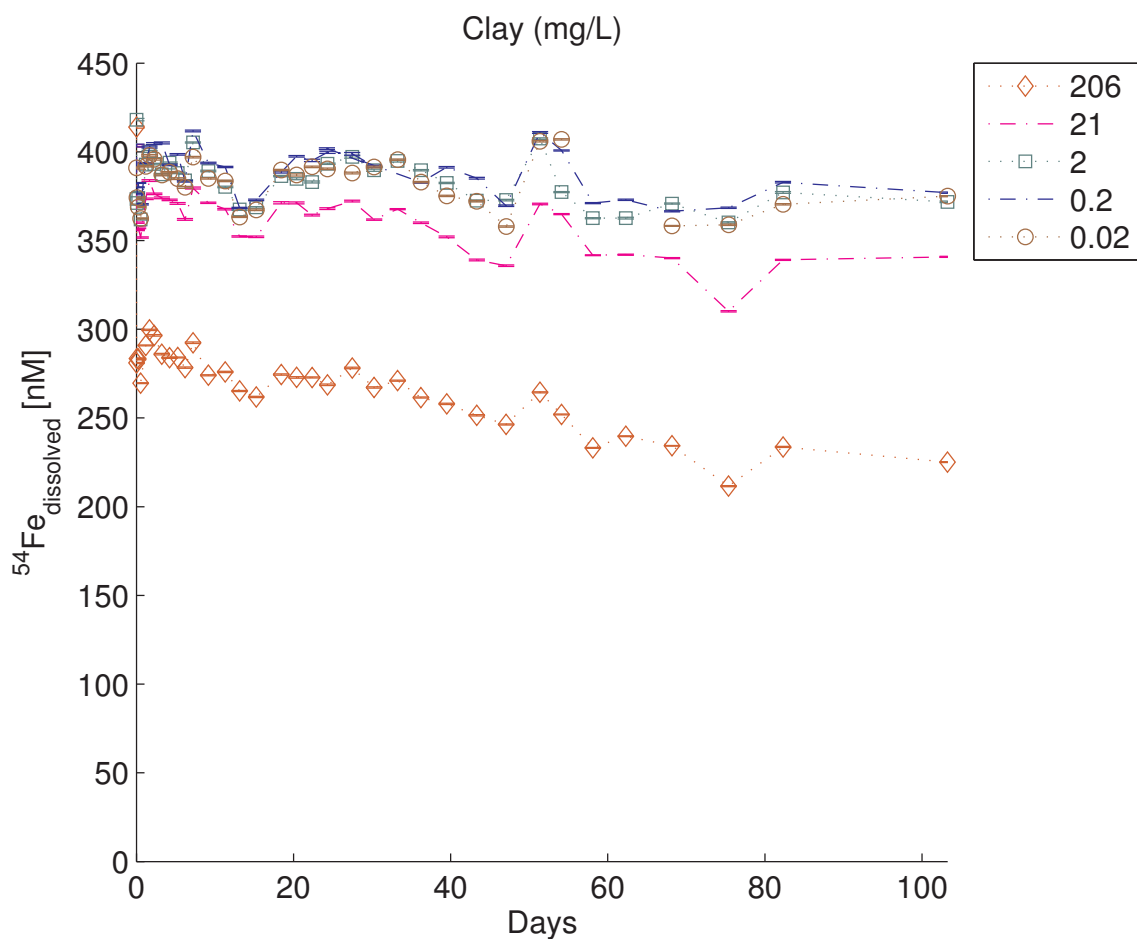
Plots of ^{54}Fe versus time and ^{56}Fe versus time are displayed in Figures 4.1–4.4 for the first set of experiments at lower particle concentrations. For goethite, forams, and opal, there is very little ^{54}Fe removal from the dissolved phase, suggesting that they have few reactive sites for absorbing organically complexed Fe. Montmorillonite, on the other hand, shows a sharp drop in concentration by the first sub-sample at ~ 10 minutes after particle addition, then a slower decline in ^{54}Fe continues through

day 100. The magnitude of ^{54}Fe removal increases with increasing montmorillonite concentration. The increases in ^{56}Fe for opal and forams scale between particle concentrations, whereas goethite has similar dissolution magnitudes among all particle concentrations. Montmorillonite has the highest ^{56}Fe increase among these 4 particle types after 100 days.

The plots of ^{54}Fe and ^{56}Fe versus time for the second set of experiments with these particles at a single, higher particle concentration (6000 mg/L) are shown in Figure 4.5. This particle concentration is larger than the particulate loading typically found in estuaries, which is approximately 500 mg/L. At this high particulate loading, the ^{54}Fe concentration in the presence of forams, opal, or goethite decreased by 20% at most. However, the ^{54}Fe concentration in the presence of montmorillonite decreased by 87%, again indicating the affinity of ^{54}Fe for this particular mineral phase.

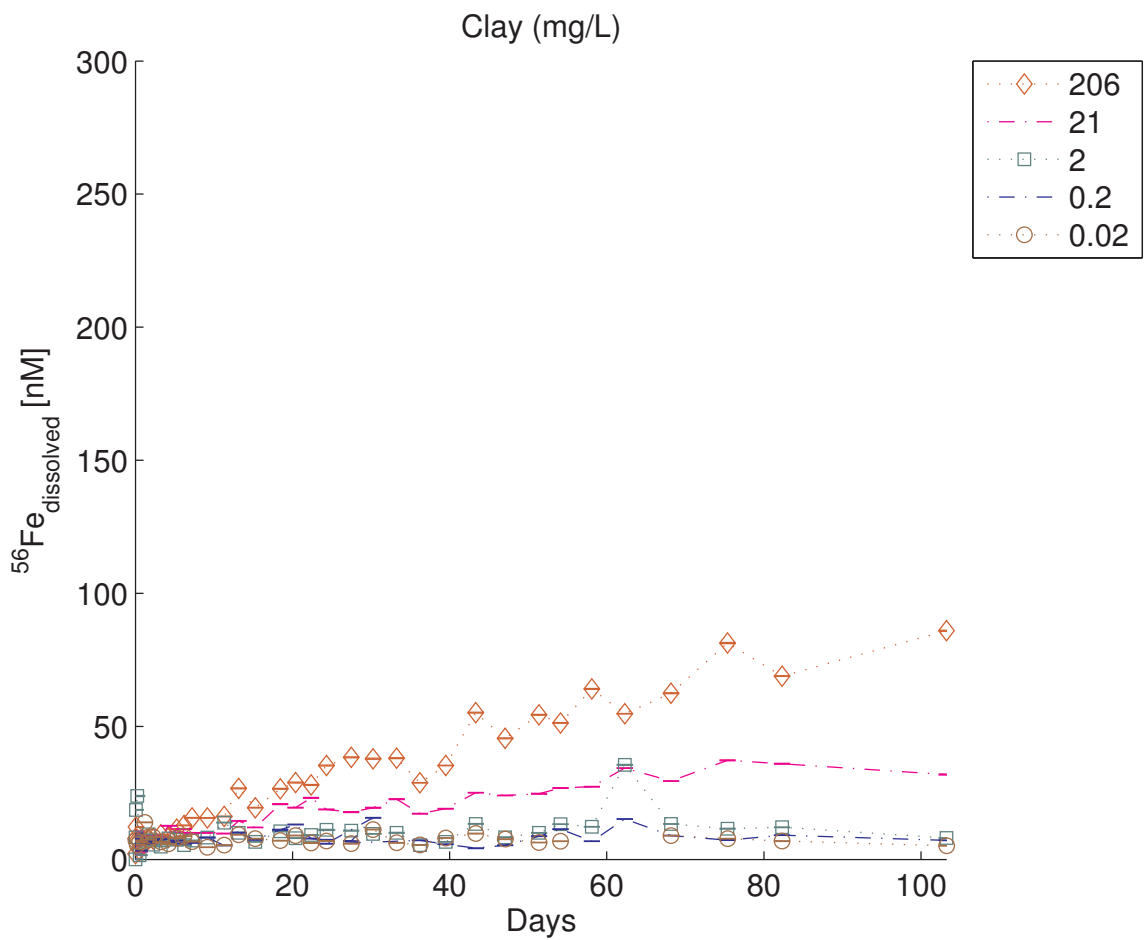
The desorption experiments are shown in Figure 4.6 alongside the ferrihydrite desorption experiment. During the adsorption period for the desorption experiment, the solution had an effective particle concentration of 250,000 mg/L. The non-ferrihydrite particles all show greater increases in ^{54}Fe over time into the dissolved phase than ^{56}Fe , suggesting that the ^{54}Fe was loosely absorbed to these particles. Ferrihydrite, as discussed previously, is the only particle type that has an approximately 100 nM increase in ^{56}Fe and a negligible increase in ^{54}Fe . The magnitude of ^{54}Fe increase among the various particles suggests that Fe will desorb readily from opal, forams, and clay when those particles move into areas of water with low Fe concentrations.

As for the desorption or dissolution of Fe from the non-ferrihydrite particles, the dissolved phase in the presence of montmorillonite and opal has similar increases in ^{56}Fe over time, again corresponding to increasing particle concentrations. The similarity of montmorillonite and opal desorption or dissolution suggests that these mechanisms are unrelated to their respective absorption capabilities of the particles. The increase in ^{56}Fe from forams also corresponds to particle concentration, though the overall magnitude of the increase is about half that of montmorillonite or opal. Goethite had the smallest change in ^{56}Fe concentration, confirming the refractory nature of this iron oxide. The invariance in ^{56}Fe among varying particle concentra-



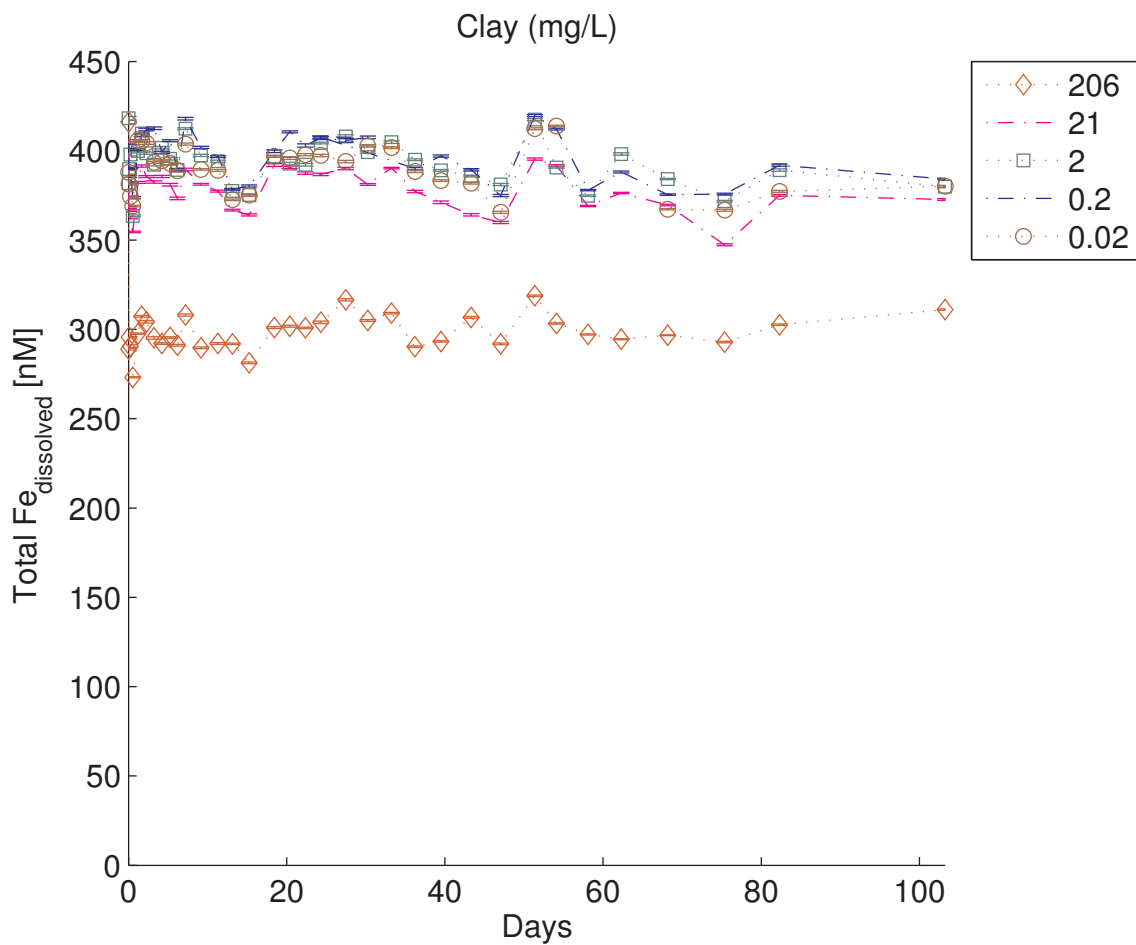
(a) The tracer concentration, ^{54}Fe (nM), vs. time. Tracer is immediately taken up by the dry montmorillonite, within 10 minutes, then has a second, more gradual linear absorption onto the clay over time. The absorption scales with particle concentration.

Figure 4.1. Montmorillonite absorption experiment. Legend indicates particle concentration (mg/L).



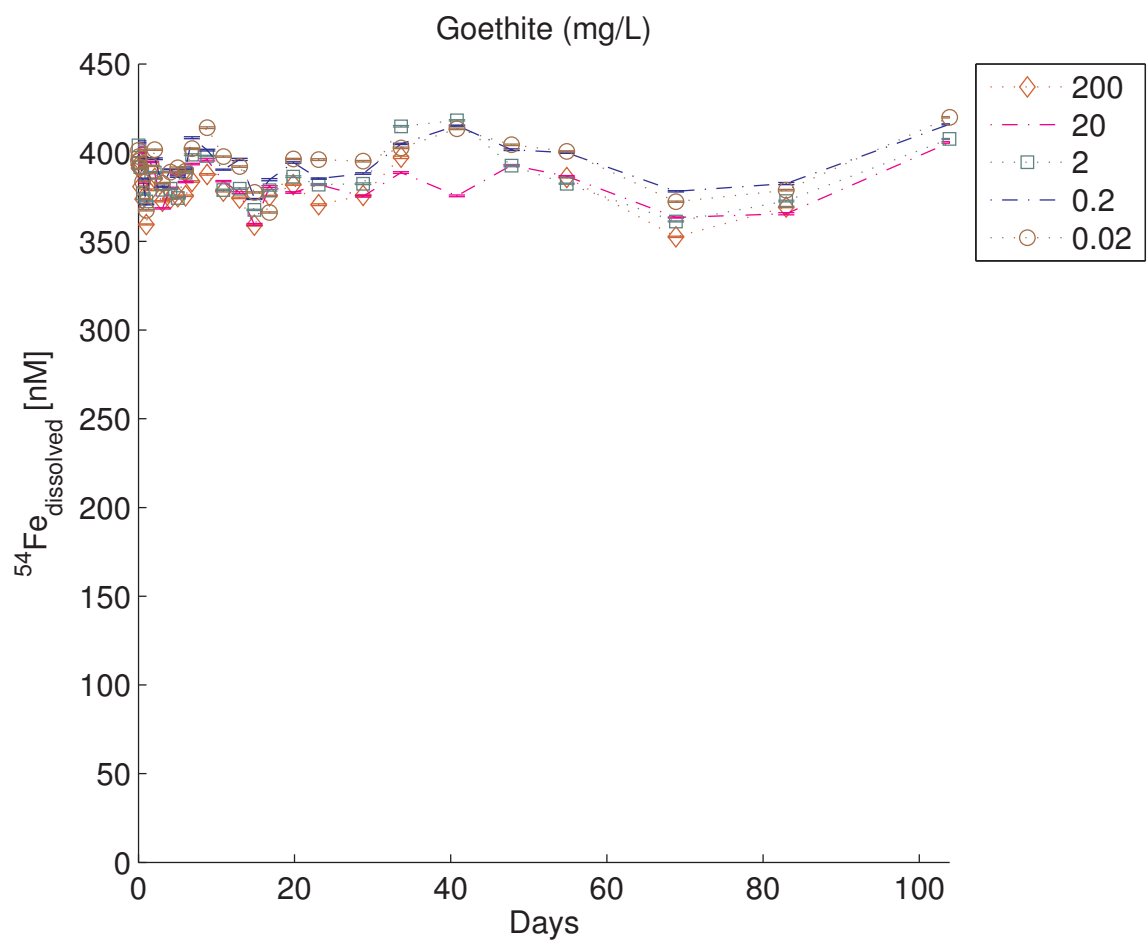
(b) The desorption of ^{56}Fe from montmorillonite into the dissolved phase over time. The amount of ^{56}Fe scales with particle concentration.

Figure 4.1. Montmorillonite absorption experiment. Legend indicates particle concentration (mg/L).



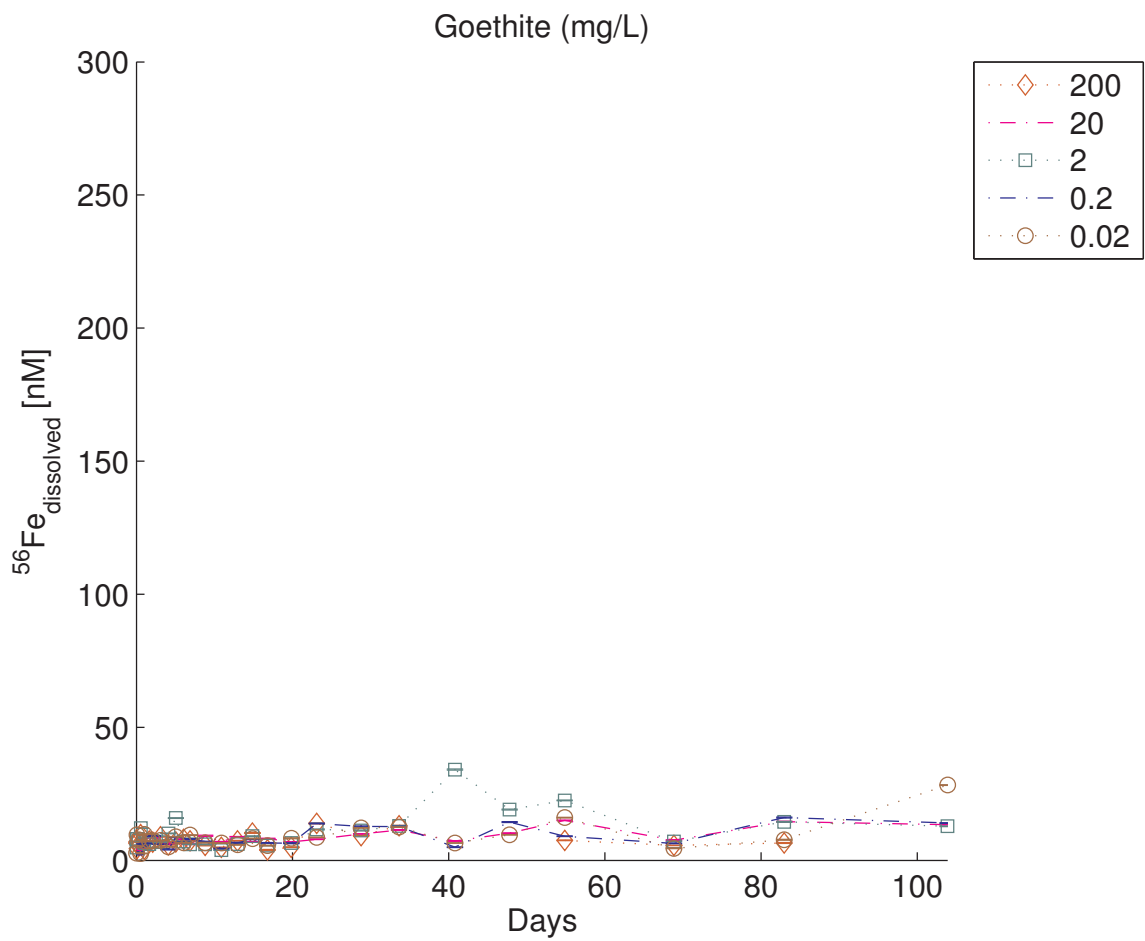
(c) The total amount of dissolved Fe (^{54}Fe and ^{56}Fe) over time. The concentration of total Fe is noticeably stable compared to the individual Fe isotopes measured in 4.1a and 4.1b, suggesting that after the fast, initial absorption that the Fe in the dissolved and particulate phases exchanges at similar rates.

Figure 4.1. Montmorillonite absorption experiment. Legend indicates particle concentration (mg/L).



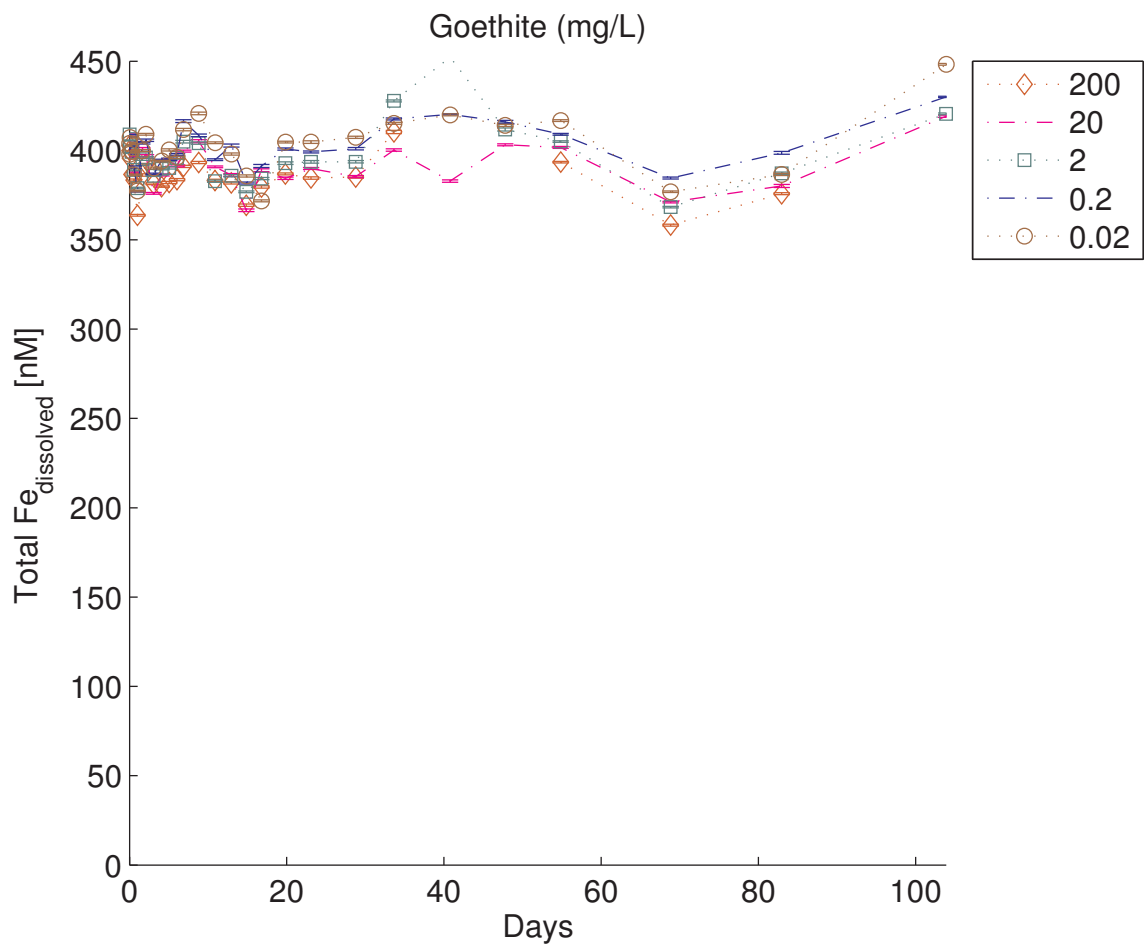
(a) The tracer ^{54}Fe in the presence of goethite shows little change over time.

Figure 4.2. Goethite absorption experiment. Legend indicates particle concentration (mg/L).



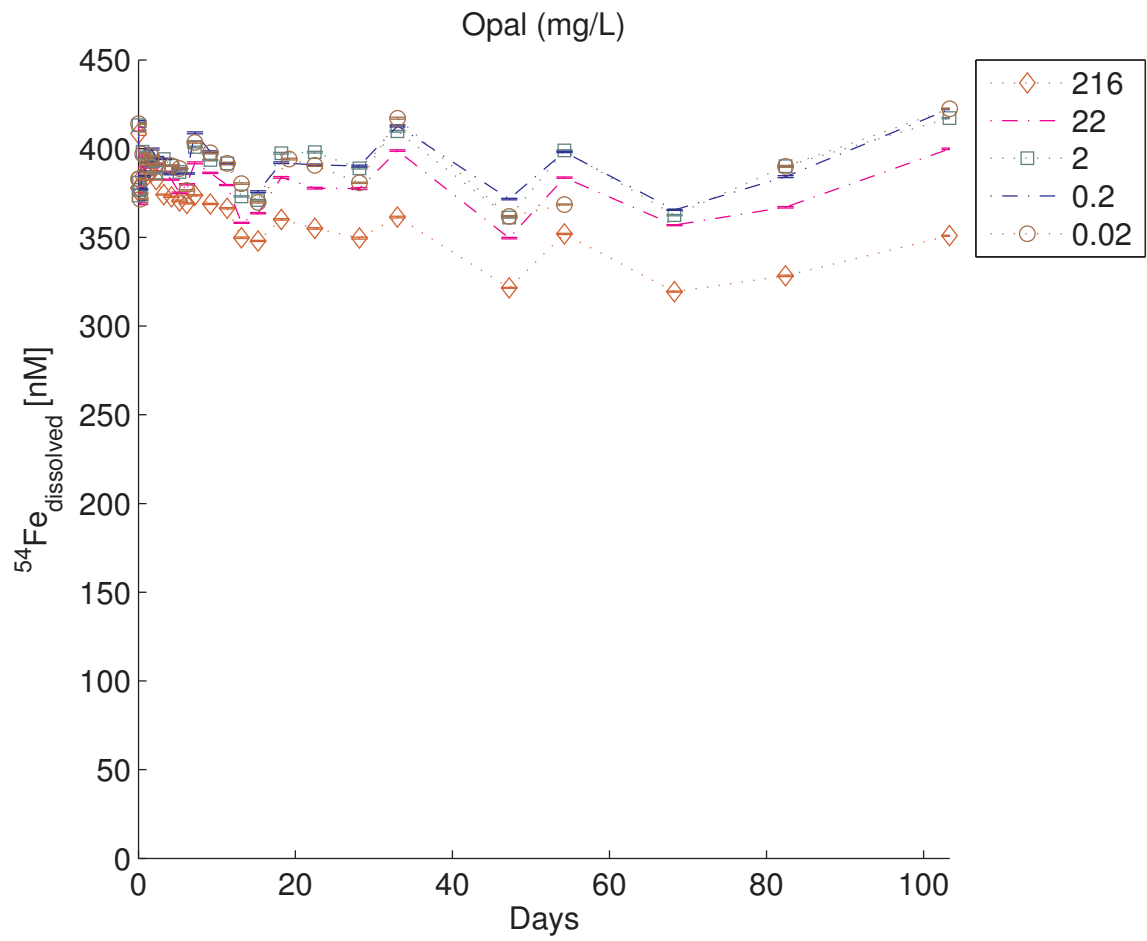
(b) Very little ^{56}Fe dissolves from the goethite over time.

Figure 4.2. Goethite absorption experiment. Legend indicates particle concentration (mg/L).



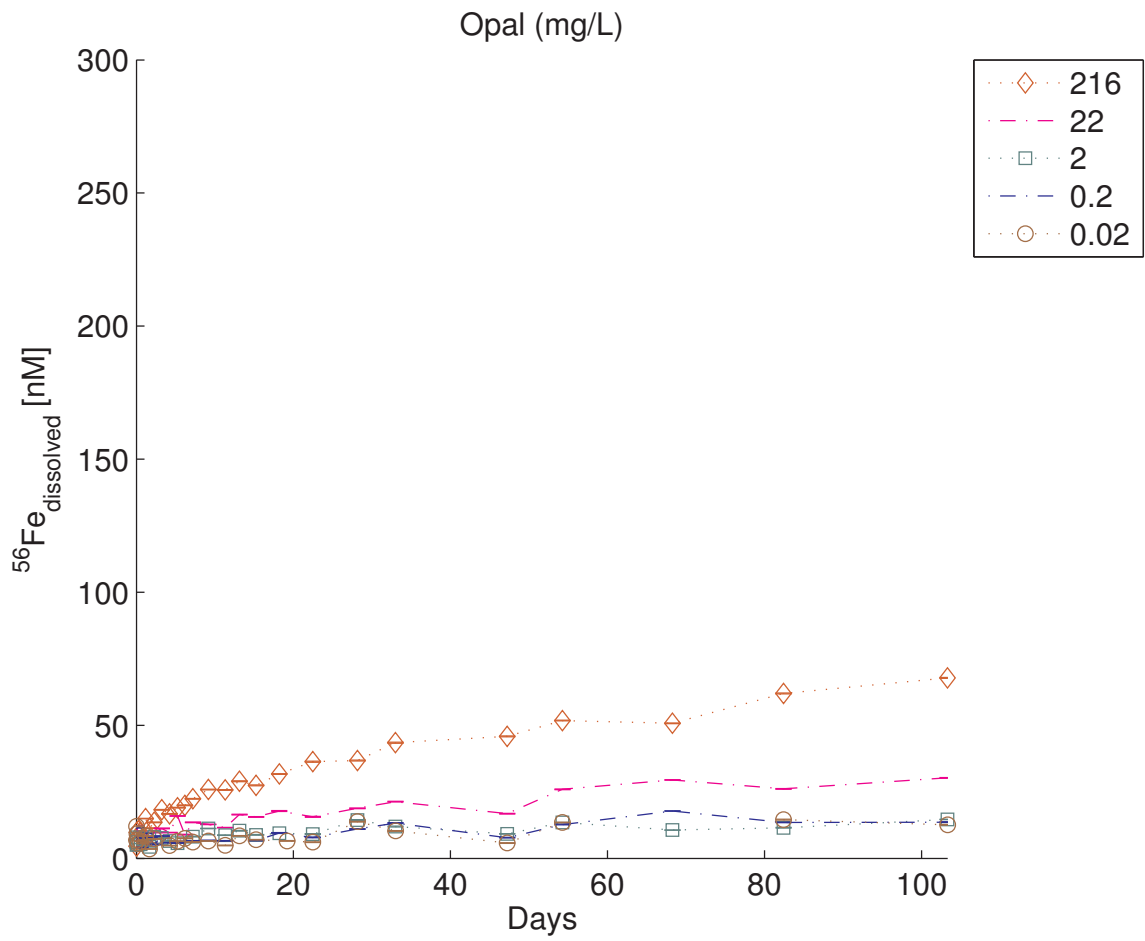
(c) The total amount of dissolved Fe (^{54}Fe and ^{56}Fe) over time remains fairly constant.

Figure 4.2. Goethite absorption experiment. Legend indicates particle concentration (mg/L).



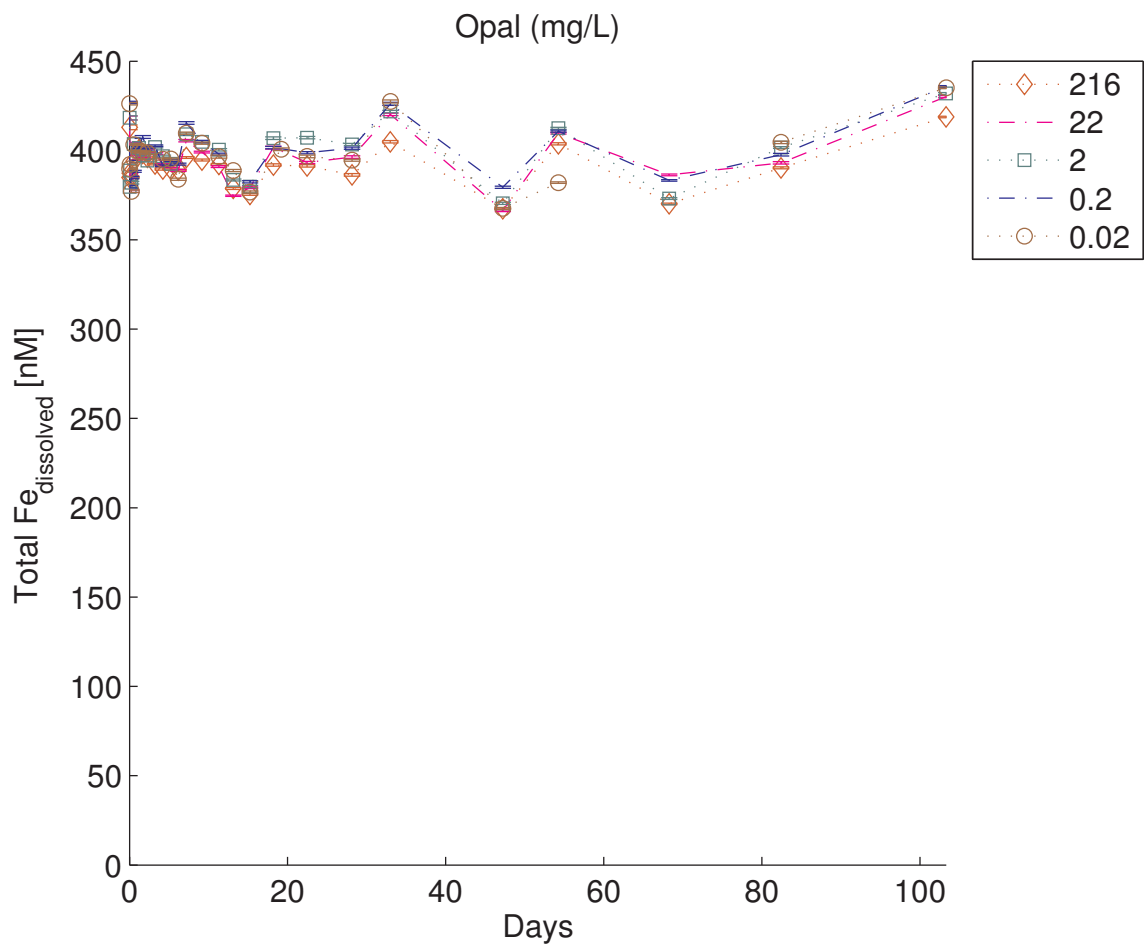
(a) The absorption of the tracer ^{54}Fe scales with particle concentration.

Figure 4.3. Opal absorption experiment. Legend indicates particle concentration (mg/L).



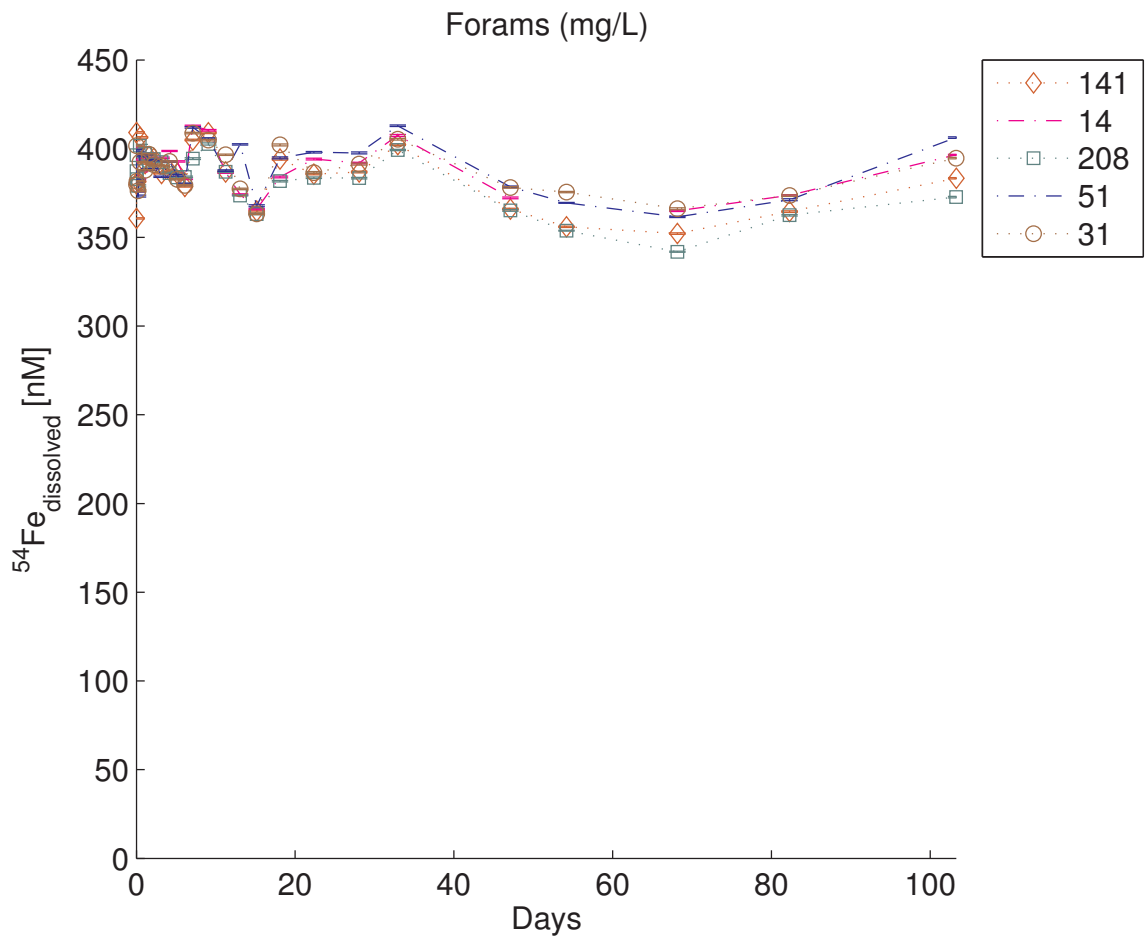
(b) Desorption of ^{56}Fe scales with particle concentration over time.

Figure 4.3. Opal absorption experiment. Legend indicates particle concentration (mg/L).



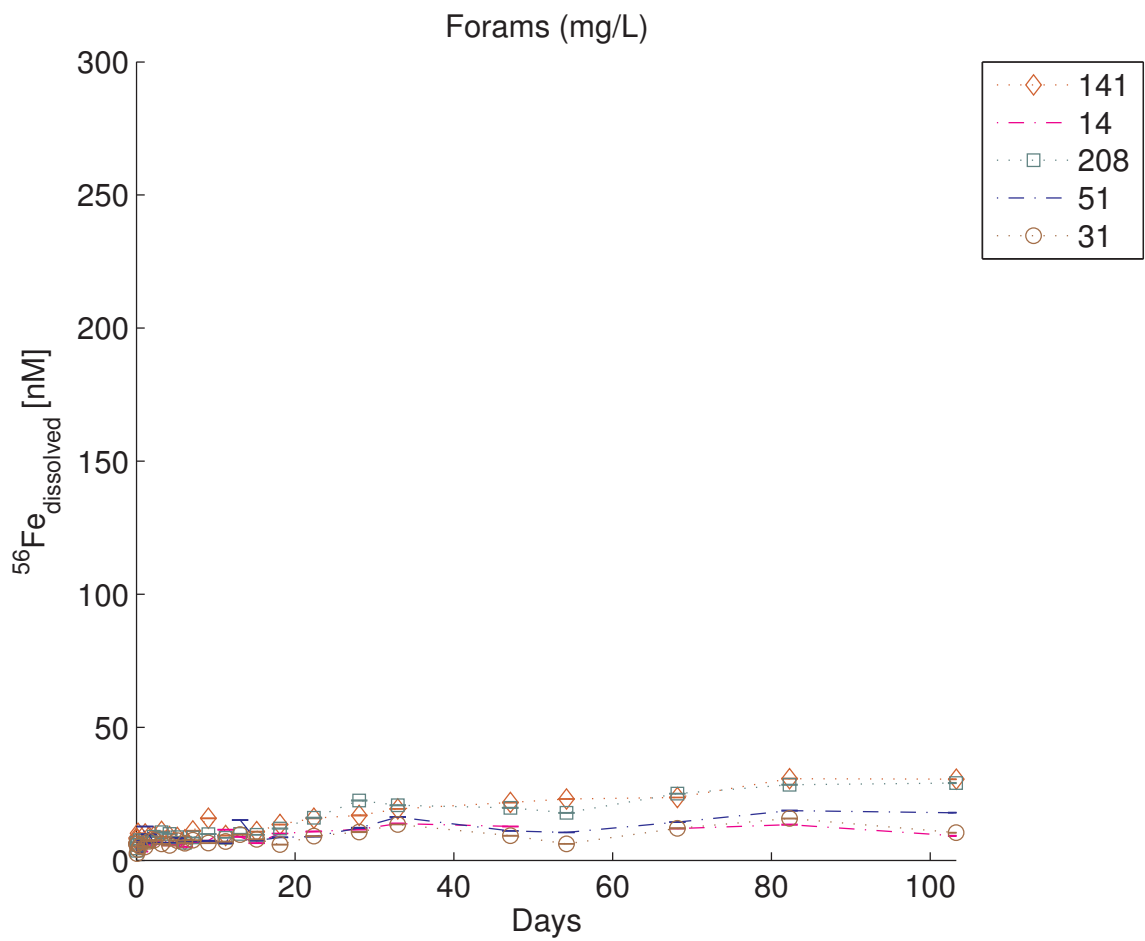
(c) The total amount of dissolved Fe (^{54}Fe and ^{56}Fe) over time remains fairly constant.

Figure 4.3. Opal absorption experiment. Legend indicates particle concentration (mg/L).



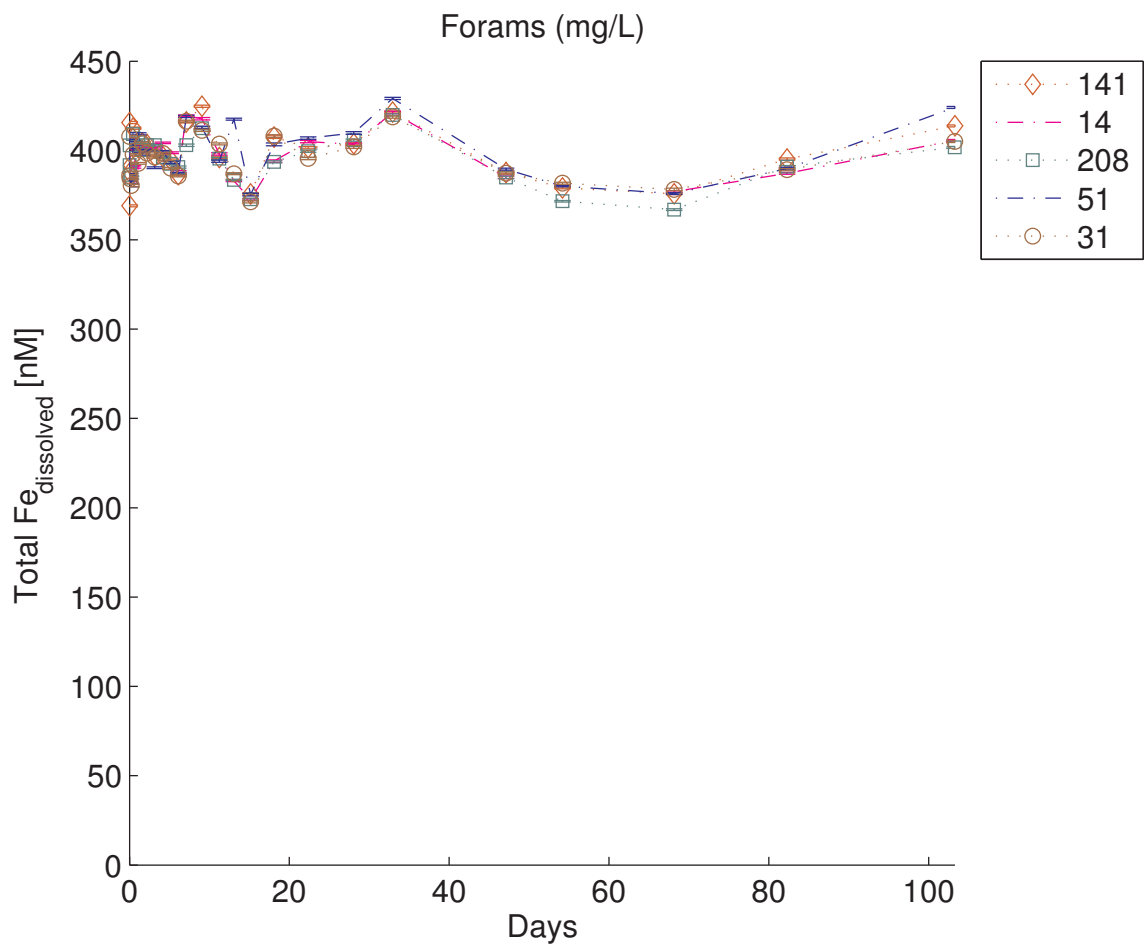
(a) The tracer ^{54}Fe scales very slightly in magnitude with particle concentration.

Figure 4.4. Forams absorption experiment. Legend indicates particle concentration (mg/L).



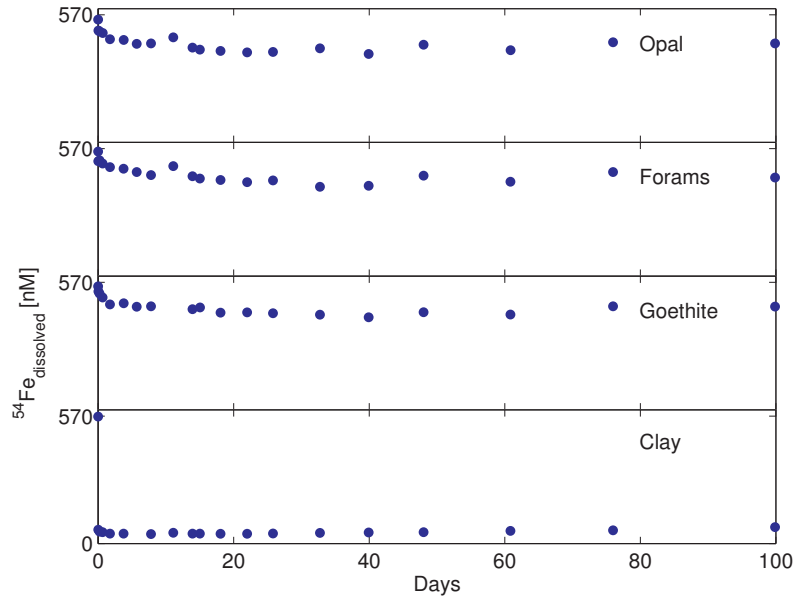
(b) Desorption of ^{56}Fe increases with increasing particle concentration.

Figure 4.4. Foram absorption experiment. Legend indicates particle concentration (mg/L).

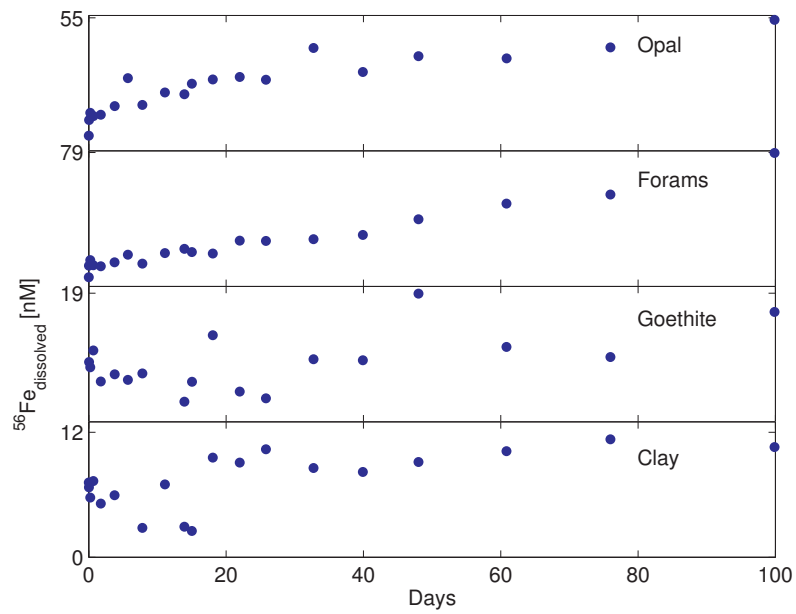


(c) The total amount of dissolved Fe (^{54}Fe and ^{56}Fe) remains fairly constant over time.

Figure 4.4. Foram absorption experiment. Legend indicates particle concentration (mg/L).

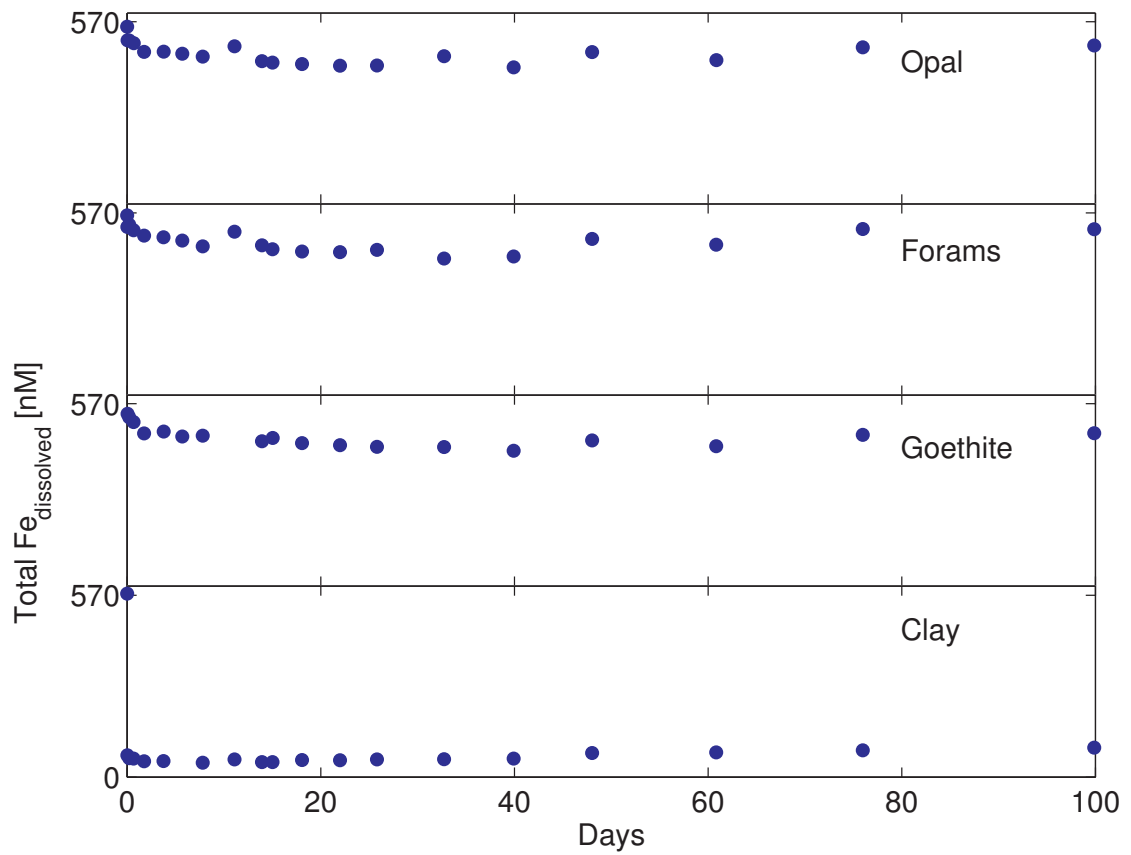


(a) Subplots of the tracer ^{54}Fe absorption over time in the presence of various particles. The y-axis is the same for all subplots.



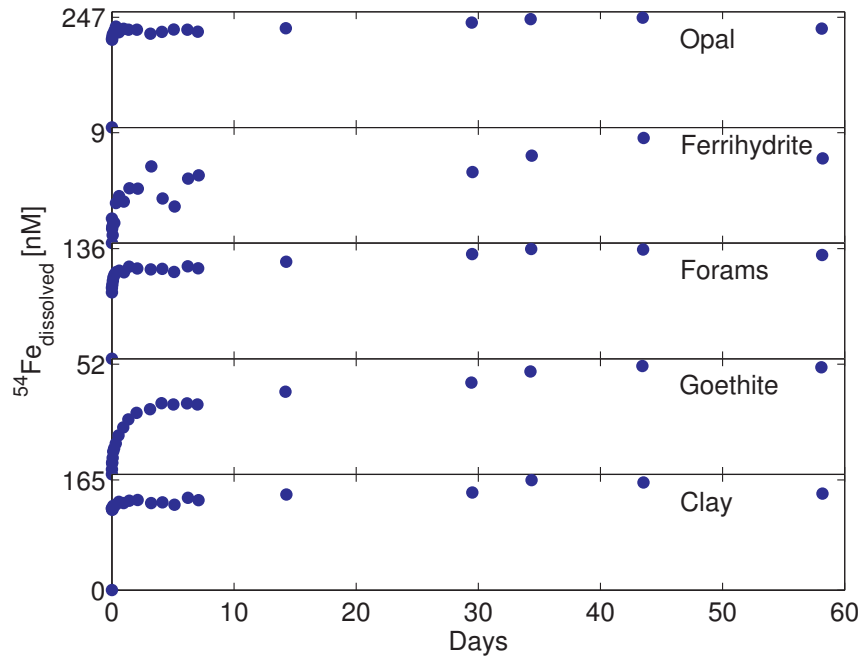
(b) Desorption or dissolution of ^{56}Fe over time from various particle types. The y-axis has been adjusted to maximize the range of concentrations for each particle type.

Figure 4.5. Largest particle concentration absorption experiment (6000 mg/L).

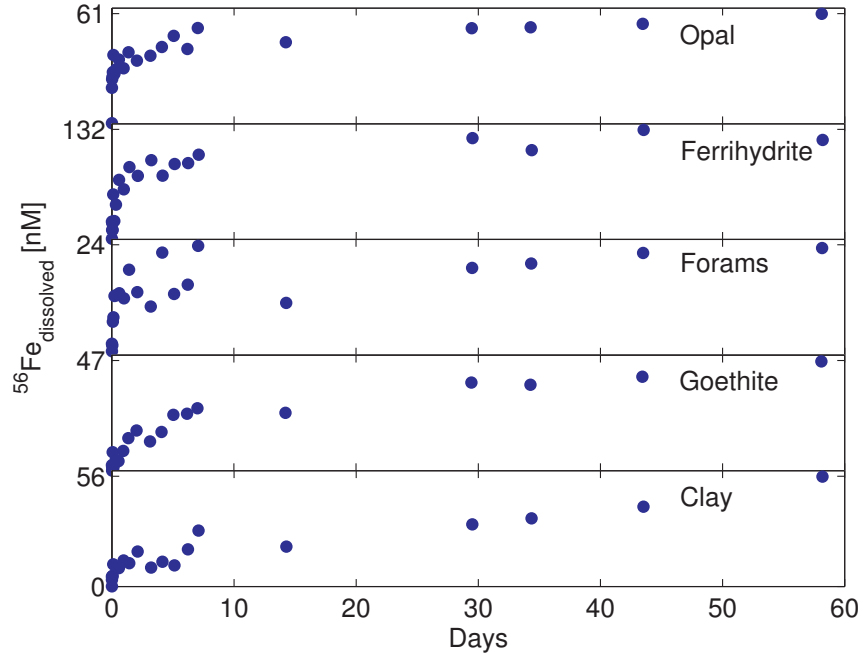


(c) The total amount of dissolved Fe (^{55}Fe and ^{56}Fe) over time. There are similar equilibrium levels of dissolved Fe in the presence of opal, forams, and goethite, less than 20% decrease in overall dissolved Fe. However, in the presence of dry clay, the dissolved total Fe decreases by over 80 % within 10 minutes of particle addition.

Figure 4.5. Largest particle concentration experiment for absorption (6000 mg/L).

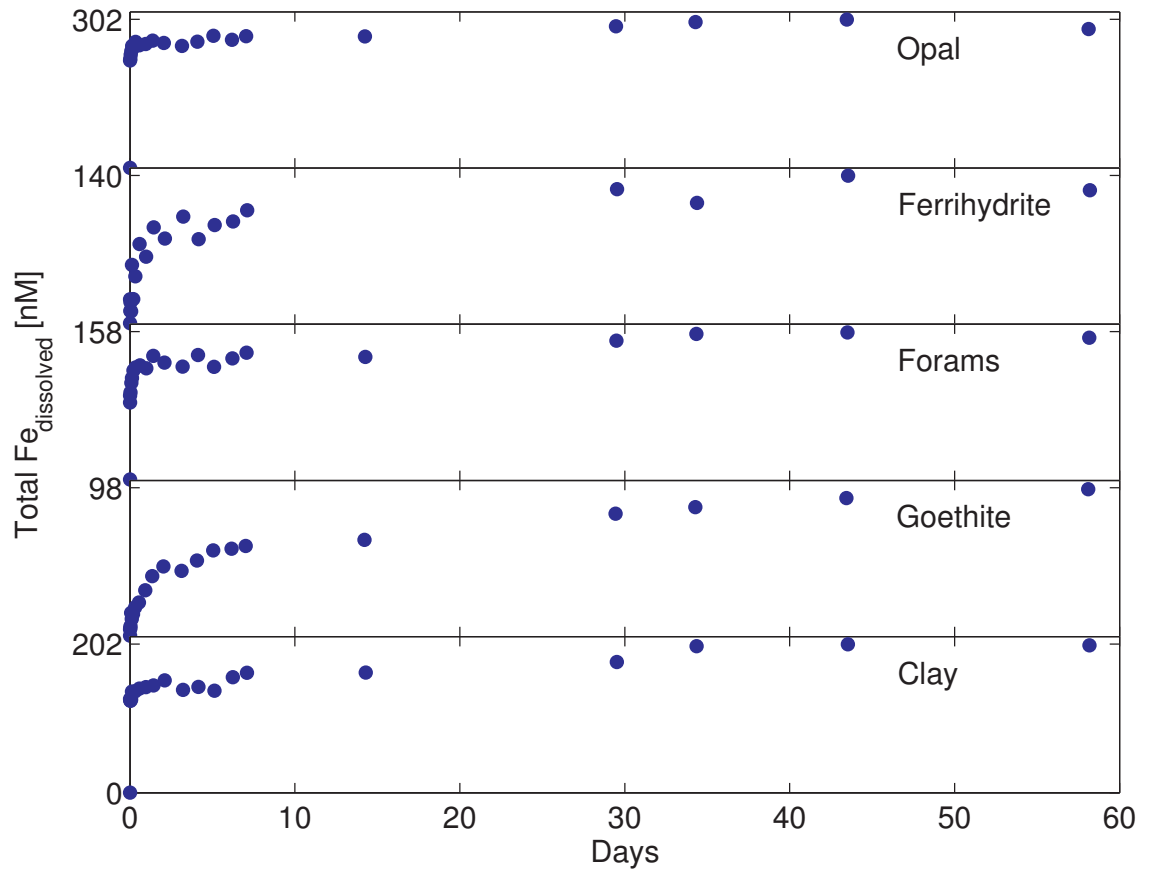


(a) ^{54}Fe



(b) ^{56}Fe

Figure 4.6. Desorption experiments.



(c) Total Fe

Figure 4.6. Desorption experiments.

tion also suggests that dissolution of Fe happens on a slow enough time scale that increasing particle concentration does little to affect dissolved Fe.

4.4 Discussion

4.4.1 Absorption Experiments

Since the dissolved phase in the presence of montmorillonite, goethite, forams, opal and even some of the lower ferrihydrite particle concentration ranges, seem to have reached steady state, a calculation of the partition distribution ratio is useful,

$$K_D = \frac{(\text{moles of Fe particulate/mass of particles})}{(\text{moles of Fe dissolved/volume of AQUIL})} \quad (4.2)$$

because K_D is a measure of the natural equilibrium between total Fe particulate and dissolved. The end result has units of mL/g. K_D should be constant across a range of particle concentrations for easy comparison of suspended particulate matter equilibrium across multiple field sites. We do not have measurements of actual Fe particulate concentrations from the filters throughout the experiments. An estimate was obtained by leaching the non-Fe particles in bulk and calculating the Fe in the iron oxides from chemical stoichiometry (Table 2.1). We have an estimate of the amount of Fe within a particle initially (M_{P_i}), a known starting concentration of the dissolved phase (M_{D_i}), and the total concentration of dissolved Fe at steady state (M_D), thus we calculate K_D via mass conservation

$$K_D = \frac{(M_T - M_D)/(M_D)}{C_P}, \quad (4.3)$$

where M_T is equal to the sum of M_{P_i} and M_{D_i} , and C_P is the concentration of particulate matter (g/mL). Additionally, for experiments where the loss of metal from the dissolved phase can be quantified and assumed to be absorbed onto the

particulate matter, then a calculation of

$$K_{Ds} = \frac{(\text{moles of absorbed Fe/mass of particles})}{(\text{moles of Fe dissolved/volume of AQUIL})},$$

$$K_{Ds} = \frac{(M_{Di} - M_D)/(M_D)}{C_P}, \quad (4.4)$$

can be done. Since three of our five particle types, goethite, opal, and forams, had no absorption, their K_{Ds} values would be zero, and positive K_{Ds} values can only be calculated for montmorillonite and ferrihydrite concentrations that had a measurable affect on the dissolved phase, assuming ferrihydrite has reached an equilibrium. Another insightful approach for our laboratory experiments, one which is also not feasible in the field, is to evaluate the normalized ratio of Fe that ended up in the particulate and dissolved phases respective to their initial values, where

$$K_{Df} = \frac{(M_T - M_D)/(M_{Pi})}{M_D/M_{Di}}. \quad (4.5)$$

These values tell us if there was a net shift in Fe to the particulate or dissolved fractions. This calculation normalizes for the initial Fe present, which makes interpretation of the equilibrium iron oxide data more straightforward. K_{Df} greater than 1 indicates net absorption and less than 1 means net dissolution or desorption. Also, since we have not normalized to particle concentration, we would expect to see K_{Df} scale with particle concentration.

Values for our experimental K_D , K_{Ds} , and K_{Df} , along with other experimental K_{Ds} or field site K_D values, are shown in Table 4.1. The other tracer experiments from the literature use a wide range of water matrices and particle or sediment types.

Overall, our K_D and K_{Df} values are fairly similar among the non-iron oxide particles, with the exception of montmorillonite. Montmorillonite partitioning increases only at higher concentrations, above 2 mg/L, suggesting that there is a threshold FeDFB to suspended particulate matter (SPM) ratio where there are enough reactive sites to have an effect on the ligand-dominated dissolved phase. Clearly there is a net adsorption of FeDFB into this dry, layered 2:1 clay type. The swelling clay

pulls water in and takes Fe with it. This threshold occurs going from a ratio of 200 to 20 for FeDFB:[particle] for montmorillonite. The K_{Ds} values for montmorillonite from the reference were experiments performed in filtered coastal water with cationic Fe^{3+} . While there may have been some organic ligands present, they most likely were already complexed with Fe in the dissolved and colloidal phases. Their K_{Ds} values show greatly increased Fe affinity, and this could be due to lack of excess ligand to sequester Fe^{3+} in the dissolved phase before the montmorillonite rapidly absorbs the Fe^{3+} .

The ferrihydrite and goethite, which obviously have a high particulate Fe concentration, have similar K_D values to the two field sites where natural K_D values were measured, indicating that the affinity for FeDFB to iron oxides in our experiments is similar to that in a gulf or estuary. This could be due to the higher dissolved Fe abundance in river water that flocculates upon reaching the brackish coastal waters and drastically increases the Fe in the particulate phase in these regions.

Ferrihydrite has a dynamic range of K_{Ds} and K_{Df} . From the lowest particle concentrations to the highest, the K_{Ds} values decrease, suggesting more affinity for the dissolved phase. This notable trend could be a sign of the particle concentration effect [29]. This effect is due to the increasing amount of colloid associated Fe with higher SPM, which are not included in particulate Fe, and gives the appearance of higher dissolved phase affinity. In fact, the ferrihydrite K_{Df} indicates the opposite, and shows an increasing partitioning of Fe to the particulate phase with higher particle concentration. Ideally K_{Ds} should be constant across particle concentrations if the system is at equilibrium. Corrections for colloids and for large particles that have few surface sites per gram could result in truly constant K_{Ds} values [55, 104].

The lower values of our experimental K_{Ds} for montmorillonite and ferrihydrite compared to the other tracer experiments underscore the ability of ligand-bound Fe, particularly strong siderophores, to retain Fe in the dissolved phase. The variability among the other experimental K_{Ds} is most likely a result of the different background concentrations of ligand in experiments with natural filtered waters and the different particle compositions.

4.4.2 Desorption

The results from the desorption experiments are somewhat more qualitative because attempts to measure the amount of remaining Fe in solution after the high “absorption” period were unsuccessful. The solution was too limited to obtain an accurate measurement from filtering. The original intention was to force absorption onto the particle surfaces to see how quickly the Fe came back into solution, though we cannot quantify how much FeDFB absorbed onto the surfaces.

The non-ferrihydrate particles all show enhanced increase in ^{54}Fe over time in the dissolved phase, above any increase in ^{56}Fe , suggesting that the ^{54}Fe was loosely absorbed to these particles. Ferrihydrate is the only particle type that has a 100 nM increase in ^{56}Fe and a minimal increase in ^{54}Fe . The magnitude of ^{54}Fe increase among the various particles suggests that Fe will desorb readily from opal, forams, and clay when those particles move into areas of water with low Fe concentrations, whereas ferrihydrate will simply begin dissolving in the presence of ligands.

4.5 Conclusions

The notably absent reactivity of FeDFB with goethite, forams, and opal is striking compared to the varied absorptivity of ferrihydrate and montmorillonite. FeDFB is very stable in the presence of some particle types, but the absorptive capabilities of a fresh, labile iron oxide and a swelling clay can compete with ligand-bound Fe. These differences are due to the type of particle reaction sites and structure, their particle size fractions, and their affinity for Fe. Particle composition obviously has a varied effect on dissolved Fe in the ocean, even in the presence of siderophores. An optimal model would incorporate particle composition and corresponding exchange rates to show how dissolved Fe would change as particles fall through the water column.

Table 4.1. Our experimental values (*) for $\log K_D$ and $\log K_{D_s}$, if significant sorption occurred, are listed, respectively, in the same column and K_{D_f} values in a separate column. Experiments that used tracers with various particle and water types [68, 105, 102, 55] to determine the distribution of sorbed tracer versus dissolved, K_{D_s} values, are denoted by subscript D_s . K_D values, particulate vs. dissolved distribution, for natural field site measurements of coastal and estuary water [106, 107] are indicated by subscript D . All ferrihydrite values are from this work, Set 1 and Set 2 experiments, as described in Chapter 3. Particle concentrations (mg/L) are included for most values. Particulate ($> 0.45 \mu\text{m}$) and colloid ($0.04\text{--}0.45 \mu\text{m}$) K_D values are indicated in the estuary studies. Approximate sampling locations are indicated for samples taken within the Gulf of California.

Particle Type	[Particle] (mg/L)	$\log(K_{D/D_s})$	K_{D_f}	Matrix	Reference
Montmorillonite	206	3.72/3.21	1.92	AQUIL	*
	21	3.73/3.40	1.96	AQUIL	*
	2	3.44/–	1.00	AQUIL	*
	0.2	3.44/–	1.00	AQUIL	*
	0.02	3.44/–	1.00	AQUIL	*
	650	5 D_s		coastal SW	[68]
	10	6.2 D_s		coastal SW	[68]
Ferrihydrite	570	7.10/3.39	2.40	AQUIL	set 1
	349	7.03/3.45	2.00	AQUIL	set 1
	172	6.90/3.46	1.50	AQUIL	set 1
	33	6.83/3.90	1.26	AQUIL	set 1
	208	6.99/3.05	1.23	AQUIL	set 2
	21	6.92/3.40	1.05	AQUIL	set 2
	2	6.92/4.42	1.06	AQUIL	set 2
	0.2	6.94/–	1.09	AQUIL	set 2
	0.02	7.04/–	1.38	AQUIL	set 2

continued on next page...

continued from previous page

Particle Type	[Particle] (mg/L)	$\log(K_{D/D_s})$	K_{Df}	Matrix	Reference
Opal	200	3.22/–	0.80	AQUIL	*
Goethite	200	7.42/–	0.94	AQUIL	*
	20	7.42/–	0.94	AQUIL	*
	2	7.42/–	0.94	AQUIL	*
	0.2	7.42/–	0.93	AQUIL	*
	0.02	7.37/–	0.84	AQUIL	*
	<100	>7 D_s		coastal SW	[68]
Forams	208	3.26/–	1.00	AQUIL	*
	141	3.26/–	1.00	AQUIL	*
	51	3.26/–	1.00	AQUIL	*
	31	3.26/–	1.00	AQUIL	*
	14	3.26/–	1.00	AQUIL	*
MnO₂	50	6.7 D_s		coastal SW	[68]
Hematite	–	5.5 D_s		synthetic	[55]
Cariaco Trench sediment	25	4.1 D_s		deep SW	[68]
Remote Marine aerosol	60	7.7 D_s		open ocean	[102]
	3	6.4 D_s		open ocean	[102]
Gulf of California	38 (central)	6.92 D		–	[106]
	38 (coastal)	5.85 D		–	[106]
Vienne River, France	0.4 (colloids)	6.5 D_s		freshwater	[105]
	8 (colloids)	5.5 D_s		freshwater	[105]
	20 (colloids)	4.5 D_s		freshwater	[105]
	– (particulate)	5.25 D_s		freshwater	[105]
Galveston Bay	2 to 40	7 to 5 D		–	[107]

Chapter 5

Fe Isotopic Fractionation in the Presence of Particles

5.1 Introduction

Atmospheric dust has been touted as the main source of Fe to the open ocean, however recent work suggests that lateral transport of Fe from continental margins could be just as significant. Fe profiles in the eastern and western sub-arctic Pacific show evidence for a subsurface supply of Fe that is accessible to the surface through seasonal upwelling and vertical mixing [108, 109, 110]. The subsurface Fe has a more reduced oxidation state, which is indicative of continental margin sediments. Constraining the Fe sources in the ocean will lead to a better understanding of the impact on productivity, especially in the open ocean or HNLC regions where Fe sources are limited.

Isotopes of Fe offer a potential way of “fingerprinting” the different sources and processes that lead to input and removal of dissolved Fe. With each phase change, oxidation state change, or biota uptake, Fe isotopes can be fractionated between the competing pools. Isotopic signatures have been observed for a number of potential Fe sources. Atmospheric aerosols, mostly from lithogenic sources, have a very narrow isotopic range of 0‰ to +0.2‰ [111]. Isotopically light Fe, characteristic of Fe(II), has been measured in anoxic pore waters, -2.96‰ to -1.3‰, and to a lesser extent in hydrothermal fluids, -0.67‰ to -0.09‰ [112, 113, 114]. Biological and abiotic processes will also create fractionation, including precipitation [115] and ligand-promoted dissolution of minerals [116]. The isotopic source signatures and fractionating processes

could leave a quantitative imprint on the dissolved phase, thus creating constraints on the relative Fe contributions in the Fe cycle.

Recent advances have been made towards measuring Fe isotopic composition of the dissolved phase at the low concentrations, 0.01 to 1 nM, found in seawater [117, 96]. There are now open-ocean isotopic profiles in the Southern Ocean, equatorial Pacific, the Bermuda Atlantic Time Series (BATS), and in California coastal waters at the San Pedro Basin. The Atlantic section of the Southern Ocean contains both isotopically light $\delta^{56}\text{Fe}$ minimums (-0.13‰) and enriched maximums (+0.21‰), hypothesized to be from organic matter remineralization and phytoplankton uptake, respectively [117]. In the equatorial Pacific, the dissolved $\delta^{56}\text{Fe}$ values are mostly positive (+0.01‰ to 0.58‰) with most variation occurring within the vertical direction and little difference between the 2 stations that are 2400 miles apart, suggesting Fe isotopic signatures can be carried laterally along water masses [118]. The San Pedro Basin has 2 isotopically light minimums, corresponding to input of reduced sediments given the topography of the region [96, 119]. BATS, similar to the equatorial Pacific, is also enriched throughout the water column, with a maximum at depth hypothesized to be due to hydrothermal vent Fe inputs [120]. The total Fe-dissolved profile at BATS is dynamic, yet maintains a fairly constant isotopic composition around +0.3‰. This consistency is hypothesized to be due to a rapid exchange with particles in the water column.

These laboratory experiments will attempt to answer the following questions related to particle effect on dissolved Fe. What is the isotopic composition of the Fe dissolved phase in the presence of common marine minerals? Does it change with particle type? How do these laboratory isotopic fractionations compare to Fe isotopic profiles in the ocean?

5.2 Brief Experimental Setup

As described in Chapter 2, eighty bottles of AQUIL were prepared with natural abundance FeDFB in 1:1, either 400:400 nM or 1000:1000 nM, and 400:1000 nM ratios in a 100 mL volume. 66 bottles had clay or ferrihydrite at six different particulate

concentrations (0.02 to 3000 mg/L) because their isotopic effect is of interest due to their strong exchangeability, as noted in the kinetic experiments. There was one bottle each of goethite, forams, or opal particles at the 1:1 FeDFB and at a high particle concentration (2500 mg/L). There were controls with no particles at the three ratios of Fe to DFB. The matrix of experiments is in Section 2.7, Table 2.4. After 3 months of shaking in the dark, the bottles were all filtered, purified through anion exchange column chemistry, and analyzed on the Neptune ICP-MS to determine $\delta^{56}\text{Fe}$ of the dissolved phase relative to IRMM-14. Additional samples were analyzed for their $\delta^{56}\text{Fe}$ values without further purification, including ferrihydrite precipitates that had never been exposed to the AQUIL solutions, the FeDFB solution in milliQ at pH 3, and the acidified Fe standard solution.

5.3 Results

Table 5.1 lists $\delta^{56}\text{Fe}$ values for all the sample types and particle concentrations and the controls (no particles). The $\delta^{56}\text{Fe}$ values are an average of intermediate replicates, the same purified sample run during multiple analytical sessions, and external bottle replicates for experiments set up in triplicate. Variance in the data is given as 1 standard deviation. The dissolved phase [Fe] at the time of sampling and its respective variance, initial [Fe], and initial [DFB] values are also noted for each sample or control. Fe remaining in the dissolved phase relative to the initial [Fe] is given in the final column. As noted in Section 2.8, the two highest-particle-concentration bottles for montmorillonite and ferrihydrite are excluded owing to their high blank contamination.

The end member value of the Fe standard, used in the FeDFB solution, and the FeDFB solution itself are close to 0‰ $\delta^{56}\text{Fe}$, meaning there is insignificant fractionation of the Fe during equilibration with DFB. The bulk solid phase ferrihydrite value is 0.13‰, indicating that during precipitation the heavier ^{56}Fe was preferentially recruited into the solid phase. This result is opposite of the expected kinetic isotope effect, and a more detailed study of precipitation’s effect on the dissolved phase and

bulk or leachable solid phase is warranted. The control bottles have some amount of fractionation without any particles present, and the samples with particles in AQUIL had their respective control bottle subtracted, listed as $\Delta(\delta^{56}\text{Fe}_{\text{sample-control}})$. The $\Delta^{56}\text{Fe}$ values range from -0.14‰ to 0.12‰ for montmorillonite. The ferrihydrite sample $\Delta^{56}\text{Fe}$ values have a much larger range, from 0.05 to 1.19‰. The other particle types, goethite, forams, and opal, have a tight range, from 0.10‰ to 0.16‰.

Type	Matrix	$\delta^{56}\text{Fe}$	(1 SD)	Δ ($\delta^{56}\text{Fe}_{\text{sample-control}}$)	[Part] mg/L	[Fe] ^{diss} nM	(1 SD)	[Fe] _i nM	[DFB] _i nM	[Fe] _{diss/i}
Control	AQUIL	0.39	0.02	--	0	304	7	400	400	0.76
Ferrihydrite	AQUIL	1.21	0.07	0.82	320	207	4	400	400	0.52
Ferrihydrite	AQUIL	0.48	0.06	0.09	3	271	4	400	400	0.68
Ferrihydrite	AQUIL	0.46	0.02	0.06	0.3	289	1	400	400	0.72
Clay	AQUIL	0.39	0.03	0.00	116	241	2	400	400	0.60
Clay	AQUIL	0.26	0.06	-0.14	2	291	2	400	400	0.73
Clay	AQUIL	0.38	0.04	-0.01	0.2	290	10	400	400	0.72
Clay	AQUIL	0.27	0.01	-0.13	0.02	292	13	400	400	0.73
Control	AQUIL	0.05	0.03	--	0	370	4	400	1000	0.93
Ferrihydrite	AQUIL	1.25	0.11	1.19	320	566	4	400	1000	1.41
Ferrihydrite	AQUIL	0.42	0.08	0.37	0.3	814	21	400	1000	2.03
Clay	AQUIL	0.17	0.04	0.12	116	407	8	400	1000	1.02
Clay	AQUIL	0.15	0.01	0.10	0.2	366	2	400	1000	0.91
Control	AQUIL	0.30	0.02	--	0	722	7	1000	1000	0.72
Opal	AQUIL	0.45	0.04	0.15	2450	671	5	1000	1000	0.67
Goethite	AQUIL	0.46	0.04	0.16	2440	631	5	1000	1000	0.63
Forams	AQUIL	0.40	0.01	0.10	2490	689	5	1000	1000	0.69
Ferrihydrite	AQUIL	1.26	0.03	0.95	320	522	20	1000	1000	0.52
Ferrihydrite	AQUIL	0.35	0.06	0.05	3	686	4	1000	1000	0.69
Ferrihydrite	AQUIL	0.39	0.03	0.08	0.3	706	7	1000	1000	0.71
Clay	AQUIL	0.31	0.07	0.01	116	612	1	1000	1000	0.61
Clay	AQUIL	0.38	0.04	0.08	2	684	10	1000	1000	0.68
Clay	AQUIL	0.32	0.05	0.02	0.2	730	6	1000	1000	0.73
Clay	AQUIL	0.28	0.04	-0.02	0.02	729	6	1000	1000	0.73
Ferrihydrite	2% HNO ₃	0.13	0.04	--	--	--	--	--	--	--
FeDFB	milliQ	0.05	0.03	--	--	--	--	--	--	--
Fe Standard	2% HNO ₃	0.00	0.03	--	--	--	--	--	--	--

Table 5.1. Isotope data

5.4 Discussion

The behavior of the control bottles and their respective fractionations are interesting to note. The controls with a 1:1 ratio of FeDFB each lost approximately 25% Fe and had $\delta^{56}\text{Fe}$ values of 0.39‰ and 0.30‰ for the lower and higher FeDFB concentrations, respectively. The bottle with the 400:1000 FeDFB ratio retained most of its Fe and had very little fractionation, 0.05‰. This suggests that a 1:1 ratio of Fe:DFB cannot compete with the surface area of the bottle in the presence of AQUIL, and loss of Fe to the bottle walls preferentially favors light ^{54}Fe .

To better understand the changes in the montmorillonite and ferrihydrite equilibrations, their $\Delta^{56}\text{Fe}$ values versus relative amount of [Fe] are plotted in Figures 5.1 and 5.2, with a zoomed-in region of the values close to 0‰ shown in Figure 5.4.

Montmorillonite (Figure 5.1) causes relatively little fractionation compared to ferrihydrite. The fractionations are all around 0‰ for 1:1 FeDFB ratios, with Fe retention in the dissolved phase from 0.60 at the highest particle concentration of 116 mg/L to 0.73 for the lowest, 0.02 mg/L. However, at the higher ratio of DFB to Fe, there is an ever-so-slightly enriched average signature of 0.12‰ and 0.10‰. While this higher isotopic mean may not be statistically significant, it suggests that DFB has preferentially desorbed ^{56}Fe from the montmorillonite. Overall, the montmorillonite seems to be indiscriminately absorbing ^{54}Fe and ^{56}Fe when it takes in water. The natural exchange of pre-wetted montmorillonite with FeDFB in AQUIL might give a more accurate estimate of its typical fractionation for clay-associated river sediments that empty into the ocean. Our observation of little fractionation is more relevant for surface waters that have aerosol deposition with a montmorillonite-like composition.

The $\Delta^{56}\text{Fe}$ versus relative amount of dissolved Fe to initial Fe is shown in Figure 5.2. Ferrihydrite has a fractionation pattern that scales with both particle amount and ligand concentration relative to Fe. For the 1:1 ratio FeDFB experiments, there is an increasing net loss of dissolved phase Fe with relative fractions of 0.72, 0.68, and 0.52 for 0.3 mg/L, 3 mg/L, and 320 mg/L ferrihydrite, respectively. The fractionation pattern also roughly scales with decrease in the dissolved phase with little difference

between the 2 lower particle concentrations, 0.05‰ to 0.09‰, and an order of magnitude jump at the highest particle concentration, 0.82‰ to 0.95‰. This jump in enriched Fe is probably due to a combination of losing ^{54}Fe from the dissolved phase, and gaining ^{56}Fe from the particulate phase. The enriched signature of the control bottles confirms losing ^{54}Fe preferentially from the dissolved phase. The increase in ligand concentration beyond a 1:1 ratio with $[\text{Fe}]_i$ promotes ferrihydrite dissolution and further enriches dissolved Fe. In fact, the higher ligand-to-Fe experiments in the presence of ferrihydrite were the only 2 experiments that increased the relative amount of Fe in the dissolved phase. The clay and control experiments bottles at 400:1000 FeDFB merely retained their initial Fe level, around 0.91 to 1.02 relative $[\text{Fe}]$. At 320 mg/L ferrihydrite, the amount of dissolution in the presence of excess DFB was negated by particle absorption since its relative fraction was 1.41, compared to 2.03 for 0.3 mg/L ferrihydrite. When excess ligand is present and no additional Fe source presents itself, then the ligand acts to preserve the isotopic composition of the dissolved phase by reducing Fe loss. However, in the presence of inorganic Fe sources, the excess ligand will also pull ^{56}Fe into the dissolved phase.

Given that the fractionation pattern varied between FeDFB ratios and amount of relative dissolved Fe (the black and grey bold arrows, Figure 5.2), a more consistent relationship is found in the fractionation versus particle concentration. The isotopic fractionation in the presence of ferrihydrite can potentially be quantified. The relationship between particle concentration and fractionation ($\Delta^{56}\text{Fe}$) to a first approximation is linear (Figure 5.3), $0.0026 \pm 0.0001 \Delta^{56}\text{Fe}/(\text{mg/L})$ with an offset of around 0.30‰, for the 400:1000 experiments. This slope represents the amount of fractionation caused by uptake onto particles, while the offset represents the fractionation caused by increased dissolution. Since the offset is constant between the middle and highest ferrihydrite concentrations, where the threshold of particulate matter is high enough to have a noticeable fractionation, the dissolution is indeed set by the amount of excess ligand, which is also constant between the two. The net dissolved Fe is a combination of these two factors, absorption and dissolution, as discussed in Chapter 3.

The result that the dissolved phase becomes enriched in the presence of various particles is consistent with the hypothesis for the BATS profile and the observation of the enriched equatorial Pacific profiles. Fresh, labile iron oxides will have the largest single fractionation impact on the dissolved phase from preferential ^{56}Fe ligand-promoted dissolution. However, the initial isotopic effect of precipitation needs to be better understood. The presence of high amounts of goethite, forams, and opal all caused a similar relative fractionation (+0.10‰ to +0.16‰), suggesting that even the less-reactive particles will preferentially have ^{56}Fe desorbed or dissolved from them in the presence of ligand. Some montmorillonite-like particles will have little net effect on the fractionation of the dissolved phase.

5.5 Conclusions

Inorganic particles fractionate the dissolved phase Fe, ranging from near 0‰ to +1.19‰. Ligands will preferentially dissolve ^{56}Fe and particles will absorb ^{54}Fe , leaving the dissolved phase enriched. Montmorillonite had little effect on the dissolved phase fractionation, even though it is high reactivity in the kinetic experiments. The fractionation in the presence of ferrihydrite was linear with particle concentration and had a slope of 0.0026‰/(mg/L). The ratio of dissolved FeDFB to particle concentration did not seem to have an appreciable effect on fractionation, only the ratio of Fe to DFB with excess ligand causes an additional fractionation of 0.3‰. The less-reactive particle types, goethite, opal, and forams, all had slightly enriched dissolved Fe, suggesting that a variety of particle interactions will leave a positive signature on the dissolved phase. Enriched open-ocean Fe profiles could be due to exchange with suspended or falling particulate matter.

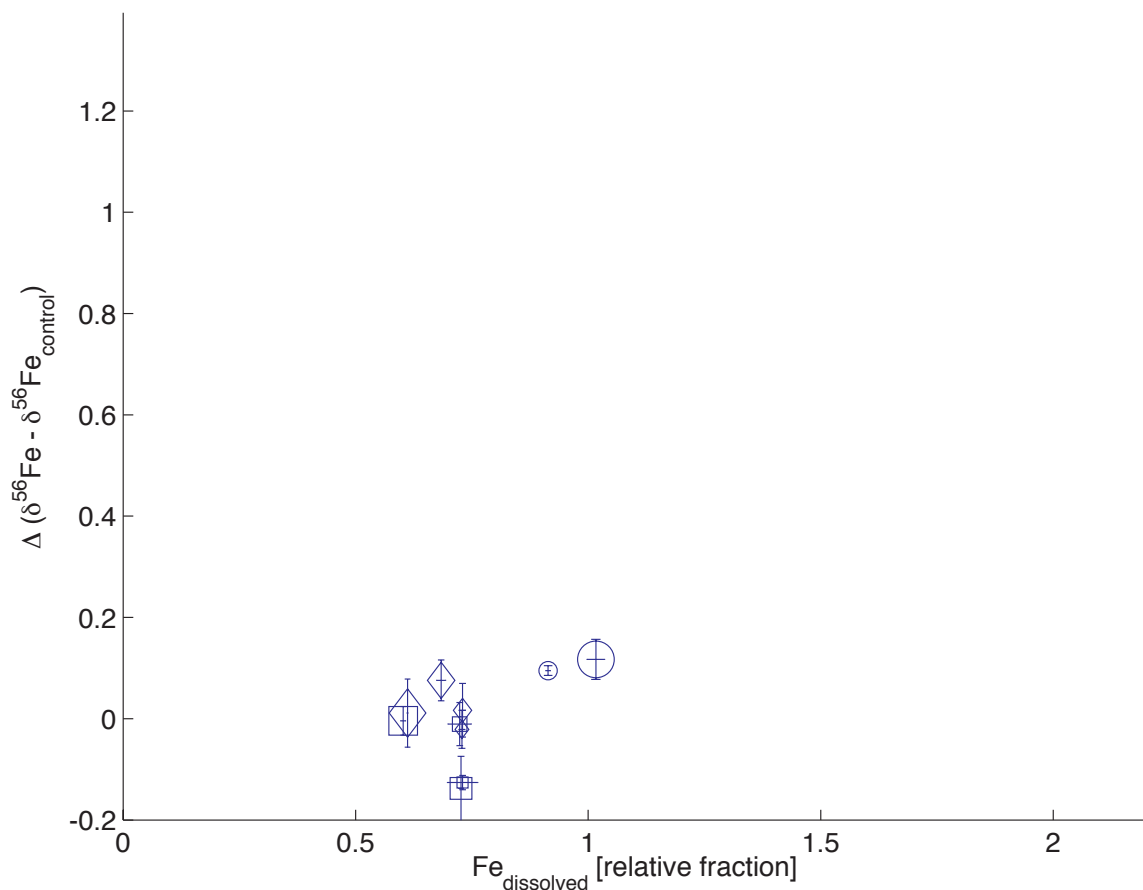


Figure 5.1. Fractionation of relative Fe dissolved ($[\text{Fe}]_{diss}$ at time of sampling/ $[\text{Fe}]_i$) in the presence of montmorillonite. \circ -400 nM Fe, 1000 nM DFB. \diamond -1000 nM Fe, 1000 nM DFB. \square -400 nM Fe, 400 nM DFB. Particle concentration increases with symbol size. $\Delta^{56}\text{Fe}$ has been corrected for the amount of fractionation caused in the presence of no particles (control) for each specific concentration and ratio of FeDFB. There is relatively little fractionation in the presence of montmorillonite, though the 400:1000 FeDFB experiments do have a higher average $\Delta^{56}\text{Fe}$ compared to the 1:1 FeDFB. Otherwise, there are no clear trends with particle concentration or with dissolved Fe.

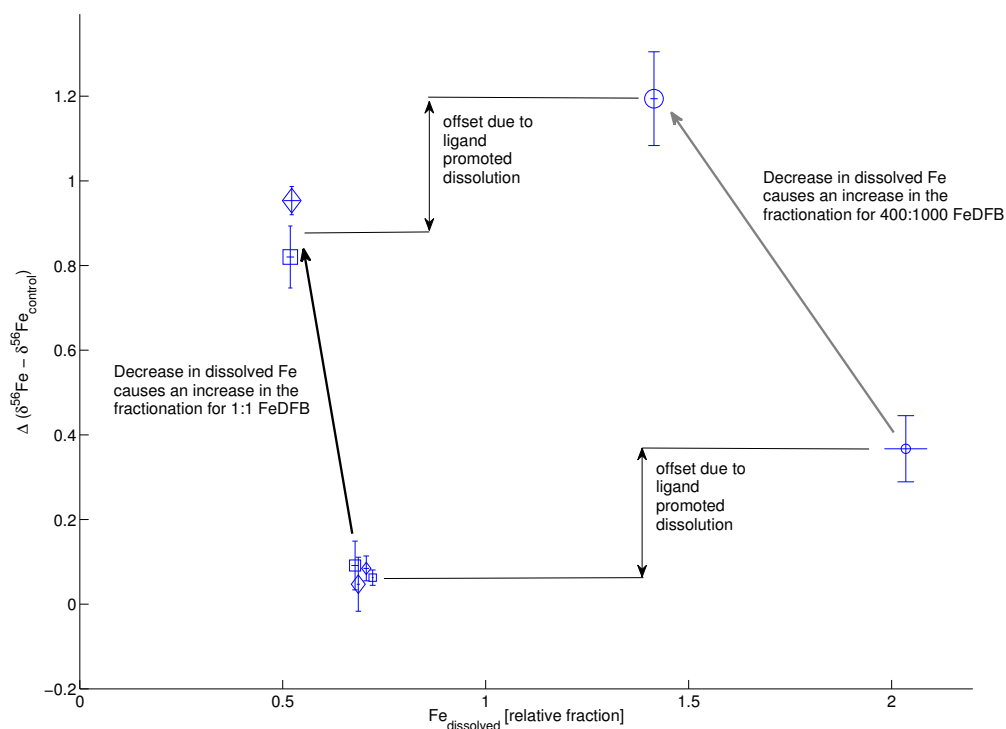


Figure 5.2. Fractionation of relative Fe dissolved ($[\text{Fe}]_{diss}$ at time of sampling/ $[\text{Fe}]_i$) in the presence of ferrihydrite. \circ -400 nM Fe, 1000 nM DFB. \diamond -1000 nM Fe, 1000 nM DFB. \square -400 nM Fe, 400 nM DFB. Particle concentration increases with symbol size. $\Delta^{56}\text{Fe}$ has been corrected for the amount of fractionation caused in the presence of no particles (control) for each specific concentration and ratio of FeDFB. The 1:1 ratio FeDFB data collapse to the same fractionation line (black, bold), indicating that concentration of dissolved Fe is not a factor in fractionation, unless there is excess ligand (grey, bold). The excess ligand-mediated-dissolution causes a constant fractionation of $+0.3\%$ from the 1:1 FeDFB data for the corresponding particle concentrations, indicated by the offset. The increased fractionation slopes, bold arrows, with the decreasing amount Fe dissolved in the presence of a higher ferrihydrite concentration suggests that there is some combination of light Fe removed and heavy Fe dissolved. However, these bold arrow slopes are different in the presence of varying ligand concentration. There is an indistinguishable difference in fractionation between the two lowest ferrihydrite concentrations.

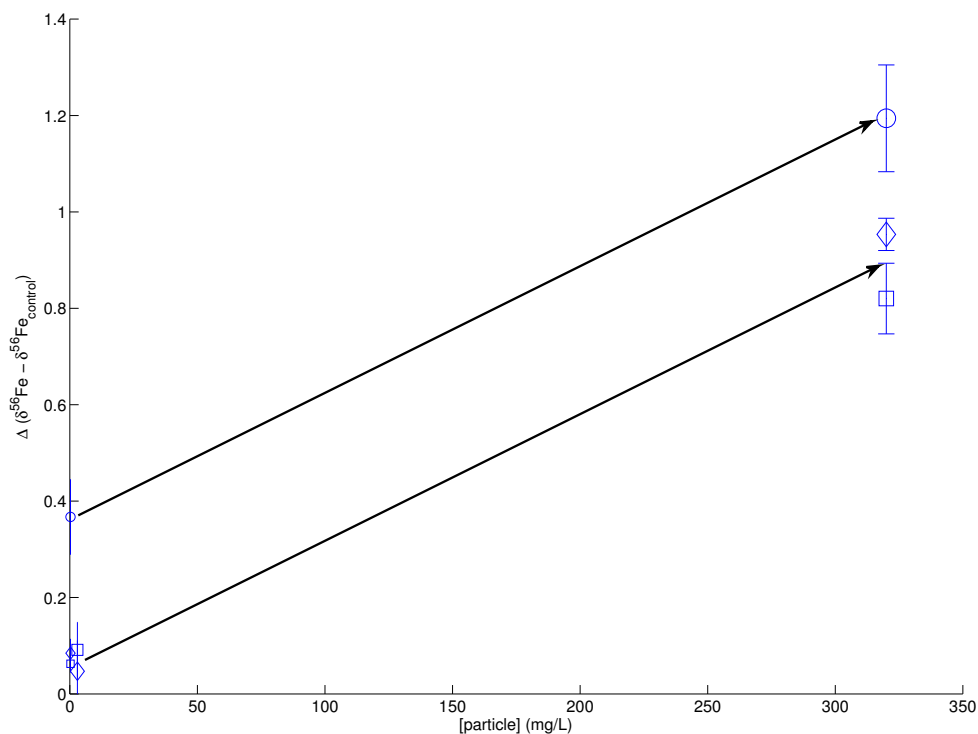


Figure 5.3. Fractionation versus ferrihydrate concentration. ○-400 nM Fe, 1000 nM DFB. ◇-1000 nM Fe, 1000 nM DFB. □-400 nM Fe, 400 nM DFB. Particle concentration increases with symbol size. $\Delta^{56}\text{Fe}$ has been corrected for the amount of fractionation caused in the presence of no particles (control) for each specific concentration and ratio of FeDFB. The fractionation slopes (arrows) are the same regardless of ligand concentration, indicating a possible first-order dependence on particle concentration. Additional particle concentration data and associated fractionations are needed to confirm this hypothesis.

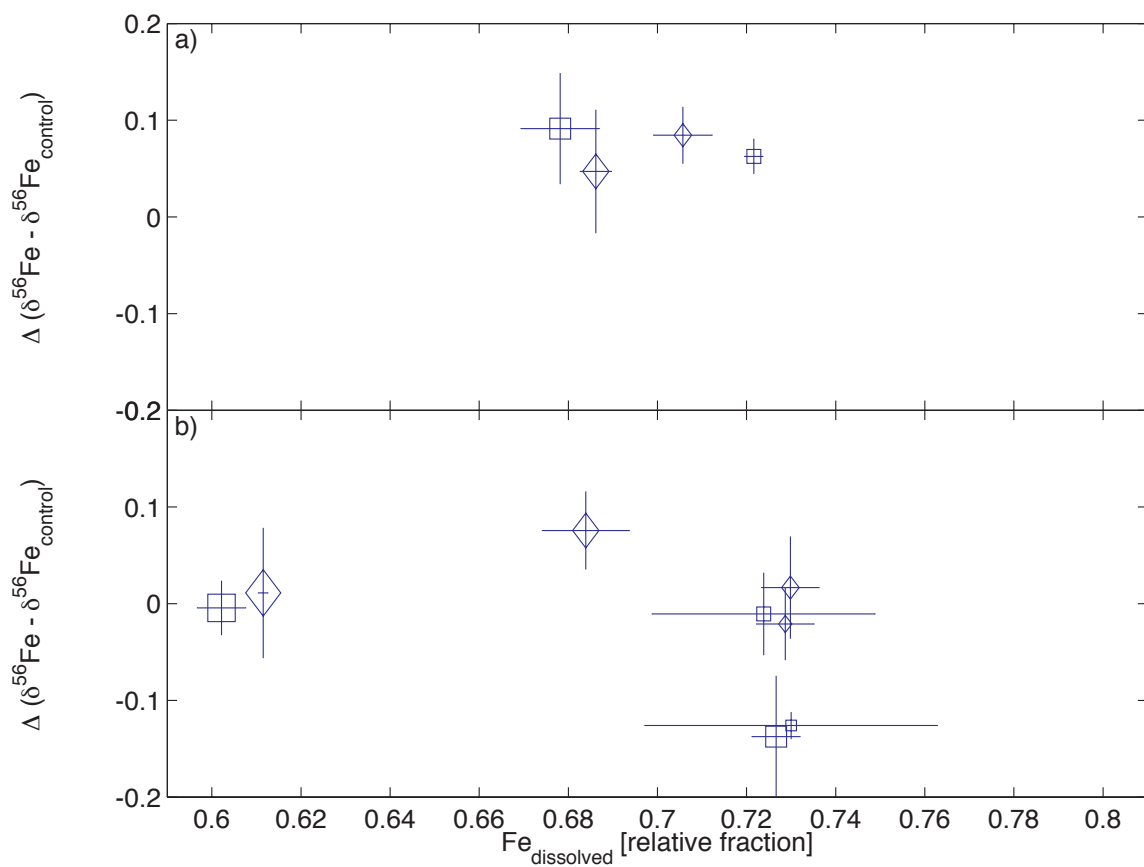


Figure 5.4. Detail of fractionation regions close to 0‰ for (a) ferrihydrite and (b) montmorillonite. Only 1:1 FeDFB samples are shown in this view. \diamond -1000 nM Fe, 1000 nM DFB. \square -400 nM Fe, 400 nM DFB. Particle concentration increases with symbol size. X- and y-axes are the same for each subplot. The overall conclusion is that fractionation is similar for 1:1 ratios of FeDFB and particle concentrations under 3 mg/L. A certain threshold particle concentration is needed to induce measurable fractionation.

Chapter 6

Conclusions

Our experimental setup allows us to track two separate pools of Fe (dissolved and particulate) using a less-abundant stable isotope tracer, ^{54}Fe , bound to a naturally occurring siderophore to elucidate the exchange rates and capacities of various marine particles.

For FeDFB experiments in the presence of ferrihydrite, there are large effects on dissolved $[\text{Fe}]$ due to adsorption of FeDFB onto the particles and dissolution of ferrihydrite itself. Even with Fe bound to siderophores, they cannot compete with fresh, labile iron oxides that have highly accessible surface area and reactive sites. Total FeDFB decreases over time, though a remarkable amount of ligand-mediated dissolution also takes place, which could be further investigated to determine the mechanism. The estimated parameter ranges for adsorption and dissolution are $(4 \pm 2) \times 10^{-4} \text{ (mg/L)}^{-1} \text{ day}^{-1}$ and $0.015 \pm 0.01 \text{ day}^{-1}$ based on ordinary differential equations modeling Fe exchange. This exchange capacity is important for fresh precipitates formed in the ocean. Even though Fe will precipitate when the dissolved phase becomes over-saturated, there is still exchange that transfers Fe from both phases to continue to alter the dissolve phase $[\text{Fe}]$.

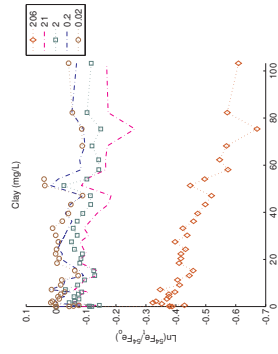
The notably absent reactivity of FeDFB with goethite, forams, and opal is striking compared to the varied absorptivity of ferrihydrite and montmorillonite. Montmorillonite absorbs Fe quickly and reaches a nearly instantaneous equilibrium. FeDFB is very stable in the presence of some particle types, but the absorptive capabilities of a fresh, labile iron oxide and a swelling clay can compete with ligand-bound Fe. These differences are due to the type of particle reaction sites and structure, including particle size fractions. Particle composition obviously has a varied effect on dissolved

Fe in the ocean, even in the presence siderophores.

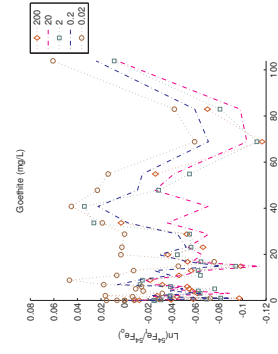
Inorganic particles fractionate the dissolved phase Fe, ranging from near 0 to +1.19‰. Ligands will preferentially dissolve ^{56}Fe and particles will absorb ^{54}Fe , leaving the dissolved phase enriched. Montmorillonite had little effect on the dissolved phase fractionation, even though it is high reactivity kinetically, meaning it is unbiased in its Fe uptake. The fractionation in the presence of ferrihydrite was linear with particle concentration and had a slope of $0.0026\text{‰}/(\text{mg/L})$. The ratio of dissolved Fe/DFB to particle concentration did not seem to have an appreciable effect on fractionation, though the ratio of Fe to DFB caused a fractionation of 0.3‰ in the presence of excess ligand.. The less reactive particle types, goethite, opal, and forams, all had slightly enriched dissolved Fe. The overall positive fractionation of the dissolved phase Fe in the presence of various particles suggests that enriched open ocean Fe profiles, like the BATS, could be due to exchange with suspended and falling particulate matter.

An optimal model would incorporate particle composition and corresponding exchange rates to show how dissolved Fe and isotopic composition would change as particles fall through the water column or as water masses circulate.

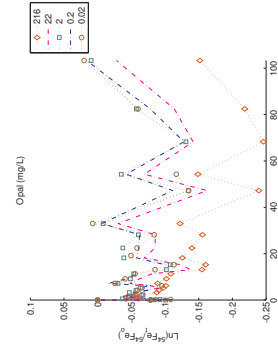
Appendix A
Natural Log Plots of Data from Chapter 4



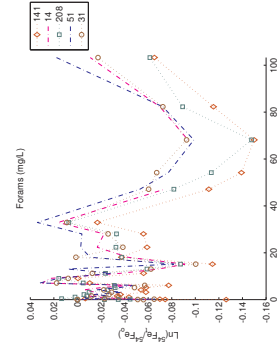
(a) Clay ⁵⁴Fe



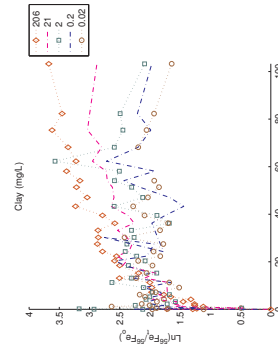
(b) Goethite ⁵⁴Fe



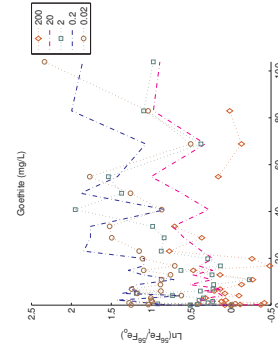
(c) Opal ⁵⁴Fe



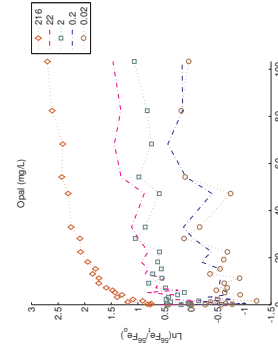
(d) Forams ⁵⁴Fe



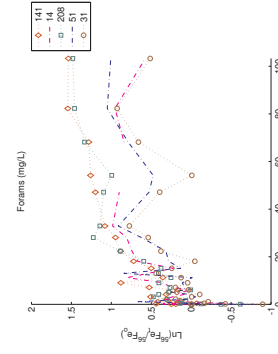
(e) Clay ⁵⁶Fe



(f) Goethite ⁵⁶Fe



(g) Opal ⁵⁶Fe



(h) Forams ⁵⁶Fe

Bibliography

- [1] J. H. Martin and R. M. Gordon, “Northeast Pacific iron distributions in relation to phytoplankton productivity.” *Deep-Sea Res.*, vol. 35, pp. 177–196, 1988. [1](#)
- [2] J. H. Martin, R. M. Gordon, S. Fitzwater, and W. W. Broenkow, “VERTEX: phytoplankton/iron studies in the Gulf of Alaska.” *Deep-Sea Res.*, vol. 36, pp. 649–680, 1989. [1](#)
- [3] J. Martin, R. Gordon, and S. Fitzwater, “The Case for Iron,” *Limnology and Oceanography*, vol. 36, no. 8, pp. 1793–1802, 1991. [Online]. Available: <http://www.jstor.org/stable/2837715> [1](#)
- [4] K. Bruland, K. Orians, and J. Cowen, “Reactive trace metals in the stratified central North Pacific,” *Geochimica et Cosmochimica Acta*, vol. 58, no. 15, pp. 3171–3182, Aug. 1994. [Online]. Available: <http://linkinghub.elsevier.com/retrieve/pii/0016703794900442> [1](#)
- [5] F.-x. Fu and P. R. Bell, “Growth, N₂ fixation and photosynthesis in a cyanobacterium, *Trichodesmium* sp., under Fe stress.” *Biotechnology letters*, vol. 25, no. 8, pp. 645–9, Apr. 2003. [Online]. Available: <http://www.ncbi.nlm.nih.gov/pubmed/12882160> [1](#)
- [6] H. W. Paerl, L. E. Prufertbebout, and C. Z. Guo, “IRON-STIMULATED N-2 FIXATION AND GROWTH IN NATURAL AND CULTURED POPULATIONS OF THE PLANKTONIC MARINE CYANOBACTERIA TRICHODESMIUM SPP,” *Applied and Environmental Microbiology*, vol. 60, no. 3, pp. 1044–1047, 1994. [Online]. Available: <GotoISI://A1994MZ13700044> [1](#)
- [7] J. Wu, W. Sunda, E. a. Boyle, and D. M. Karl, “Phosphate depletion in the western North Atlantic Ocean.” *Science (New York, N.Y.)*, vol. 289, no. 5480, pp. 759–62, Aug. 2000. [Online]. Available: <http://www.ncbi.nlm.nih.gov/pubmed/10926534> [1](#)
- [8] M. M. Mills, C. Ridame, M. Davey, J. La Roche, and R. J. Geider, “Iron and phosphorus co-limit nitrogen fixation in the eastern tropical North Atlantic,” *Nature*, vol. 429, no. 6989, pp. 292–294, 2004. [Online]. Available: <GotoISI://000221505900041> [1](#), [3](#)
- [9] R. A. Duce and N. W. Tindale, “Atmospheric transport of iron and its deposition in the Ocean,” *Limnology and Oceanography*, vol. 36, no. 8,

- pp. 1715–1726, 1991. [Online]. Available: <http://www.jstor.org/stable/2837709> [\(GotoISI\)://A1991HR98100016](#) **1, 2, 73**
- [10] C. I. Measures, M. T. Brown, and S. Vink, “Dust deposition to the surface waters of the western and central North Pacific inferred from surface water dissolved aluminum concentrations,” *Geochemistry Geophysics Geosystems*, vol. 6, no. 9, p. Q09M03, 2005. [Online]. Available: <http://www.agu.org/pubs/crossref/2005.../2005GC000922.shtml> **2**
- [11] J. H. Martin, “Glacial-interglacial CO₂ change: The iron hypothesis,” *Paleoceanography*, vol. 5, pp. 1–13, 1990. **2**
- [12] K. H. Coale, K. S. Johnson, S. E. Fitzwater, R. M. Gordon, S. Tanner, F. P. Chavez, L. Ferioli, C. Sakamoto, P. Rogers, F. Millero, P. Steinberg, P. Nightingale, D. Cooper, W. P. Cochlan, M. R. Landry, J. Constantinou, G. Rollwagen, A. Trasvina, and R. Kudela, “A massive phytoplankton bloom induced by an ecosystem-scale iron fertilization experiment in the equatorial Pacific Ocean,” *Nature*, vol. 383, no. 6600, pp. 495–501, 1996. [Online]. Available: [\(GotoISI\)://A1996VL75500041](#) **3**
- [13] J. H. Martin, K. H. Coale, K. S. Johnson, S. E. Fitzwater, R. M. Gordon, S. J. Tanner, C. N. Hunter, V. A. Elrod, J. L. Nowicki, T. L. Coley, R. T. Barber, S. Lindley, A. J. Watson, K. Vanscoy, C. S. Law, M. I. Liddicoat, R. Ling, T. Stanton, J. Stockel, C. Collins, A. Anderson, R. Bidigare, M. Ondrusek, M. Latasa, F. J. Millero, K. Lee, W. Yao, J. Z. Zhang, G. Friederich, C. Sakamoto, F. Chavez, K. Buck, Z. Kolber, R. Greene, P. Falkowski, S. W. Chisholm, F. Hoge, R. Swift, J. Yungel, S. Turner, P. Nightingale, A. Hatton, P. Liss, and N. W. Tindale, “TESTING THE IRON HYPOTHESIS IN ECOSYSTEMS OF THE EQUATORIAL PACIFIC-OCEAN,” *Nature*, vol. 371, no. 6493, pp. 123–129, 1994. [Online]. Available: [\(GotoISI\)://A1994PF19100054](#) **3**
- [14] P. W. Boyd, A. J. Watson, C. S. Law, E. R. Abraham, T. Trull, R. Murdoch, D. C. E. Bakker, A. R. Bowie, K. O. Buesseler, H. Chang, M. Charette, P. Croot, K. Downing, R. Frew, M. Gall, M. Hadfield, J. Hall, M. Harvey, G. Jameson, J. LaRoche, M. Liddicoat, R. Ling, M. T. Maldonado, R. M. McKay, S. Nodder, S. Pickmere, R. Pridmore, S. Rintoul, K. Safi, P. Sutton, R. Strzeppek, K. Tanneberger, S. Turner, A. Waite, and J. Zeldis, “A mesoscale phytoplankton bloom in the polar Southern Ocean stimulated by iron fertilization,” *NATURE*, vol. 407, no. 6805, pp. 695–702, Oct. 2000. **3, 4**
- [15] P. W. Boyd, T. Jickells, C. S. Law, S. Blain, E. A. Boyle, K. O. Buesseler, K. H. Coale, J. J. Cullen, H. J. W. de Baar, M. Follows, M. Harvey, C. Lancelot, M. Lasseuseur, N. P. J. Owens, R. Pollard, R. B. Rivkin, J. Sarmiento, V. Schoemann, V. Smetacek, S. Takeda, A. Tsuda, S. Turner, and A. J. Watson, “Mesoscale iron enrichment experiments 1993–2005: Synthesis and future directions,” *Science*, vol. 315, no. 5812, pp. 612–617, 2007. [Online]. Available: [\(GotoISI\)://000243909400033](#) **3**

- [16] F. Millero and S. Sotolongo, "The oxidation of Fe(II) with H₂O₂ in seawater," *Geochimica et Cosmochimica Acta*, vol. 53, no. 8, pp. 1867–1873, Aug. 1989. [Online]. Available: <http://linkinghub.elsevier.com/retrieve/pii/0016703789903074> 3
- [17] K. Yokoi and C. van den Berg, "The determination of iron in seawater using catalytic cathodic stripping voltammetry," *Electroanalysis*, vol. 4, no. 1, pp. 65–69, Jan. 1992. [Online]. Available: <http://onlinelibrary.wiley.com/doi/10.1002/elan.1140040113/abstract> 3
- [18] E. Rue and K. Bruland, "Complexation of iron(III) by natural organic ligands in the Central North Pacific as determined by a new competitive ligand equilibration/adsorptive cathodic stripping voltammetric method," *Marine Chemistry*, vol. 50, no. 1-4, pp. 117–138, Aug. 1995. [Online]. Available: <http://linkinghub.elsevier.com/retrieve/pii/030442039500031L> 3
- [19] E. L. Rue and K. W. Bruland, "The role of organic complexation on ambient iron chemistry in the equatorial Pacific Ocean and the response of a mesoscale iron addition experiment," *Limnology and Oceanography*, vol. 42, no. 5, pp. 901–910, 1997. [Online]. Available: http://www.aslo.org/lo/toc/vol_42/issue_5/0901.html 4
- [20] D. A. Hutchins, A. E. Witter, A. Butler, and G. W. L. Iii, "letters to nature Competition among marine phytoplankton for different chelated iron species," *Nature*, vol. 400, no. AUGUST, pp. 858–861, 1999. 4, 6
- [21] M. Wells, "Manipulating iron availability in nearshore waters," *Limnology and oceanography*, vol. 44, no. 4, pp. 1002–1008, 1999. [Online]. Available: <http://www.jstor.org/stable/2670755> 4
- [22] M. Wells, N. Price, and K. Bruland, "Iron Limitation and the Cyanobacterium *Synechococcus* in Equatorial Pacific Waters," *Limnology and oceanography*, vol. 39, no. 6, pp. 1481–1486, 1994. [Online]. Available: <http://www.jstor.org/stable/2838148> 4, 6
- [23] M. L. Wells and C. G. Trick, "Controlling iron availability to phytoplankton in iron-replete coastal waters," *Marine Chemistry*, vol. 86, no. 1-2, pp. 1–13, Apr. 2004. [Online]. Available: <http://linkinghub.elsevier.com/retrieve/pii/S0304420303001907> 4
- [24] K. Barbeau, E. L. Rue, K. W. Bruland, and A. Butler, "Photochemical cycling of iron in the surface ocean mediated by microbial iron(III)-binding ligands," *Nature*, vol. 413, no. 6854, pp. 409–413, Sep. 2001. [Online]. Available: [http://www.ncbi.nlm.nih.gov/pubmed/11574885\(GotoISI\):/000171188700051](http://www.ncbi.nlm.nih.gov/pubmed/11574885(GotoISI):/000171188700051) 4
- [25] K. Barbeau, E. L. Rue, C. G. Trick, K. W. Bruland, and A. Butler, "Photochemical reactivity of siderophores produced by marine heterotrophic bacteria and cyanobacteria, based on characteristic Fe(III) binding groups," *Limnology and Oceanography*, vol. 48, no. 3, pp. 1069–1078, 2003. [Online]. Available: http://www.aslo.org/lo/toc/vol_48/issue_3/1069.html 4

- [26] S. E. Vartivarian and R. E. Cowart, “Extracellular iron reductases: identification of a new class of enzymes by siderophore-producing microorganisms.” *Archives of biochemistry and biophysics*, vol. 364, no. 1, pp. 75–82, Apr. 1999. [Online]. Available: <http://www.ncbi.nlm.nih.gov/pubmed/10087167> 4
- [27] M. T. Maldonado and N. M. Price, “Reduction and Transport of Organically Bound Iron By *Thalassiosira Oceanica* (Bacillariophyceae),” *Journal of Phycology*, vol. 37, no. 2, pp. 298–310, Apr. 2001. [Online]. Available: <http://doi.wiley.com/10.1046/j.1529-8817.2001.037002298.x> 4
- [28] P. Santschi, “Particle flux and trace metal residence time in natural waters,” *Limnology and Oceanography*, vol. 29, no. 5, pp. 1100–1108, 1984. [Online]. Available: <http://www.jstor.org/pss/2836435http://openagricola.nal.usda.gov/Record/IND85012758> 5, 38
- [29] B. D. Honeyman and P. H. Santschi, “Metals in aquatic systems,” *Environmental Science & Technology*, vol. 22, no. 8, pp. 862–871, Aug. 1988. [Online]. Available: <http://pubs.acs.org/doi/abs/10.1021/es00173a002> 5, 6, 94
- [30] M. P. Bacon and R. F. Anderson, “Distribution of Thorium isotopes between dissolved and particulate forms in the deep sea.” *Journal of Geophysical Research*, vol. 87, pp. 2045–2056, 1982. 5
- [31] K. H. Coale and K. W. Bruland, “TH-234 - U-238 DISEQUILIBRIA WITHIN THE CALIFORNIA CURRENT,” *Limnology and Oceanography*, vol. 30, no. 1, pp. 22–33, 1985. [Online]. Available: [GotoISI://A1985ACJ5400002](http://www.jstor.org/pss/2836435http://openagricola.nal.usda.gov/Record/IND85012758) 5
- [32] R. F. Anderson, M. P. Bacon, and P. G. Brewer, “Removal of Th-230 and Pa-231 at ocean margins.” *Earth and Planetary Science Letters*, vol. 66, pp. 73–90, 1983. 5
- [33] —, “Removal of Th-230 and Pa-231 from the open ocean,” *Earth and Planetary Science Letters*, vol. 62, pp. 7–23, 1983. 5
- [34] M. P. Bacon, C.-a. Huh, A. P. Fleer, and W. G. Deuser, “Seasonality in the flux of natural radionuclides and plutonium in the deep Sargasso Sea,” *Deep-Sea Research*, vol. 32, pp. 273–286, 1985. 5
- [35] K. O. Buesseler, “Do upper-ocean sediment traps provide an accurate record of particle flux?” *Nature*, vol. 353, pp. 420–423, 1991. 5
- [36] K. O. Buesseler, A. F. Michaels, D. A. Siegel, and A. H. Knap, “A 3-DIMENSIONAL TIME-DEPENDENT APPROACH TO CALIBRATING SEDIMENT TRAP FLUXES,” *Global Biogeochemical Cycles*, vol. 8, no. 2, pp. 179–193, 1994. [Online]. Available: [GotoISI://A1994NQ41000007](http://www.jstor.org/pss/2836435http://openagricola.nal.usda.gov/Record/IND85012758) 5
- [37] J. F. McManus, R. Francois, J. M. Gherardi, L. D. Keigwin, and S. Brown-Leger, “Collapse and rapid resumption of Atlantic meridional circulation linked to deglacial climate changes.” *Nature*, vol. 428, pp. 834–837, 2004. 5
- [38] E. Yu, R. Francois, and M. Bacon, “Similar rates of modern and last-glacial ocean thermohaline circulation inferred from radiochemical data,” *Nature*,

- vol. 379, no. 6567, pp. 689–694, 1996. [Online]. Available: <http://www.ldeo.columbia.edu/~peter/Resources/Seminar/readings/Yuetal.1996.pdf> 5
- [39] J. K. B. Bishop, D. R. Ketten, and J. M. Edmond, “CHEMISTRY, BIOLOGY AND VERTICAL FLUX OF PARTICULATE MATTER FROM THE UPPER 400M OF THE CAPE BASIN IN THE SOUTHEAST ATLANTIC OCEAN,” *Deep-Sea Research*, vol. 25, no. 12, pp. 1121–1161, 1978. [Online]. Available: GotoISI://A1978GG30200001 5
- [40] K. O. Buesseler, A. N. Antia, M. Chen, S. W. Fowler, W. D. Gardner, O. Gustafsson, K. Harada, A. F. Michaels, M. R. van der Loeff'o, M. Sarin, D. K. Steinberg, and T. Trull, “An assessment of the use of sediment traps for estimating upper ocean particle fluxes,” *Journal of Marine Research*, vol. 65, no. 3, pp. 345–416, 2007. [Online]. Available: GotoISI://000248890500002 5
- [41] K. O. Buesseler, T. W. Trull, D. K. Steinber, M. W. Silver, D. A. Siegel, S. I. Saitoh, C. H. Lamborg, P. J. Lam, D. M. Karl, N. Z. Jiao, M. C. Honda, M. Elskens, F. Dehairs, S. L. Brown, P. W. Boyd, J. K. B. Bishop, and R. R. Bidigare, “VERTIGO (VERTical Transport in the Global Ocean): A study of particle sources and flux attenuation in the North Pacific,” *Deep-Sea Research Part Ii-Topical Studies in Oceanography*, vol. 55, no. 14-15, pp. 1522–1539, 2008. [Online]. Available: GotoISI://000259409900002 5
- [42] T. Cheng, D. E. Hammond, W. M. Berelson, J. G. Hering, and S. Dixit, “Dissolution kinetics of biogenic silica collected from the water column and sediments of three Southern California borderland basins,” *Marine chemistry*, vol. 113, no. 1-2, pp. 41–49, 2009. [Online]. Available: GotoISI://000264652400005 5
- [43] C. De La Rocha and U. Passow, “Factors influencing the sinking of POC and the efficiency of the biological carbon pump,” *Deep Sea Research Part II: Topical Studies in Oceanography*, vol. 54, no. 5-7, pp. 639–658, Mar. 2007. [Online]. Available: <http://www.sciencedirect.com/science/article/pii/S0967064507000392> 5
- [44] R. M. Gordon, K. S. Johnson, and K. H. Coale, “The behaviour of iron and other trace elements during the IronEx-I and PlumEx experiments in the Equatorial Pacific,” *Deep-Sea Research Part Ii-Topical Studies in Oceanography*, vol. 45, no. 6, pp. 995–1041, 1998. [Online]. Available: GotoISI://000076946500005 5
- [45] S. Huang and M. H. Conte, “Source/process apportionment of major and trace elements in sinking particles in the Sargasso sea,” *Geochimica Et Cosmochimica Acta*, vol. 73, no. 1, pp. 65–90, 2009. [Online]. Available: GotoISI://000261914500005 5
- [46] G. A. Knauer, D. M. Karl, J. H. Martin, and C. N. Hunter, “INSITU EFFECTS OF SELECTED PRESERVATIVES ON TOTAL CARBON, NITROGEN AND METALS COLLECTED IN SEDIMENT TRAPS,” *Journal*

- of Marine Research*, vol. 42, no. 2, pp. 445–462, 1984. [Online]. Available: [⟨GotoISI⟩://A1984SS86200008](http://www.sciencedirect.com/science/article/pii/S0967063798000594) 5
- [47] J. Kuss and K. Kremling, “Particulate trace element fluxes in the deep northeast Atlantic Ocean,” *Deep-Sea Research Part I*, vol. 46, no. 1, pp. 149–169, 1999. [Online]. Available: <http://www.sciencedirect.com/science/article/pii/S0967063798000594> 5
- [48] C. Pohl, A. Löffler, and U. Hennings, “A sediment trap flux study for trace metals under seasonal aspects in the stratified Baltic Sea (Gotland Basin; 57 degrees 19.20 ' N; 20 degrees 03.00 ' E),” *Marine chemistry*, vol. 84, no. 3-4, pp. 143–160, 2004. [Online]. Available: [⟨GotoISI⟩://000187751200001](http://www.sciencedirect.com/science/article/pii/S0304420304001120) 5
- [49] A. Turner and G. Millward, “Suspended Particles: Their Role in Estuarine Biogeochemical Cycles,” *Estuarine, Coastal and Shelf Science*, vol. 55, no. 6, pp. 857–883, Dec. 2002. [Online]. Available: <http://linkinghub.elsevier.com/retrieve/pii/S0272771402910334> 5, 6
- [50] S. E. Weinstein and S. B. Moran, “Vertical flux of particulate Al, Fe, Pb, and Ba from the upper ocean estimated from Th-234/U-238 disequilibria,” *Deep-Sea Research Part I-Oceanographic Research Papers*, vol. 52, no. 8, pp. 1477–1488, 2005. [Online]. Available: [⟨GotoISI⟩://000231249100008](http://www.sciencedirect.com/science/article/pii/S0304420305001120) 5
- [51] A. B. Burd, G. A. Jackson, and S. B. Moran, “The role of the particle size spectrum in estimating POC fluxes from Th-234/U-238 disequilibrium,” *Deep-Sea Research Part I-Oceanographic Research Papers*, vol. 54, no. 6, pp. 897–918, 2007. [Online]. Available: [⟨GotoISI⟩://000247715600004](http://www.sciencedirect.com/science/article/pii/S0304420307001120) 5
- [52] M. P. Hurst and K. W. Bruland, “An investigation into the exchange of iron and zinc between soluble, colloidal, and particulate size-fractions in shelf waters using low-abundance isotopes as tracers in shipboard incubation experiments,” *Marine chemistry*, vol. 103, no. 3-4, pp. 211–226, 2007. [Online]. Available: [⟨GotoISI⟩://000244392000001](http://www.sciencedirect.com/science/article/pii/S0304420307001120) 5
- [53] K. J. Farley and F. M. M. Morel, “Role of coagulation in the kinetics of sedimentation,” *Environmental Science & Technology*, vol. 20, no. 2, pp. 187–195, Feb. 1986. [Online]. Available: <http://pubs.acs.org/doi/abs/10.1021/es00144a014> 5
- [54] B. D. Honeyman and P. H. Santschi, “A BROWNIAN-PUMPING MODEL FOR OCEANIC TRACE-METAL SCAVENGING - EVIDENCE FROM TH-ISOTOPES,” *Journal of Marine Research*, vol. 47, no. 4, pp. 951–992, 1989. [Online]. Available: [⟨GotoISI⟩://A1989CK55000011](http://www.sciencedirect.com/science/article/pii/S0304420389001120) 5, 55
- [55] —, “Coupling adsorption and particle aggregation: laboratory studies of ”colloidal pumping” using iron-59-labeled hematite,” *Environmental Science & Technology*, vol. 25, no. 10, pp. 1739–1747, Oct. 1991. [Online]. Available: <http://pubs.acs.org/doi/abs/10.1021/es00022a010> 5, 55, 94, 96, 97
- [56] M. C. Stordal, P. H. Santschi, and G. A. Gill, “Colloidal pumping: Evidence for the coagulation process using natural colloids tagged with Hg-203,”

- Environmental Science & Technology*, vol. 30, no. 11, pp. 3335–3340, 1996. [Online]. Available: [〈GotoISI〉://A1996VR63100051](#) 5
- [57] L. S. Wen, P. Santschi, G. Gill, and C. Paternostro, “Estuarine trace metal distributions in Galveston Bay: importance of colloidal forms in the speciation of the dissolved phase,” *Marine chemistry*, vol. 63, no. 3-4, pp. 185–212, 1999. [Online]. Available: [〈GotoISI〉://000081358000001](#) 5
- [58] J. Wu, E. Boyle, W. Sunda, and L. S. Wen, “Soluble and colloidal iron in the oligotrophic North Atlantic and North Pacific.” *Science (New York, N.Y.)*, vol. 293, no. 5531, pp. 847–9, Aug. 2001. [Online]. Available: <http://www.ncbi.nlm.nih.gov/pubmed/11486084> 5, 6
- [59] J. M. Garnier, M. K. Pham, P. Ciffroy, and J. M. Martin, “Kinetics of trace element complexation with suspended matter and with filterable ligands in freshwater,” *Environmental Science & Technology*, vol. 31, no. 6, pp. 1597–1606, 1997. [Online]. Available: [〈GotoISI〉://A1997XB62000022](#) 6
- [60] L. Wen, P. Santschi, and D. Tang, “Interactions between radioactively labeled colloids and natural particles: Evidence for colloidal pumping,” *Geochimica et cosmochimica acta*, vol. 61, no. 14, pp. 2867–2878, 1997. [Online]. Available: <http://linkinghub.elsevier.com/retrieve/pii/S0016703797001397> 6, 73
- [61] C. S. Hassler and V. Schoemann, “Bioavailability of organically bound Fe to model phytoplankton of the Southern Ocean,” *Biogeosciences*, vol. 6, no. 10, pp. 2281–2296, Oct. 2009. [Online]. Available: <http://www.biogeosciences.net/6/2281/2009/> 6
- [62] M. T. Maldonado, “Acquisition of iron bound to strong organic complexes, with different Fe binding groups and photochemical reactivities, by plankton communities in Fe-limited subantarctic waters,” *Global Biogeochemical Cycles*, vol. 19, no. 4, 2005. [Online]. Available: <http://www.agu.org/pubs/crossref/2005/2005GB002481.shtml> 6
- [63] H. W. Rich and F. M. M. Morel, “Availability of well-defined iron colloids to the marine diatom *Thalassiosira weissflogii*,” *Limnology and Oceanography*, vol. 35, no. 3, pp. 652–662, 1990. [Online]. Available: http://www.aslo.org/lo/toc/vol_35/issue_3/0652.html 6
- [64] L. M. Nodwell and N. M. Price, “Direct use of inorganic colloidal iron by marine mixotrophic phytoplankton,” *Limnology and Oceanography*, vol. 46, no. 4, pp. 765–777, 2001. [Online]. Available: http://www.aslo.org/lo/toc/vol_46/issue_4/0765.html 6
- [65] M. Chen, R. Dei, W. Wang, and L. Guo, “Marine diatom uptake of iron bound with natural colloids of different origins,” *Marine chemistry*, vol. 81, no. 3-4, pp. 177–189, Apr. 2003. [Online]. Available: <http://linkinghub.elsevier.com/retrieve/pii/S030442030300032X> 6
- [66] W. C. Zhang and W. X. Wang, “Colloidal organic carbon and trace metal (Cd, Fe, and Zn) releases by diatom exudation and copepod grazing,” *JOURNAL*

OF EXPERIMENTAL MARINE BIOLOGY AND ECOLOGY, vol. 307, no. 1, pp. 17–34, Aug. 2004. 6

- [67] V. Hatje, T. Payne, D. Hill, G. McOrist, G. Birch, and R. Szymczak, “Kinetics of trace element uptake and release by particles in estuarine waters: effects of pH, salinity, and particle loading,” *Environment international*, vol. 29, no. 5, pp. 619–629, 2003. [Online]. Available: <http://linkinghub.elsevier.com/retrieve/pii/S0160412003000497> 6, 7
- [68] Y. Li, L. Burkhardt, M. Buchholtz, P. Ohara, and P. Santschi, “Partition of radiotracers between suspended particles and seawater,” *Geochimica et Cosmochimica Acta*, vol. 48, no. 10, pp. 2011–2019, Oct. 1984. [Online]. Available: <http://linkinghub.elsevier.com/retrieve/pii/001670378490382X> 6, 38, 72, 96, 97
- [69] U. Nyffeler, Y. Li, and P. Santschi, “A kinetic approach to describe trace-element distribution between particles and solution in natural aquatic systems,” *Geochimica et Cosmochimica Acta*, vol. 48, no. 7, pp. 1513–1522, Jul. 1984. [Online]. Available: <http://linkinghub.elsevier.com/retrieve/pii/0016703784904071> 6, 38, 73
- [70] Z. Chase, R. F. Anderson, M. Q. Fleisher, and P. W. Kubik, “The influence of particle composition and particle flux on scavenging of Th, Pa and Be in the ocean,” *Earth and Planetary Science Letters*, vol. 204, no. 1-2, pp. 215–229, Nov. 2002. [Online]. Available: <http://linkinghub.elsevier.com/retrieve/pii/S0012821X02009846> 6
- [71] S. Luo and T.-L. Ku, “Oceanic $^{231}\text{Pa}/^{230}\text{Th}$ ratio influenced by particle composition and remineralization,” *Earth and Planetary Science Letters*, vol. 167, no. 3-4, pp. 183–195, Apr. 1999. [Online]. Available: <http://linkinghub.elsevier.com/retrieve/pii/S0012821X99000357> 6
- [72] M. Roy-Barman, C. Jeandel, M. Souhaut, M. R. van der Loeff, I. Voegelé, N. Leblond, and R. Freydier, “The influence of particle composition on thorium scavenging in the NE Atlantic ocean (POMME experiment),” *Earth and Planetary Science Letters*, vol. 240, no. 3-4, pp. 681–693, 2005. [Online]. Available: <http://linkinghub.elsevier.com/retrieve/pii/S0012821X05000011> 6
- [73] M. Roy-Barman, C. Lemaitre, S. Ayrault, C. Jeandel, M. Souhaut, and J. C. Miquel, “The influence of particle composition on Thorium scavenging in the Mediterranean Sea,” *Earth and Planetary Science Letters*, vol. 286, no. 3-4, pp. 526–534, 2009. [Online]. Available: <http://linkinghub.elsevier.com/retrieve/pii/S0012821X09000018> 6
- [74] H. J. Walter, M. M. Rutgers van der Loeff, and H. Hoeltzen, “Enhanced scavenging of Pa-231 relative to Th-230 in the South Atlantic south of the Polar Front: Implications for the use of the Pa-231/Th-230 ratio a paleoproductivity proxy,” *Earth and Planetary Science Letters*, vol. 149, pp. 85–100, 1997. 6
- [75] H. J. Walter, W. Geibert, M. M. R. van der Loeff, G. Fischer, and U. Bathmann, “Shallow vs. deep-water scavenging of Pa-231 and Th-230 in radionuclide enriched waters of the Atlantic sector of the Southern Ocean,”

- Deep-Sea Research Part I-Oceanographic Research Papers*, vol. 48, no. 2, pp. 471–493, 2001. [Online]. Available: [〈GotoISI〉://000165362800006](#) 6
- [76] L. D. Guo, M. Chen, and C. Gueguen, “Control of Pa/Th ratio by particulate chemical composition in the ocean,” *Geophysical Research Letters*, vol. 29, no. 20, 2002. [Online]. Available: [〈GotoISI〉://000180607700022](#) 6
- [77] E. A. Boyle, “Cadmium, zinc, copper, and barium in foraminifera tests,” *Earth and Planetary Science Letters*, vol. 53, pp. 11–35, 1981. 7
- [78] —, “Vertical oceanic nutrient fractionation and glacial/interglacial CO₂ cycles,” *Nature*, vol. 331, pp. 55–56, 1988. 7
- [79] —, “Cadmium and d13C paleochemical ocean distributions during the stage 2 glacial maximum,” *Annual Reveiw of Earth and Planetary Sciences*, vol. 20, pp. 245–287, 1992. 7
- [80] K. Hester and E. Boyle, “Water chemistry control of the Cd content of benthic foraminifera,” *Nature*, vol. 298, pp. 260–261, 1982. 7
- [81] H. Elderfield and R. Rickaby, “Oceanic Cd/P ratio and nutrient utilization in the glacial Southern Ocean,” *Nature*, vol. 405, no. 6784, pp. 305–310, May 2000. [Online]. Available: <http://www.ncbi.nlm.nih.gov/pubmed/10830952> 7
- [82] W. Geibert and R. Usbeck, “Adsorption of thorium and protactinium onto different particle types: Experimental findings,” *Geochimica Et Cosmochimica Acta*, vol. 68, no. 7, pp. 1489–1501, 2004. [Online]. Available: [〈GotoISI〉://000220470900004](#) 7
- [83] Y. Y. Zhang, E. R. Zhang, and J. Zhang, “Modeling on adsorption-desorption of trace metals to suspended particle matter in the Changjiang Estuary,” *Environmental geology*, vol. 53, no. 8, pp. 1751–1766, 2008. [Online]. Available: [〈GotoISI〉://000252798500014](#) 7
- [84] F. M. M. Morel, J. G. Rueter, D. M. Anderson, and R. R. L. Guillard, “AQUIL - CHEMICALLY DEFINED PHYTOPLANKTON CULTURE-MEDIUM FOR TRACE-METAL STUDIES,” *Journal of Phycology*, vol. 15, no. 2, pp. 135–141, 1979. [Online]. Available: [〈GotoISI〉://A1979HC26300004](#) 9
- [85] U. Schwertmann and R. Cornell, *Iron Oxides in the laboratory: preparation and characterization*, 2nd ed. Germany, New York: Weinheim, Wiley-VCH, 2000. 11, 55
- [86] A. Helmy, E. Ferreiro, and de Bussetti SG, “Surface Area Evaluation of Montmorillonite.” *Journal of colloid and interface science*, vol. 210, no. 1, pp. 167–171, Feb. 1999. [Online]. Available: <http://www.ncbi.nlm.nih.gov/pubmed/9924120> 11, 13
- [87] W.-T. Tsai, C.-W. Lai, and K.-J. Hsien, “Characterization and adsorption properties of diatomaceous earth modified by hydrofluoric acid etching,” *Journal of Colloid and Interface Science*, vol. 297, no. 2, pp. 749–754, 2006. [Online]. Available: <http://www.sciencedirect.com/science/article/pii/S0021979705011148> 11, 13

- [88] T. Hiemstra and W. H. Van Riemsdijk, “A surface structural model for ferrihydrite I: Sites related to primary charge, molar mass, and mass density,” *Geochimica et Cosmochimica Acta*, vol. 73, no. 15, pp. 4423–4436, Aug. 2009. [Online]. Available: <http://linkinghub.elsevier.com/retrieve/pii/S0016703709002944> 11, 53
- [89] A. L. Rose and T. D. Waite, “Kinetics of hydrolysis and precipitation of ferric iron in seawater.” *Environmental science & technology*, vol. 37, no. 17, pp. 3897–903, Sep. 2003. [Online]. Available: <http://www.ncbi.nlm.nih.gov/pubmed/12967111> 11, 38, 54, 57, 58, 59, 70
- [90] S. Cheah, “Steady-state dissolution kinetics of goethite in the presence of desferrioxamine B and oxalate ligands: implications for the microbial acquisition of iron,” *Chemical Geology*, vol. 198, no. 1-2, pp. 63–75, Jul. 2003. [Online]. Available: <http://linkinghub.elsevier.com/retrieve/pii/S0009254102004217> 13
- [91] C. Coccozza, C. C. G. TSAO, S.-F. CHEAH, S. M. KRAEMER, K. N. RAYMOND, T. M. MIANO, and G. SPOSITO, “Temperature dependence of goethite dissolution promoted by trihydroxamate siderophores,” *Geochimica et Cosmochimica Acta*, vol. 66, no. 3, pp. 431–438, Feb. 2002. [Online]. Available: <http://linkinghub.elsevier.com/retrieve/pii/S0016703701007803> 13
- [92] N. Carrasco, R. Kretzschmar, M.-L. Pesch, and S. M. Kraemer, “Low concentrations of surfactants enhance siderophore-promoted dissolution of goethite,” *ENVIRONMENTAL SCIENCE & TECHNOLOGY*, vol. 41, no. 10, pp. 3633–3638, May 2007. 13
- [93] F. Morel and J. G. Hering, *Principles and applications of aquatic chemistry*, ser. Wiley-interscience publication. Wiley, 1993. [Online]. Available: <http://books.google.com/books?id=Rs31PfkeBaIC> 14, 59
- [94] J. Mendez and J. Adkins, “IRON AND MANGANESE IN THE OCEAN: Atmospheric Input by Dust and Coastal Ocean Time Series,” Pasadena, p. 188, 2008. 25
- [95] C. N. Marechal, P. Telouk, and F. Albarede, “Precise analysis of copper and zinc isotopic compositions by plasma-source mass spectrometry.” *Chemical Geology*, vol. 156, pp. 251–273, 1999. 31
- [96] S. G. John and J. F. Adkins, “Analysis of dissolved iron isotopes in seawater,” *Marine Chemistry*, vol. 119, no. 1-4, pp. 65–76, Apr. 2010. [Online]. Available: <http://linkinghub.elsevier.com/retrieve/pii/S0304420310000022> 31, 32, 99
- [97] J. Mendez, C. Guieu, and J. Adkins, “Atmospheric input of manganese and iron to the ocean: Seawater dissolution experiments with Saharan and North American dusts,” *Marine Chemistry*, vol. 120, no. 1-4, pp. 34–43, Jun. 2010. [Online]. Available: <http://linkinghub.elsevier.com/retrieve/pii/S0304420308001448> 38, 57

- [98] J. Davis and J. Leckie, "Surface ionization and complexation at the oxide/water interface II. Surface properties of amorphous iron oxyhydroxide and adsorption of metal ions," *Journal of Colloid and Interface Science*, vol. 67, no. 1, pp. 90–107, Oct. 1978. [Online]. Available: <http://www.sciencedirect.com/science/article/pii/0021979778902175> 54
- [99] D. Girvin, "Neptunium adsorption on synthetic amorphous iron oxyhydroxide," *Journal of Colloid and Interface Science*, vol. 141, no. 1, pp. 67–78, Jan. 1991. [Online]. Available: <http://linkinghub.elsevier.com/retrieve/pii/002197979190303P> 54
- [100] D. Janney, J. Cowley, and P. Buseck, "Transmission electron microscopy of synthetic 2-and 6-line ferrihydrite," *Clays and Clay Minerals*, vol. 48, no. 1, p. 111, 2000. [Online]. Available: <http://www.clays.org/journal/archive/volume48/48-1-111.pdf><http://ccm.geoscienceworld.org/cgi/content/abstract/48/1/111> 55
- [101] T. D. Jickells, Z. S. An, K. K. Andersen, a. R. Baker, G. Bergametti, N. Brooks, J. J. Cao, P. W. Boyd, R. a. Duce, K. a. Hunter, H. Kawahata, N. Kubilay, J. LaRoche, P. S. Liss, N. Mahowald, J. M. Prospero, a. J. Ridgwell, I. Tegen, and R. Torres, "Global iron connections between desert dust, ocean biogeochemistry, and climate." *Science (New York, N.Y.)*, vol. 308, no. 5718, pp. 67–71, Apr. 2005. [Online]. Available: <http://www.ncbi.nlm.nih.gov/pubmed/15802595> 73
- [102] G. Zhuang and R. Duce, "The adsorption of dissolved iron on marine aerosol particles in surface waters of the open ocean," *Deep Sea Research Part I: Oceanographic Research Papers*, vol. 40, no. 7, pp. 1413–1429, 1993. [Online]. Available: <http://linkinghub.elsevier.com/retrieve/pii/096706379390120R> 73, 96, 97
- [103] Z. Shi, M. D. Krom, S. Bonneville, A. R. Baker, C. Bristow, N. Drake, G. Mann, K. Carslaw, J. B. McQuaid, T. Jickells, and L. G. Benning, "Influence of chemical weathering and aging of iron oxides on the potential iron solubility of Saharan dust during simulated atmospheric processing," *Global Biogeochemical Cycles*, vol. 25, no. 2, May 2011. [Online]. Available: <http://www.agu.org/pubs/crossref/2011/2010GB003837.shtml> 73
- [104] G. Benoit and T. Rozan, "The influence of size distribution of the particle concentration effect and trace metal partitioning in rivers," *Geochimica et Cosmochimica Acta*, vol. 63, no. 1, pp. 113–127, 1999. [Online]. Available: <http://www.sciencedirect.com/science/article/pii/S0016703798002762> 94
- [105] M. K. Pham and J.-M. Garnier, "Distribution of Trace Elements Associated with Dissolved Compounds (less than 0.45 μm to 1 nm) in Freshwater Using Coupled (Frontal Cascade) Ultrafiltration and Chromatographic Separations," *Environmental Science & Technology*, vol. 32, no. 4, pp. 440–449, Feb. 1998. [Online]. Available: <http://pubs.acs.org/doi/abs/10.1021/es970183y> 96, 97

- [106] L. García-Rico, L. Tejeda-Valenzuela, M. E. Jara-Marini, and A. Gómez-Álvarez, “Dissolved and particulate metals in water from Sonora Coast: a pristine zone of Gulf of California: metals in water from Sonora Coast.” *Environmental monitoring and assessment*, vol. 176, no. 1-4, pp. 109–23, May 2011. [Online]. Available: <http://www.ncbi.nlm.nih.gov/pubmed/20574698> 96, 97
- [107] G. Benoit, S. Oktay-Marshall, and A. Cantu, “Partitioning of Cu , Pb , Ag , Zn , Fe , Al , and Mn between filter- retained particles, colloids , and solution in six Texas estuaries,” *Marine Chemistry*, vol. 45, pp. 307–336, 1994. [Online]. Available: <http://www.sciencedirect.com/science/article/pii/S0304420394900760> 96, 97
- [108] V. Elrod, W. Berelson, K. Coale, and K. Johnson, “The flux of iron from continental shelf sediments: A missing source for global budgets,” *Geophys. Res. Lett.*, vol. 31, no. 12, p. L12307, 2004. [Online]. Available: <http://www.agu.org/pubs/crossref/2004/2004GL020216.shtml><http://earth.usc.edu/~berelson/papers/elrodgrlFeflux.pdf> 98
- [109] P. J. Lam, J. K. B. Bishop, C. C. Henning, M. a. Marcus, G. a. Waychunas, and I. Y. Fung, “Wintertime phytoplankton bloom in the subarctic Pacific supported by continental margin iron,” *Global Biogeochemical Cycles*, vol. 20, no. 1, pp. 1–12, 2006. [Online]. Available: <http://www.agu.org/pubs/crossref/2006/2005GB002557.shtml> 98
- [110] P. J. Lam and J. K. B. Bishop, “The continental margin is a key source of iron to the HNLC North Pacific Ocean,” *Geophysical Research Letters*, vol. 35, no. 7, pp. 1–5, Apr. 2008. [Online]. Available: <http://www.agu.org/pubs/crossref/2008/2008GL033294.shtml> 98
- [111] B. L. Beard and C. M. Johnson, “High precision iron isotope measurements of terrestrial and lunar materials,” *Geochimica et Cosmochimica Acta*, vol. 63, no. 11-12, pp. 1653–1660, Jun. 1999. [Online]. Available: <http://linkinghub.elsevier.com/retrieve/pii/S0016703799000897> 98
- [112] O. Rouxel, E. Sholkovitz, M. Charette, and K. J. Edwards, “Iron isotope fractionation in subterranean estuaries,” *GEOCHIMICA ET COSMOCHIMICA ACTA*, vol. 72, no. 14, pp. 3413–3430, Jul. 2008. 98
- [113] M. Sharma, M. Polizzotto, and A. D. Anbar, “Iron isotopes in hot springs along the Juan de Fuca Ridge,” *EARTH AND PLANETARY SCIENCE LETTERS*, vol. 194, no. 1-2, pp. 39–51, Dec. 2001. 98
- [114] S. Severmann, C. M. Johnson, B. L. Beard, and J. McManus, “The effect of early diagenesis on the Fe isotope compositions of porewaters and authigenic minerals in continental margin sediments,” *GEOCHIMICA ET COSMOCHIMICA ACTA*, vol. 70, no. 8, pp. 2006–2022, Apr. 2006. 98
- [115] T. D. Bullen, A. F. White, C. W. Childs, D. V. Vivit, and M. S. Schulz, “Demonstration of significant abiotic iron isotope fractionation in nature,” *GEOLOGY*, vol. 29, no. 8, pp. 699–702, Aug. 2001. 98

- [116] S. L. Brantley, L. J. Liermann, R. L. Guynn, A. Anbar, G. A. Icopini, and J. Barling, “Fe isotopic fractionation during mineral dissolution with and without bacteria,” *GEOCHIMICA ET COSMOCHIMICA ACTA*, vol. 68, no. 15, pp. 3189–3204, Aug. 2004. 98
- [117] F. Lacan, a. Radic, C. Jeandel, F. Poitrasson, G. Sarthou, C. Pradoux, and R. Freydier, “Measurement of the isotopic composition of dissolved iron in the open ocean,” *Geophysical Research Letters*, vol. 35, no. 24, pp. 1–5, Dec. 2008. [Online]. Available: <http://www.agu.org/pubs/crossref/2008/2008GL035841.shtml> 99
- [118] A. Radic, F. Lacan, and J. Murray, “Iron isotopes in the seawater of the equatorial Pacific Ocean: New constraints for the oceanic iron cycle,” *Earth and Planetary Science Letters*, vol. 306, no. 1-2, pp. 1–10, 2011. [Online]. Available: <http://www.sciencedirect.com/science/article/pii/S0012821X11001592> 99
- [119] S. John, J. Mendez, J. Moffett, and J. Adkins, “The flux of iron and iron isotopes from San Pedro Basin sediments.” 99
- [120] S. G. John and J. F. Adkins, “Iron isotopes in the North Atlantic: The role of hydrothermal venting and isotopic buffering by particle exchange.” 99